2019

The effects of metallicity and magnetism on the radii of M dwarf stars

BOSTON UNIVERSITY

GRADUATE SCHOOL OF ARTS AND SCIENCES

Dissertation

The Effects of Metallicity and Magnetism on the Radii of M dwarf Stars

by

Aurora Yvonne Kesseli

B.A. Physics, Colby College, Waterville, ME, 2013
M.A., Boston University, Boston, MA, 2016

Submitted in partial fulfillment of the

requirements for the degree of

Doctor of Philosophy

2019

Approved by

First Reader

Philip Muirhead, PhD
Assistant Professor of Astronomy

Second Reader

Tereasa Brainerd, PhD
Associate Professor of Astronomy

Acknowledgments

I would like to thank my soon-to-be husband Andres for always encouraging me to pursue my career dreams even when it meant we would need to spend six months apart. His support is the reason I am finishing the program. I want to thank my family for being the most caring people and inspiring roles models I could ask for. I would also like to thank my community here at Boston University, including my advisor Phil Muirhead and my fellow graduate students, all of whom helped me through the many ups and downs that is graduate school. Finally, I want to thank my thesis committee for their guidance, and especially Davy Kirkpatrick for a wonderful 6 months of working together and mentoring me.

Sections of this dissertation are based upon work supported by the National Science Foundation under grant Nos. 1716260 and 1255568 and by NASA under grant No. 1255568. This work was partially supported by a NASA Keck PI Data Award, administered by the NASA Exoplanet Science Institute. Part of this work was performed while AYK was a Visiting Graduate Student Research Fellow at the Infrared Processing and Analysis Center (IPAC), California Institute of Technology. These results made use of the Lowell Observatory's Discovery Channel Telescope, supported by Discovery Communications, Inc., Boston University, the University of Maryland, the University of Toledo and Northern Arizona University, as well as the Immersion Grating Infrared Spectrograph (IGRINS) that was developed under a collaboration between the University of Texas at Austin and the Korea Astronomy and Space Science Institute (KASI) with the financial support of the US National

Science Foundation under grant AST-1229522, of the University of Texas at Austin, and of the Korean GMT Project of KASI.

THE EFFECTS OF METALLICITY AND MAGNETISM ON THE RADII OF M DWARF STARS

AURORA YVONNE KESSELI

Boston University, Graduate School of Arts and Sciences, 2019

Major Professor: Philip Muirhead, Professor of Astronomy.

ABSTRACT

M dwarfs are ubiquitous in the galaxy, yet their fundamental properties are not precisely known. Radii are particularly difficult to determine because M dwarfs are intrinsically small and faint, leading to only a few radius determinations using either long-baseline optical interferometry or eclipses of binary stars. Observations rarely agree with models, and the scatter in M dwarf radius relations is significantly larger and less understood than it is for higher mass stars. I explored the two main hypotheses evoked to explain discrepancies between model radii and observed radii, namely effects from metallicity and strong magnetic fields. I conducted a spectroscopic survey of M dwarfs with a wide range of metallicities and derived radii using the Stefan-Boltzmann law in order to constrain radius relations for the lowest mass and lowest metallicity stars. I found that solar metallicity stars can be up to five times larger than their low-metallicity counterparts for a given effective temperature, but that metallicity has a relatively small effect on mass- or luminosity-to-radius relations. To test the effect of magnetism on radii, I determined a statistical distribution of radii for magnetically active M dwarfs by combining measured rotational broadening values with literature rotation periods. I found that the magnetically active

stars were on average 10-15% larger than model predictions and that models and observations were most discrepant for the lowest-mass stars. To deduce whether the 10-15% radius discrepancy could be due entirely to the spotted nature of these stars, I determined the spot temperature and spot filling fraction of one of the most magnetically active stars in my sample. I measured a high spot filling fraction, spot temperatures several hundred Kelvin lower than the photosphere temperature, and I also detected evidence of faculae on the stellar surface. I concluded that spots are the primary cause for models overestimating the sizes of low-mass stars, and that stellar-evolution models should consider the effects of spots to more accurately predict the sizes and temperature of all M dwarfs.

Contents

List of Tables

List of Figures

List of Abbreviations

2MASS	Two micron All-Sky Survey
APOGEE	Apache Point Observatory Galactic Evolution Experiment
BOSS	Baryon Oscillation Spectroscopic Survey
BIC	Bayesian Information Criterion
DCT	Discovery Channel Telescope
DBSP	The Palomar Double Spectrograph
FWHM	Full Width at Half Maximum
IGRINS	Immersion Grating Infrared Spectrograph
IRAF	Image Reduction and Analysis Facility
IRSA	NASA/IPAC Infrared Survey Archive
IRTF	Infrared Telescope Facility
LBOI	Long Baseline Optical Interferometry
MCMC	Markov Chain Monte Carlo
MIST	Mesa Isochrones and Stellar Tracks
Pan-STARRS	Panoramic Survey Telescope and Rapid Response System
PDF	Probability Distribution Function
SDSS	Sloan Digital Sky Survey
TESS	Transiting Exoplanet Survey Satellite
WFIRST	Wide-Field Infrared Survey Telescope
WISE	Wide-Field Infrared Survey Explorer

Chapter 1

Introduction

Excerpts from this Chapter are similar to sections published by Kesseli et al. (2017), Kesseli et al. (2018), and Kesseli et al. (2019).

M dwarfs are the most abundant stars in the Galaxy, comprising over 70% of all stars by number and dominating the stellar population of the Milky Way (Bochanski et al. 2010). There is also evidence that M dwarf stars are the dominant components of the stellar populations of other galaxies (e.g., Conroy & van Dokkum 2012), making M dwarf stars the most common type of star in the Universe.

M dwarf stars are dwarf stars that lie on the main sequence in a Hertzsprung-Russell Diagram. Stars that lie on the main sequence are actively fusing hydrogen into helium in their cores and therefore are not still collapsing as pre-main sequence stars nor have they exhausted their core hydrogen supplies as giant stars. M dwarfs were historically categorized by the appearance of molecules in their spectra (Cannon & Pickering 1901) and “M dwarf" referred to the coolest category of dwarf star known at the time. M dwarf stars have masses ranging from 0.08 $M_{\rm Sun}$ to approximately 0.6 $M_{\rm Sun}$. M dwarf stars have correspondingly small radii that typically range from about 0.1 $R_{\rm Sun}$ to 0.6 $R_{\rm Sun}$ and are much dimmer than Sun-like stars, with luminosities ranging from 10^{-3} $L_{\rm Sun}$ to 0.2 $L_{\rm Sun}$. Finally, they have cooler surface temperatures and redder colors than Solar-type stars, with surface temperatures ranging from about 2500 to 4200 Kelvin.

1.1 Motivation

Even with the ubiquity of M dwarf stars, precise determinations of their fundamental parameters are challenging. Radii are particularly difficult to determine because M dwarf stars are intrinsically small and faint, leading to only a few direct radius measurements using long-baseline optical interferometry (< 20, and only three with spectral types later than M3.5; Ségransan et al. 2003; Demory et al. 2009; Boyajian et al. 2012; von Braun et al. 2014; Rabus et al. 2019). Other M dwarf radius measurements come from eclipsing binary stars (EBs). However, many of these systems reveal radii that are as much as $10 - 15\%$ larger than theoretical predictions from stellar evolutionary models, and are on average inflated by $5 - 10\%$ (e.g., Torres & Ribas 2002; Kraus et al. 2011; Han et al. 2017). It does not seem that binarity is responsible for the inflation. Morales et al. (2008) found evidence that single stars were 3% cooler and therefore 5% larger than model predictions by using the Stefan-Boltzmann method to determine radii (see Section 1.4.3), while the limited results from long-baseline optical interferometry also show evidence of the radii being inflated by about 5% compared to models.

Inaccurate stellar radii are a problem for exoplanet characterization because the accuracy and precision of the radius on a transiting exoplanet is limited by the accuracy and precision of the radius on the star. If stellar radii are in error by 15%, a significant fraction of the planets that appear to be rocky super-Earths would be gaseous mini-Neptunes. M dwarf stars appear to host more short-period exoplanets than any other type of star (Dressing & Charbonneau 2015) and are heavily targeted by ongoing planet finding missions such as NASA's Transiting Exoplanet Survey Satellite (*TESS*). With *TESS*'s 27-day baseline for photometric observations, the majority of the discovered exoplanets will be close to their host star. This means that the majority of the habitable zone planets will be around cooler M dwarf stars, since

even close-in planets can have temperate enough climates to support liquid water (Muirhead et al. 2018). By observing and characterizing M dwarf stars, uncertainties in derived exoplanet parameters can be reduced and trends in how stellar properties, such as spectral type and metallicity, correlate with planet occurrence rates can be discovered.

More accurate and precise stellar radius measurements will also improve stellar parameter estimates from upcoming exoplanet microlensing surveys, such as the one to be performed by the Wide Field Infrared Survey Telescope (*WFIRST*). *WFIRST* will monitor Galactic bulge stars and look for brightening indicative of lensing by intervening foreground objects. A planet in orbit around the lensing star can be detected as a secondary perturbation (Gaudi 2012). A large fraction of *WFIRST*'s exoplanet microlensing events will display finite source effects (Zhu et al. 2014), where sharp features of the lens' magnification pattern resolve the finite angular size of the background source star (e.g., Witt & Mao 1994) and allow for measurement of the ratio of the angular source radius to the angular Einstein radius. Knowledge of the angular source radius, for example from the use of color-surface brightness relations (Yoo et al. 2004; Kervella & Fouqué 2008; Boyajian et al. 2012), allows the ratio to be converted into a measurement of the angular Einstein radius and gives a constraint on the mass of the lens (Gould 1994; Nemiroff & Wickramasinghe 1994). However, to do this the sizes of the background bulge source stars need to be known, of which the vast majority will be M dwarfs.

In addition to being important for exoplanet characterization, accurate radii provide an observable to test the accuracy of stellar structure and stellar evolutionary models. M dwarf stars represent an especially interesting part of parameter space for model testing because the transition from partially convective to fully convective energy transport takes place in the middle of their spectral sequence (Reid et al.

1995; Chabrier & Baraffe 1997). Higher mass M dwarf stars have a radiative core and a convective exterior like the Sun, while in lower mass M dwarf stars convection is the dominant form of energy transport throughout the star. Along with testing how well models can capture the fully-convective boundary, the lowest mass M dwarfs also allow theoretical tests of the effects of core electron degeneracy pressure on the radii (Cassisi & Salaris 2019). If models and observations do not agree, there is potentially some piece of physics within these stars which is not accurately captured in the modeling process.

1.2 M dwarf Parameters

Before discussing M dwarf radii in detail, I will review other M dwarf fundamental parameters that will be important throughout this dissertation.

1.2.1 Spectral Types

Historically, a star's spectral type was used to estimate a star's fundamental parameters. The M spectral sequence is characterized by the appearance of large molecular features, especially titanium oxide (TiO) in optical spectra (Cannon & Pickering 1901; Kirkpatrick et al. 1991). Spectral types of low-mass stars are usually determined by comparing mid-resolution optical or IR spectra to template spectra of known spectral types. Once a spectral type is determined, many relations exist for converting the spectral type to a rough estimate of the star's fundamental parameters, such as mass, temperature and radius (Cox 2000).

Although spectral types are useful, and in many instances are the only available way to estimate a star's fundamental parameters, spectral types only correspond directly to temperature, and even the derived temperature can be misleading because of the possibility of spots being present on the stellar surface (see Chapter 5). A

relatively wide range of metallicities, masses, and radii can correspond to a single spectral type. For example, I found that a low-metallicity and a high-metallicity star of the same spectral type (both M3 dwarfs) can range in radius estimates by up to a factor of five (see Section 3.6 and Kesseli et al. 2019). Therefore, using a spectral type to determine any physical parameter should be used as an initial estimate.

1.2.2 Metallicity

The metallicity of a star is a measurement of the bulk chemical composition of all elements heavier than hydrogen and helium. By convention, astronomers refer to these heavier elements as "metals" ([m/H]). An [m/H] of +0.5 dex means that a star has $10^{0.5}$ times each element's solar abundance. Often [m/H] is estimated by deriving the iron-to-hydrogen fraction, [Fe/H]. While it may seem inaccurate to assign abundances of all metals based solely on the abundance of iron, this is actually relatively accurate due to the metallicity enrichment history of the Galaxy. After the Big Bang, the early Universe was composed nearly entirely of hydrogen and helium. As the Universe aged, massive stars created mainly alpha-process elements (or simply alpha elements; e.g., C, O, Ne, Mg, Si, etc.) during fusion. The short lifetimes and explosive deaths of these massive stars rapidly distributed these elements throughout the first galaxies (e.g., Woosley & Weaver 1995). As time passed and lower mass stars began to migrate off the main sequence, and Type Ia supernovae, which involve an exploding white dwarf, became the dominant form of elemental enrichment in the Galaxy. Type Ia supernovae created a different ratio of elements and increased the ratio of Fe to alpha elements (Johnson 2019). The consequence of this enrichment process is a correlation between different elemental abundances in the Galaxy (Spite et al. 2005). This means that metallicity is also related to age, since older stars formed when the Galaxy had yet to be enriched by heavier elements, and ages can

be estimated by taking into account both the bulk metallicity as well as the alpha to Fe ratio (Veyette & Muirhead 2018).

Precise metallicities of M dwarfs are notoriously difficult to determine because much of their spectra are dominated by deep molecular features due to their low surface temperatures. This results in a lack of a true continuum and few unblended atomic iron lines, which are used to measure metallicities in solar-type stars. Unlike in higher mass stars, metallicities cannot be determined by comparisons to models because of incomplete lists of line opacities. In addition, a lack of knowledge of input parameters for pressure broadening becomes problematic for the complex, molecular-rich atmospheres of low-mass stars (Allard et al. 2012; Husser et al. 2013).

Recently, however, many groups have successfully used widely separated binaries or common proper motion stars that contain an F, G, or K star and an M dwarf companion to empirically calibrate M dwarf metallicities (e.g., Rojas-Ayala et al. 2010, 2012; Terrien et al. 2012; Mann et al. 2013a; Newton et al. 2014). These studies created relations that convert equivalent width or spectral indices of spectral features that are measurable in M dwarf stars (such as Na, Ca, and K) to bulk metallicity estimates. These techniques can precisely determine M dwarf metallicities for the first time and usually have uncertainties ranging from about 0.08 to 0.15 dex.

Even with all these advances there are still areas for improvement in M dwarf metallicity studies. While bulk metallicities are now possible, individual elemental abundances, which are common in solar-type stars, are still under development. Veyette et al. (2017) recently published a method to determine Ti and Fe abundances using high resolution Y-band spectra, but this method is only valid for a small range of temperatures and for only two elements. These techniques are also limited to near solar-metallicity stars and almost no work has been done to calibrate metallicity relations for abundances less than -0.5 dex.

1.3 Interior Structure and Magnetic Field Generation in M dwarfs

The interior structure of M dwarf stars differs from Sun-like stars due to a transition from a combination of convective and radiative energy transport in Sun-like stars to transport completely dominated by convection in lower-mass M dwarfs. This interior structure change is important to discuss here because it affects how the magnetic fields are generated within the star and therefore on the magnetic field strengths of M dwarf stars.

1.3.1 M dwarf Structure

In Sun-like stars and higher mass M dwarf stars, energy in the core is transported primarily by radiation, and energy in the exterior of the star is transported primarily by convection. For convection to occur, the Schwarzschild criterion states that

$$\left|\frac{dT}{dr}\right|_{act} > \left|\frac{dT}{dr}\right|_{ad} \tag{1.1}$$

meaning that the actual temperature gradient has to be larger than the adiabatic temperature gradient. In the outer layers of Sun-like stars the temperature is cool enough that the opacity increases due to partial ionization, causing a steep temperature gradient and creating a convective outer envelope. However, in the interior of the star radiation is transporting the bulk of the energy. The boundary between the radiative layer and the convective layer is called the tachocline. For stars of lower mass, the tachocline is deeper into the star as the convective conditions are met closer to the center of the star because of increasing opacities and lower temperatures. Finally, for the lowest mass stars, the tachocline disappears and convection is the dominant form of energy transport throughout the star (Chabrier & Baraffe 1997). The exact mass at which the tachocline disappears is still not exactly known

and different estimates place the transition at masses between $0.23 - 0.4 M_{Sun}$ (e.g., Chabrier & Baraffe 1997; Baraffe & Chabrier 2018; MacDonald & Gizis 2018; Rabus et al. 2019).

1.3.2 Magnetic Field Generation

Large scale magnetic fields in stars are generated through a dynamo process in which electrically conducting fluids generate and maintain a magnetic field (Parker 1975). In Sun-like stars the tachocline is thought to be essential to generate the large-scale magnetic field though the $\alpha\Omega$ dynamo process (Ossendrijver 2003). The α effect arises from the stretching and strengthening of magnetic fields during the interaction of convection and rotation, and generates a poloidal magnetic field from a toroidal magnetic field. The Ω effect again arises from the stretching and strengthening of magnetic fields, but this time due to differential rotation shears at the tachocline, and a toroidal field is generated from a poloidal field. Both of these effects rely on the rotation of the star to generate the necessary shearing and stretching of the fields, and together these effects work to amplify and sustain large scale magnetic fields.

Global magnetic field generation on fully convective M dwarfs is still not fully understood due to the fact that fully convective M dwarfs do not have a tachocline and cannot therefore support the Ω process. One might then expect that fully convective M dwarf stars cannot generate strong global magnetic fields; however, observations of magnetic fields on fully convective M dwarf stars show clear evidence of magnetism (see Section 1.3.3). Recent modeling results from Browning (2008) can now produce large scale magnetic fields through the α effect alone (α^2), but more work is required to confirm these findings.

1.3.3 Observations of Magnetic Field Strengths

It has long been inferred that M dwarf stars have strong magnetic fields due to observations of frequent flares and signatures of magnetic activity. The strong magnetic fields cause flares when magnetic fields reconnect and release large amounts of stored magnetic energy. M dwarf flares are observed to be 100 to 1000 times more energetic than the largest solar flares, and they produce large amounts of X-ray and UV flux (Youngblood et al. 2017). Magnetic activity signatures refer to emission from Hα or Ca H and K lines, and a magnetically active M dwarf is one that shows Hα in emission while an inactive M dwarf shows Hα in absorption or not at all. On the Sun, the intensity of Hα or Ca H and K emission is directly correlated to magnetic field strength (Leighton 1959; Skumanich et al. 1975), and so emission from these lines in spectra of other stars has long been used as an indirect determination of magnetic field strength (Wilson 1968). Both early-type (partially convective) and late-type (fully convective) M dwarf stars are observed to be magnetically active. In a survey of over 50,000 M dwarf stars from the Sloan Digital Sky Survey, West et al. (2011) found that about $10-15\%$ of early-type M dwarfs (spectral types M0 to M4) were magnetically active, while over 50% of late-type M dwarfs (spectral types $>$ M5) were magnetically active.

Direct detections of magnetic fields on M dwarf stars using the Zeeman effect have revealed kiloGauss scale surface magnetic fields that are often more than one thousand times stronger than those present on the Sun (e.g., Saar & Linsky 1985). The Zeeman effect causes a splitting of degenerate atomic levels due to the interaction of the electron's orbital magnetic moment with an external magnetic field. The separation in wavelength of the split line is directly proportional to the magnetic field strength. Recently, the Zeeman effect has been utilized to not only measure the average surface magnetic field, but also to resolve magnetic structure on stellar

surfaces through Zeeman Doppler imaging (ZDI). ZDI measures periodic modulations of Zeeman signatures such as polarized light to resolve the topological magnetic field structure (Donati et al. 2006; Morin et al. 2010). Again, this technique showed that both early-type and late-type M dwarfs seem to host strong magnetic fields. Unfortunately, ZDI cannot be used to determine magnetic field structure on many stars as it is observationally expensive and can only be done on the brightest nearby stars.

Lastly, it is pertinent to make the connection between magnetic field strength, stellar rotation, and age. In Sun-like stars a simple relation between rotation period and magnetic field strength exists (Skumanich 1972), where more rapidly rotating stars have stronger magnetic fields due to the dynamo generation process as discussed in Section 1.3.2. Rapidly rotating stars are also younger than slowly rotating stars since as stars age they shed angular momentum, and so in Sun-like stars an age can be estimated simply with a rotation period or magnetic field strength (Barnes 2003). West et al. (2015) found that M dwarfs with rotation periods less than 5 days were all magnetically active, providing evidence that rotation and magnetism are correlated in M dwarfs. However, Newton et al. (2016) showed that a one-to-one relation between rotation and magnetic activity does not exist for late-type M dwarfs and instead a period dichotomy is present. Newton et al. (2016) interpreted the dichotomy as evidence that late-type M dwarfs continue to rotate rapidly and have strong magnetic fields for up to 5 Gyr and then quickly lose angular momentum and rotate with periods greater than about 40 days. This further suggests that magnetic field generation in late-type M dwarf stars is not produced by the same mechanism as in Sun-like stars.

1.4 Observations of M dwarf Radii

In the following sections I will detail the most common ways that radii of M dwarf stars are observationally determined. As previously mentioned, precise and accurate radii of M dwarf stars are difficult to determine, and so I will also discuss the limitations of each method.

1.4.1 Eclipsing Binaries

Most measurements of M dwarf radii are from eclipsing binaries– binary stars that happen to be oriented in a configuration such that the stars pass in front of and behind each other during their orbit as viewed from our perspective. This chance configuration allows for precise, model-independent measurements of masses and radii by combining photometric time-series data with radial velocities derived from spectra.

Radial velocities are determined by observing periodic Doppler shifts in the spectrum throughout the orbit of the binary system. If the stars are comparable in brightness and it is possible to distinguish both pairs of spectral lines, then both radial velocity shifts can be measured and the system is called an SB2. The two radial velocities can be used to derive information on the masses and the semimajor axes of the orbits. With radial velocity measurements throughout the orbit, the ellipticity of the orbit can also be determined by modeling the shape of the radial velocity curve.

Photometric time-series data, or light curves, show periodic dips in brightness as the stars are eclipsed by each other. The period of the orbit can easily be measured from the time between mid-eclipses. The ratio of the eclipse depths and the time between the start of a transit and full depth of a transit gives information on the stellar radii. The inclination of the system can be determined by modeling the eclipse shape to see if the stars are in a grazing orbit or a near-perfect, edge-on orbit.

By combining all of the information from the radial velocity measurements and the light curves, the masses, radii, eccentricity, semimajor axes, and period of the system can be measured to a precision better than 5% (e.g., Torres et al. 2010; López-Morales 2007). While I have simplified the explanations of how the parameters are determined, in reality there are degeneracies between many of these parameters and a careful reduction process is required to achieve the above quoted 5% uncertainty.

While EBs can give precise, model-independent parameters, the measurements are observationally expensive. Eclipsing binaries require a chance orientation and so to find them a large number of targets need to be photometrically monitored at a high cadence. Before the late 2000s only 3 SB2 systems containing an M dwarf star were known, but with recent surveys such as *TESS* and *Kepler* this number has significantly increased. Additionally, to determine the radial velocities to a high precision, high-resolution spectral observations are needed at multiple times throughout the orbit of the binary system. Since M dwarf stars are dim, long exposure times are required to build up enough signal to accurately measure radial velocities.

Even with good data there are still significant sources of astrophysical noise that complicate the process of deriving masses and radii. The surfaces of M dwarf stars are heavily spotted, which introduces photometric variability into the light curves, making it difficult to precisely model the eclipses (Torres & Ribas 2002). M dwarf stars also flare frequently (Hilton et al. 2010; Davenport et al. 2019), and while removing flares from the light curves is possible it can add noise to the photometric data points.

Furthermore, the way in which the stellar parameters are extracted from the light curves is also subject to sources of uncertainty. Morales et al. (2010) showed that if magnetic cool spots on active M dwarf stars are preferentially distributed near the poles (as seen by Granzer et al. 2000; Jeffers et al. 2007; Strassmeier 2009), the

radii could be overestimated by up to 6% by parameter extraction codes that assume circular stellar disks when modeling EB light curves. In addition, reanalysis of EB data from multiple groups has oftentimes lead to vastly different stellar parameters, calling into question the accuracy of parameters extracted from all EBs (e.g., Han et al. 2017).

Finally, these stars are all binaries and may not have properties that are representative of single star. Disk disruption and/or tidal effects from close binaries could alter the evolutionary history of EBs (Meibom et al. 2006; Morgan et al. 2012).

1.4.2 Long Baseline Optical Interferometry

Long baseline optical interferometry (LBOI) is another common method for obtaining precise measurements of M dwarf radii. LBOI measurements directly resolve the disk of the target to determine a radius. To gain the angular resolution required to resolve a stellar disk, multiple telescopes are spread out across a wide area, effectively increasing the diameter of the telescope dish. The light from the many telescopes is passed through vacuum tubes and combined coherently so the wavelengths are matched to an accuracy of less than one micron (Monnier 2003). An interferometer records the interference fringes created by combining the light. To determine the angular diameter of a star the fringe contrast or “visibility" is measured. The visibility is the fringe amplitude divided by the average intensity, and the shape of the visibility curve is directly related to the size of the star; a larger stellar angular diameter corresponds to a smaller visibility for a set baseline.

LBOI requires extremely stable conditions, both at the telescope and in the atmosphere. Small distortions or alterations to the mirror angles can lead to changes in the fringing patterns. Atmospheric turbulence can cause wavefront distortions and can lead to the telescope no longer being diffraction limited and potentially faulty measurements. To avoid this problem, the telescopes often take short exposures and

quickly move between observations of a target star and observations of a calibrator star located nearby so that the turbulence in the targeted area of the sky can be characterized (Boyajian et al. 2012). Due to these short exposures the target star has to be exceptionally bright.

A few facilities are capable of performing long baseline optical inteferometry, including the Center for High Angular Resolution Astronomy (CHARA) array, the Palomar Testbed Interferometer (PTI), the Naval Precision Optical Interferometer (NPOI), and the Very Large Telescope Interferometer (VLTI). CHARA is currently the most powerful optical interferometer in the world and using a 331 m baseline, it can resolve angular diameters as small as 0.4 mas in the V band (ten Brummelaar et al. 2005). In order to successfully determine angular diameters, CHARA has a limiting magnitude of 7 in the H or K band. This leaves only the closest 5 or so late-type M dwarfs for which this method is possible, which does not allow for much exploration of interesting areas of parameter space.

1.4.3 Stefan-Boltzmann Law

The radii of stars can be determined by combining effective temperatures and bolometric luminosities via the Stefan-Boltzmann law

$$R = \sqrt{L_{\rm bol}/4\pi\sigma T_{\rm eff}^4} \tag{1.2}$$

where R is the radius, $L_{\rm bol}$ is the luminosity, and $T_{\rm eff}$ is the effective temperature. This method can be used to determine radii for a large number of stars as it is not observationally expensive (like EBs) and does not require particularly bright sources (like LBOI).

To determine $L_{\rm bol}$, the bolometric flux and the parallax are combined in the following equation

$$L_{\rm bol} = 4\pi D^2 F_{\rm bol} \tag{1.3}$$

where D is the distance and is simply the inverted parallax. Prior to Gaia, parallaxes for a large number of M dwarfs were not available, but now upwards of a million M dwarfs have precise parallax measurements (Gaia Collaboration et al. 2018). The bolometric flux is the flux in all wavelengths emitted by the star. To determine bolometric fluxes, bolometric corrections have been historically used to convert a flux in a single band to the bolometric flux (e.g., Bessell & Brett 1988). This method is prone to large uncertainties, as stars with the same flux in one band can have vastly different bolometric fluxes due to changes in parameters such as metallicity, surface gravity, etc. With the wealth of data from all-sky surveys, it is now possible to obtain photometry spanning the UV (*GALEX*), to the optical (Gaia, SDSS, and pan-STARRS), to the near- and mid-IR (2MASS and *WISE*, respectively) for many sources. With photometry covering a large wavelength region, the bolometric flux can be obtained simply by integrating under a curve connecting the photometry point.

Effective temperatures are often estimated by comparing spectra to models or by using relationships between photometric color and effective temperature. As mentioned in Section 1.2, model spectra of M dwarf stars still cannot correctly match every spectral feature, but they can capture the overall behavior and can fit the majority of the dominant spectral features. Because of this, moderate-resolution spectra with wide wavelength coverage, not single spectral features, are often used for the model fits. By using an entire spectrum to calculate a temperature, effects from spurious model features or changes in line depths due to differences in elemental abundance, bulk metallicity, or magnetism (Zeeman broadening) are mitigated.

Even by using large parts of the spectrum, model fits still have uncertainties of at least 60 K and often up to 150 K (Mann et al. 2013c; Rajpurohit et al. 2016, e.g.,).

While color-to-$T_{\rm eff}$ relations do not rely on models, there are many other sources of uncertainty that are associated with them. Recent studies have used a sample of calibrator stars with effective temperatures known to a high precision and fit color relations to these stars (e.g., Mann et al. 2015). The precise effective temperatures were determined by combining LBOI radii with bolometric luminosities (determined with broadband photometry as mentioned above) to estimate the effective temperature using Equation 1.2. Unfortunately, color is susceptible to changes in metallicity and, so, all of these relations are metallicity dependent. In addition, they have not been calibrated to the lowest mass stars. If targets are confined to a spectral type of $\sim$M0$-$M5 and a metallicity within $\sim$0.5 dex of solar metallicity, uncertainties are as low as 47 K, but outside of this limited parameter space uncertainties can be much higher.

By taking into account the uncertainties from the measurement of the bolometric luminosity and effective temperature, I found that radii cannot be estimated to a $\sim$10% precision using this method (Kesseli et al. 2019). Therefore, this method can be useful when estimating radii for a large sample of stars and looking for general trends present in the data, but is less useful for getting an accurate and precise measurement of a single star, or detecting changes in radii less than $\sim$ 10%.

1.5 Radii from Stellar Evolutionary Models

Stellar evolution codes in their most basic form solve the equations of stellar structure and and energy transport. Stellar evolution models of low-mass stars have historically been challenging and often did not agree with data. In the past, gray atmospheres were used as an approximation for the surface boundary conditions, but

this approximation was shown to not be valid for low-mass stars (Allard & Hauschildt 1995; Chabrier & Baraffe 2000; Feiden & Chaboyer 2012). Modern codes solve for the interior structure and then use state-of-the-art stellar atmosphere models as the surface boundary conditions, which has yielded much better results for K- and M-type stars (e.g., Feiden & Chaboyer 2012; Chen et al. 2014). Models of low-mass stars have also been complicated by the fact that many opacity lists do not extend to low enough temperatures (e.g., Iglesias & Rogers 1996), and unlike solar-mass stars, are unable to use an analytic equation of state due to non-ideal contributions at the high plasma densities present in their interiors (Dotter et al. 2007).

Stellar isochrones are the usable output of a stellar evolution model. They relate intrinsic properties such as the mass, radius, and effective temperature at a single age to observables such as magnitudes. Currently many groups are developing stellar isochrones, some of the prominent ones being BHAC (Baraffe et al. 1997, 2015), Yonsei-Yale (Demarque et al. 2004), Padova (Bressan et al. 2012; Chen et al. 2014), Dartmouth (Dotter et al. 2008; Feiden & Chaboyer 2014), MIST (Choi et al. 2016), and Victoria-Regina (VandenBerg et al. 2006). Isochrones from each of these groups are all computed in generally the same way, but small differences such as which atmosphere models are used for the boundary conditions, which code is used to calculate equations of state, or what mixing length value is used can differ between them. All of these models show general agreement to within $5-10\%$ for most of the parameters computed for the isochrones; however, different groups have specialized in different parts of parameter space. For example, the BHAC and MIST groups have computed pre-main sequence isochrones for low-mass stars (Baraffe et al. 2015; Choi et al. 2016), while most of the other groups only have isochrones starting at 1 Gyr for low-mass stars. Recently, significant work has been done with the Dartmouth models to include effects from strong magnetic fields (Feiden & Chaboyer 2012, 2014). The

Dartmouth models are also the only ones to contain abundance variations beyond a simple bulk metallicity change (small α element variations are available in Dotter et al. 2008), although the MIST models are in the process of incorporating even more abundance variations such as carbon enhancement.

1.5.1 Comparisons between model radii and observed radii

Radii of stars determined using EBs are often $10-15\%$ larger than theoretical predictions from stellar evolutionary models, and are on average inflated by $\sim 6\%$ (e.g., Torres & Ribas 2002; Kraus et al. 2011; Han et al. 2017; Parsons et al. 2018). A few examples of stars with radii inflated by up to 3 times the predicted radius are present in the literature (e.g., Çakırlı et al. 2013). However, Han et al. (2017) have since shown that examples such as these all seem to be a problem with the parameter extraction and the radii of these stars are actually consistent with the rest of the EBs (see Figure 1.1).

It does not seem to be only binary stars that are larger than model predictions, and there is evidence that single stars also show radius inflation. Boyajian et al. (2012) combined all of the K and M dwarfs with radii from LBOI into one sample and determined that these stars are larger than models by an average of 5%. Morales et al. (2008) determined radii using the Stefan-Boltzmann method for about 700 single star and found that K and M dwarfs were on average 3% cooler than models predicted, and in turn about 6% larger than models predicted.

1.6 Hypotheses for M dwarf Radius Discrepancies

Several theories have been suggested to explain these discrepancies between models and observations. The two most prominent theories involve inaccurate metallicities or enhanced magnetic fields.

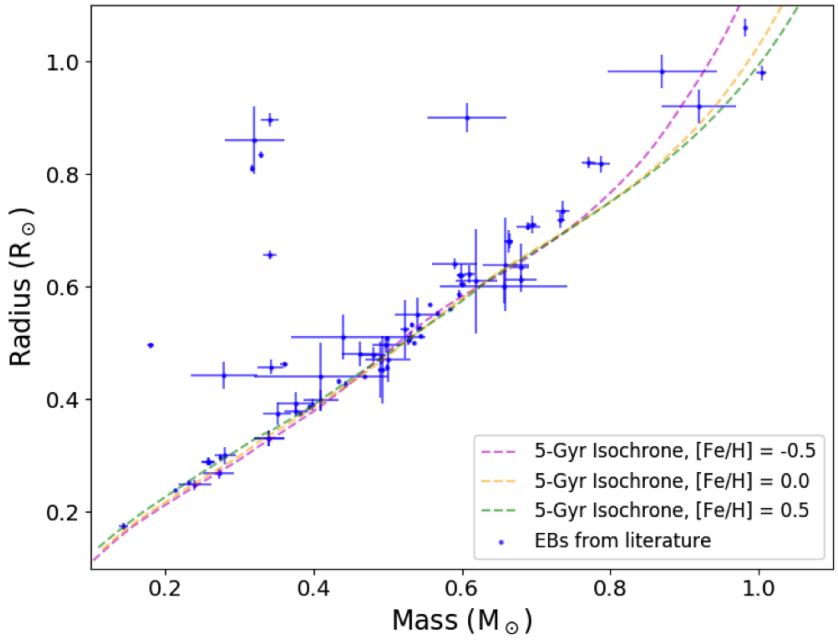

Fig. 1.1: Results of EB masses and radii from the literature (compiled by Han et al. 2017; blue points) and Dartmouth stellar evolutionary models (colored lines). Han et al. (2017) found that the radii of the EBs with the largest radius inflation were incorrect, drawing into question all of the hyper-inflated radius results. This however does not change the fact that many of the EBs show radii that are larger than the models predict, with models predicting values that are on average 6% smaller than EB measurements.

1.6.1 Metallicity

The metallicity of stars is theorized to alter their radii since metallicity controls the opacity of the atmosphere, which modifies the equilibrium configuration for a given luminosity (Burrows et al. 1993). Additionally, in metal-poor stars the photosphere is expected to lie deeper in the star where the gas temperature is higher, leading to smaller radii for a given effective temperature ($T_{\rm eff}$). Since metallicity estimates for M dwarf stars are still relatively new and have relatively high uncertainties, if the EBs in Figure 1.1 are all slightly more metal-rich than their derived metallicities show, then the 5−10% discrepancy could potentially be explained.

The effect of metallicity on radii has been predicted theoretically, and models from every group mentioned in Section 1.5 show that lower metallicity M dwarf stars have smaller radii for a given luminosity and temperature. Even with clear theoretical predictions, the metallicity−radius effect has proven difficult to confirm observationally. Berger et al. (2006) found that the deviations between model radii (with an assumed fixed mass) and radii of six low-mass stars determined using LBOI correlated with metallicity. However, López-Morales (2007) found no metallicity correlation for radius discrepancies between models and observations of six low-mass eclipsing binaries. Boyajian et al. (2012) published a compiled sample of all the low-mass radii from LBOI and saw no trend in radius with metallicity for a given mass, luminosity, or temperature. Finally, using the largest data set of M dwarf radii to date, Mann et al. (2015) saw clear evidence of a metallicity trend in a temperature versus radius plot (Figure 1.2), and slight evidence for a metallicity trend in an absolute K_s-band versus radius plot. It is important to note that all of these studies used near-solar metallicity stars that only ranged from -0.5 to $+0.3$ dex in metallicity, which undoubtedly played a role in the difficulty to observationally confirm the role of metallicity on radii.

1.6.2 Magnetism

There are two main mechanisms proposed to explain how ignoring magnetic fields in the models leads to underestimated radii. Chabrier et al. (2007) used stellar models to demonstrate that rotation-induced surface magnetic fields can lead to larger radii of low-mass stars by two scenarios: (1) strong magnetic fields inhibit convective flows, and (2) magnetic cool spots decrease the overall effective temperature of the star, and thus increase the radius as the luminosity is unchanged.

Mixing length theory is used to model energy transport by convection in stellar interiors by approximating the energy flux carried by a convective bubble. The

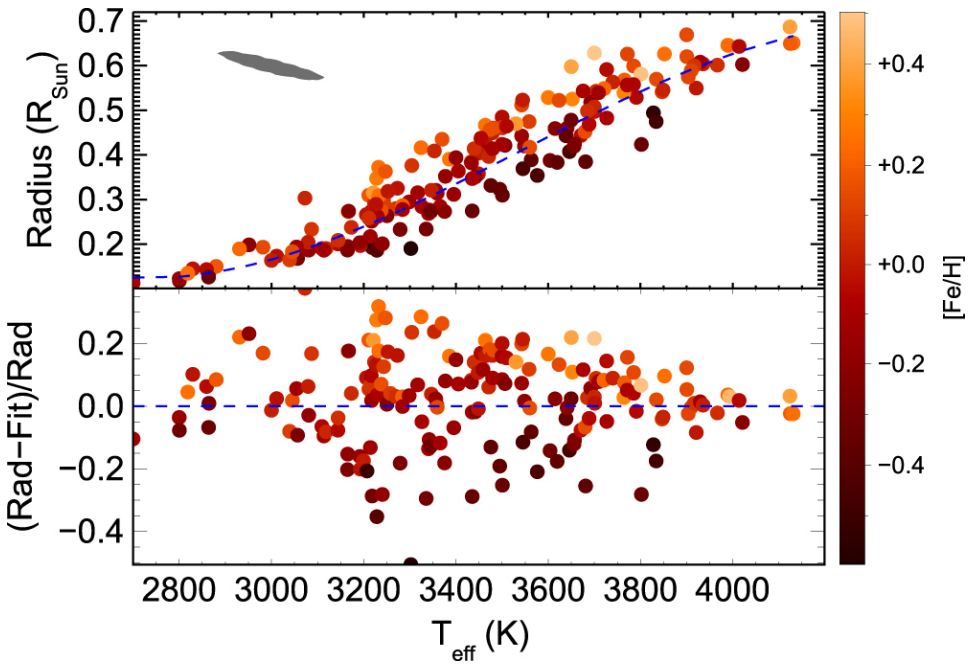

Fig. 1.2: $T_{\rm eff}$ versus radius relation from Mann et al. (2015). Clear evidence of a trend with metallicity is seen in the residual plot, where the higher metallicity stars all sit above the dotted blue metallicity-independent empirical relation and the metal-poor stars sit below the dotted blue line. This was the first clear confirmation that radii are metallicity dependant for a fixed effective temperature. Reprinted with permission from Mann et al. (2015).

mixing length parameter, α, is the ratio between average distance a convective bubble moves before it is dissipated and the pressure scale height. To model the effects of scenario (1), Chabrier et al. (2007) decreased α. In regions where convection is nearly adiabatic, changing the mixing length has little effect on heat transport and therefore little effect on the radius of the star. However, in regions where convection is superadiabatic, decreasing alpha leads to a higher fraction of heat being transported by radiation, steeper temperature gradients, and in turn cooler effective temperatures and larger radii. Superadiabaticity is inversely proportional to density squared and less dense regions (like the outer convective zones in Sun-like stars and early-M dwarfs) are superadiabatic, while the exteriors of the lowest mass M dwarfs are still too dense to become superadiabatic. For this reason, Chabrier et al. (2007) predicted

that lower the mass of the star, the less it would be affected by scenario (1) and that in fully convective M dwarfs inflation would be primarily due to spots (see Figure 1.3).

To estimate how much scenario (2) would affect the radii of M dwarfs, Chabrier et al. (2007) assumed that some fraction of the surface of the star is covered in cool spots. The flux emerging from the star is a combination of a flux from the spot or spots and a flux from the quiescent photosphere

$$F_{\rm tot} = F_{\rm phot}(1-\beta) + F_{\rm spot}\beta = \sigma T_{\rm phot}^4(1-\beta) + \sigma T_{\rm spot}^4\beta \tag{1.4}$$

where β is the spot covering fraction and is defined as the area of the spots over the area of the quiescent photosphere, or $\beta = S_{\rm spot}/S_{\rm phot}$, F is the flux, and $T_{\rm phot}$ and $T_{\rm spot}$ are the effective temperatures of the photosphere and spot, respectively. Next, Chabrier et al. (2007) assumed that a spotted star and an unspotted star of the same mass would have the same luminosity, and therefore derived how much larger the radius would need to be to offset the lower flux emitted from the spotted star.

$$\frac{R_{\rm unspotted}^2}{R_{\rm spotted}^2} = 1 - \beta + \beta\frac{T_{\rm spot}^4}{T_{\rm phot}^4} \tag{1.5}$$

Chabrier et al. (2007) found that scenario (2) alone could inflate the radii of M dwarf stars seen in EBs, but only with a large spot covering fraction of 30-50% of the stellar surface (see Figure 1.3). This estimate was a simple test since Chabrier et al. (2007) did not know spot temperatures or have any realistic estimates of spot covering fractions.

The work of Chabrier et al. (2007) has been updated and tested more thoroughly since its publication. Feiden & Chaboyer (2014) used the Dartmouth Magnetic Stellar Evolution Tracks and Relations (DMSETR; Feiden & Chaboyer 2012) to explore both of these scenarios in greater detail. Instead of modeling scenario (1) using

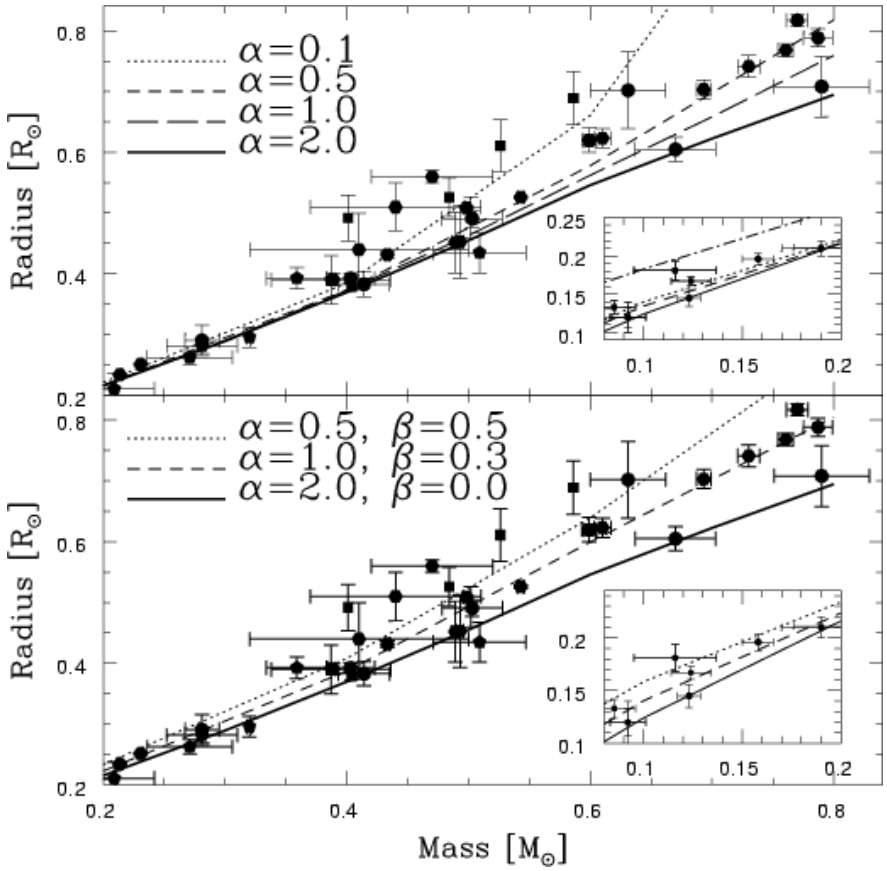

Fig. 1.3: Figure from Chabrier et al. (2007) showing the effect of decreasing the mixing length (α) and increasing fraction of the surface covered in cool spots (β) on the radii of M dwarf stars. The effect of decreasing the mixing length parameter greatly increases the radii for a given mass of partially convective stars ($M > 0.35 M_{Sun}$) but does not increase the radii of fully convective stars ($M < 0.35 M_{Sun}$) at all. The points on the plot are measured radii of EBs from the literature. Reprinted with permission from Chabrier et al. (2007).

a decreased mixing length parameter, they modeled how the magnetic field could stabilize convection and found that it could inflate the radii of fully convective stars by 5-6% if extremely strong interior magnetic fields were invoked (40 MG). However, theoretical predictions of interior field strengths concluded that the above-quoted field strengths were unreasonably large (Browning et al. 2016). On the other hand, MacDonald & Mullan (2017) used a similar approach to that of Feiden & Chaboyer

(2014), but found interior magnetic fields strengths on the order of 10 kG could inflate the radii of fully convective stars to a similar degree as seen in EBs.

Observational evidence for strong magnetic fields causing larger than expected radii can be seen in studies of EBs. EBs with measured radii tend to have short orbital periods, because of observational biases, and are synchronously rotating. Stars that are rotating more rapidly have stronger magnetic fields due to the dynamo process, and so EBs are preferentially selected to have strong magnetic fields. It follows that if the magnetic inflation scenario is correct, EBs would be on average slightly more inflated than radii of single stars observed through LBOI, which is exactly what is seen. Furthermore, in a survey of six EBs, Kraus et al. (2011) found some evidence that the radii of the stars in shorter period binary systems were slightly more inflated than the radii of the stars in longer period EBs. Both of these pieces of evidence are highly disputed and neither offer any evidence as to the mechanism (i.e., whether the above scenario (1) or (2) is responsible for the radius inflation) behind the mismatch between the models and observations.

To disentangle the roles of the two scenarios proposed to inflate the radii and to determine whether the inflation seen in EBs is real, and not some product of the difficulty in extracting accurate parameters (see Section 1.4.1), a large sample of single stars with accurate radii is required. If partially convective and fully convective stars are inflated to the same degree, then it follows that scenario (2) is most likely responsible for the majority of the radius inflation. With a sample that spans many different rotation periods, a potentially new and more accurate radius relation which includes a rotation parameter can also be developed. Deducing the role of magnetism on radii will help provide constraints for future modeling and provide insights into the physics present on these small stars.

1.7 Concluding Remarks

For the bulk of my dissertation I explored the role of different fundamental parameters on the radii of M dwarf stars. However to start, I examined how to determine these fundamental parameters and developed tools to estimate metallicity, spectral type and surface gravity of low-mass stars (Chapter 2). In Chapter 3 I quantified the effects of metallicity on M dwarf radii to determine if metallicity variation could be causing the discrepancies between models and observations. I found that while stars with different metallicities and the same $T_{\rm eff}$ can have vastly different radii, the discrepancies in the mass – radius relation are not likely to be due to metallicity. Next, I explored how strong magnetic fields and rapid rotation can alter the radii of M dwarf stars (Chapter 4). I calculated that rapidly rotating stars are on average 10-16% larger than models predict. I then explored the mechanism causing the radius discrepancy observed in the rapidly rotating stars and determined if magnetic starspots could completely account for these stars being larger than model predictions (Chapter 5). I found that spots alone could sufficiently suppress $T_{\rm eff}$ and inflate the radii compared to what models predicted. Finally, I summarized the results in Chapter 6 and discussed the degree to which metallicity and magnetism were responsible for the radius discrepancies and scatter in the mass – radius diagram of M dwarf stars.

Chapter 2

Spectral Templates and a Method for Estimating Metallicities

A similar version of this Chapter was published in the Astrophysical Journal Supplements by Kesseli et al. (2017).

2.1 Introduction

Empirical stellar spectral libraries are crucial for many areas of astronomical research. These include, but are not limited to, simple assignment of stellar spectral types by-eye, more complicated machine learning spectral typing, and modeling the spectral energy distributions and stellar populations of galaxies. The determination of stellar properties such as surface gravity, metallicity and effective temperature is often completed by comparisons to empirical templates with known parameters, or modeled spectra. In the modern age of large surveys, data sets will be so large that individual analyses will be unfeasible and machine learning or other statistical techniques will become increasingly important. To accurately train machines, data sets with known properties that cover the entire range of parameter space are needed.

With the advent of the Large Synoptic Survey Telescope (LSST) and many other large surveys, photometric data sets of unprecedented size will be available to astronomers. LSST will not include a spectrograph, and so the characterization of stellar parameters must be based entirely on the available photometric data. In preparation for LSST, Miller (2015) created a machine learning technique, which

was taught to determine metallicities solely from photometric colors, using Sloan Digital Sky Survey (SDSS) stellar spectra with log g, [Fe/H], and T_{eff} measurements from the Segue Stellar Parameters Pipeline (SSPP; Lee et al. 2008). The pipeline, however, is only quoted to be accurate for spectral types F through mid-K (it may be accurate outside this temperature range, but this requires further testing), excluding a large portion of stellar parameter space.

Empirical spectral libraries have a rich history in stellar astronomy (e.g., An Atlas of Digital Spectra of Cool Stars: Turnshek et al. 1985; Pickles: Pickles 1998; ELODIE: Prugniel & Soubiran 2001), but none of them include a very large range of M-star properties. Because of the complex molecular rich atmospheres of low-temperature stars, estimates of log g and [Fe/H] have only become accurate within the last few years (e.g., Rojas-Ayala et al. 2010; Terrien et al. 2012; Mann et al. 2013a; Newton et al. 2014), and were therefore unavailable when these libraries were assembled. The ELODIE library is also limited by its small wavelength coverage (3900 – 6800 Å), which does not include many of the longer-wavelength features necessary for studying low-mass stars' metallicities and surface gravities (e.g., Na I at 8200 Å). Numerous groups have used SDSS to create partial libraries of specific effective temperature regions because of the wide wavelength coverage and vast number of spectroscopic and photometric observations available. In the solar mass regime (4,500 – 7,500 K), Lee et al. (2008) created the Sloan Extension for Galactic Exploration and Understanding (SEGUE) SSPP and estimated T_{eff}, log g, and [Fe/H] for over 100,000 stars. In the low-mass regime, Hawley et al. (2002) first assembled a sample of M, L and T dwarf single object spectra. Bochanski et al. (2007) improved upon the sample by creating co-added templates for active and non-active low-mass stars (M0-L0), and Schmidt et al. (2014) extended the templates through the spectral subtype of L6. Savcheva et al. (2014) expanded the library further by compiling

co-added templates of low-mass (and low-metallicity) subdwarfs. However, there is no single source library that covers parameter space in the low-mass regime (M dwarf metallicities and surface gravities).

Synthetic template libraries are also used widely throughout astronomy and are extremely useful tools, since parameters such as log g, [Fe/H], and T_{eff} are model inputs and can span a wider parameter space than any empirical template library. Many of these complete model libraries are available to the public (e.g., Kurucz: Kurucz 1979; BT Settl: Allard et al. 2012). However, the models must use simplifications such as assumptions of plane parallel atmospheres, local thermal equilibrium, etc., to create these synthetic spectra (Husser et al. 2013). Synthetic stellar spectra are also limited because of incomplete lists of line opacities and a lack of knowledge of input parameters for pressure broadening models (Allard et al. 2012; Husser et al. 2013). This is especially problematic for the complex, molecular-rich atmospheres of low-mass stars, where the model spectra do not exactly match the observed spectra across all wavelengths. Empirical libraries are therefore still extremely important both to constrain models and to use in regimes where the models are limited.

In this chapter, I present a library of empirical stellar spectra for spectral types O5-L3, focusing solely on the lower-mass templates. For more detail on how the higher mass templates were created see Kesseli et al. (2017). My library separates out luminosity classes (dwarf and giant) for spectral types A0 through M8, and contains metallicity bins for spectral types A3 through M8. I do not include white dwarfs in my sample; several catalogs of SDSS white dwarfs can be found in other studies (e.g., Kleinman et al. 2013). This stellar template library spans stellar parameter space and contains wavelength coverage that is not available in other empirical libraries. Along with the templates, I have released a revised version the “Hammer" spectral

type facility (Covey et al. 2007a), dubbed “PyHammer". The original code assigned an automatic spectral type by measuring a variety of spectral lines/features and performing a least-squares minimization. The code also allowed the user to complete visual spectral fitting. I have rewritten the code in Python, using my templates for comparison, and I have augmented the code to assign a metallicity, in addition to a spectral type. I have also included a GUI for visual spectral typing.

2.2 Methods

I created the templates via co-addition of individual stellar spectra from Sloan Digital Sky Survey's (SDSS) Baryon Oscillation Spectroscopic Survey (BOSS). BOSS contains over 500,000 well-calibrated stellar spectra spanning wavelengths 3,600 – 10,400 Å at a resolution of $R \sim 2000$ (Covey et al. 2007b). To create the empirical catalog I selected and co-added spectra in bins of metallicity ([Fe/H]), surface gravity, and spectral type.

To ensure the quality of all of the spectra and photometry, I applied some basic quality cuts within my initial SDSS CasJobs Query[1]. I measured the signal-to-noise in each of the five photometric bands, and I included the object if the median value of the five signal-to-noise values (from each band) was greater than ten. I also required that the spectra to be classified as stars (not galaxies or QSOs). I required that the errors in the photometry be less than 0.1 mag in each individual band that is included in the final co-added photometry, and that the photometry in that band was not flagged for being deblended, contaminated by a cosmic ray, or saturated. Finally, I required the extinction in the r-band to be less than 0.25 mag for the object to be included. I found that this latter requirement effectively removed any spectra that were visibly altered by extinction.

[1] http://skyserver.sdss.org/CasJobs

Once the spectra were selected, I visually classified each of the spectra using the “Hammer" spectral type facility (Covey et al. 2007a). I then calculated a radial velocity (Section 2.2.1) to shift each spectrum into its rest frame before further spectral analysis and/or co-addition. I separated the spectra into metallicity (Section 2.2.3) and surface gravity (Section 2.2.2) bins when applicable. There are some holes in the template coverage across parameter space, where I could not find BOSS spectra at all the metallicity/spectral type/surface gravity values. Once separated, each spectrum was cataloged and co-added to create empirical spectral templates (Section 2.2.4).

In the following sections I only discuss the techniques I used to estimate parameters of the M-type stars. I discuss all the other spectral types in the published version of the paper (Kesseli et al. 2017).

2.2.1 Radial Velocity

To determine the radial velocities, I chose to perform my own cross correlation with the M dwarf template library from Bochanski et al. (2007), for spectral subclasses K5 through M9, and Schmidt et al. (2014) for the L dwarfs. The cross correlation method examines three regions of the spectrum (5000–6000 Å, 6000–7000 Å, and 8000–9000 Å), and for each region performs a cross correlation. The minimum of the cross correlation function is recorded, and a sigma clipped median of the measurements from all the regions is reported as the radial velocity. I calculated an uncertainty from the standard deviation of all the individual radial velocity measurements (in each region) added in quadrature with the precision at which radial velocities can be calculated from BOSS’s spectral resolution. I take this radial velocity precision to be $\sim$ 7 km s^{-1} as determined by Bochanski et al. (2007) in a comparison with high precision radial velocity measurements of Hyades cluster members. In the comparison with the Hyades cluster, Bochanski et al. (2007) found

radial velocities that were on average 4 km s^{-1} more precise than the standard SDSS pipeline's radial velocities. For the templates with a signal-to-noise ratio (SNR) > 10 I found a median uncertainty of 9 ± 0.5 km s^{-1}. The radial velocity code used to compute these values will be available with the PyHammer code. Further descriptions of the code, and tests of its accuracy are given in Section 2.4.

2.2.2 Surface Gravity

To distinguish low-temperature dwarfs from giants I followed the steps in Bochanski et al. (2014). Since giants are intrinsically bright, and thus have to be at large distances in SDSS, they will not exhibit observable proper motions. To isolate main sequence stars, I required that the proper motion in RA or Dec be greater than two times the error in the proper motion, while the giant stars must have proper motions less than two times the error in the proper motion. This proper motion cut, however, introduces a high percentage of extra-galactic source contamination in the giant category because elliptical galaxies' spectra often resemble M stars (since M giants are the main observable constituent), and also will not have any measurable proper motion. Bochanski et al. (2014) note this problem in isolating M giants, and use a $g - i, i - K$ color cut (Equation 5 in Bochanski et al. 2014), which Peth et al. (2011) show effectively separates the two populations. Main sequence and giant stars also occupy distinct locations on the $J - K, J - H$ color diagram (Bessell & Brett 1988). To use the IR color cuts (Equations 1 – 3 in Bochanski et al. 2014) that make use of the dwarf-giant distinction in IR color space, I matched all of the SDSS targets with the corresponding targets from the Two micron All-Sky Survey (2MASS). This provided me with J, H, and K-band photometry for each object. Bochanski et al. (2014) concluded that using all of the M giant photometric and proper motion cuts returns approximately $\sim 20 - 50\%$ M giants (contaminants include dwarfs, galaxies, and other sources). Contamination in the M dwarf category should be minimal, since

any giant close enough to have a measured proper motion would saturate the SDSS detectors.

To remove the remainder of the non-giant contaminants from my M giant category, I resorted to visual inspection of the spectra. I found a few carbon star and extragalactic sources, which could easily be identified spectroscopically. To spectroscopically distinguish dwarfs from giant stars, I focused on the gravity sensitive features, Na I (8200 Å) and the calcium triplet (∼8600 Å). The Na I doublet is extremely sensitive to gravity (Schlieder et al. 2012) and is only strong in dwarf stars, while the calcium triplet is more prominent in giant stars (Jones et al. 1984). After my spectroscopic classification, I conservatively removed $\sim 75\%$ of the selected stars and I expect the vast majority of my remaining spectra are true M giants.

2.2.3 Metallicity

Low mass stars' molecule rich atmospheres and distinct lack of a true continuum make it extremely difficult to measure metallicities. Recent work using M dwarfs with wide binary FGK companions has led to several new techniques for estimating M dwarf metallicities. Mann et al. (2013a) used ~ 120 absorption features in K5 through M4 dwarfs to estimate metallicities to a precision of < 0.1 dex for the metallicity range $-1.04 <$[Fe/H]$< +0.56$. I employed the Mann et al. (2013a) method and measured metallicities for over 3,000 individual M dwarfs (no giants) with spectral types through M4. Each spectrum was then separated into a metallicity bin: [Fe/H] < -1.0; -1.0 < [Fe/H] < -0.5; $-0.5 <$ [Fe/H] < 0.0; $0.0 <$ [Fe/H] < 0.5; and [Fe/H] > 0.5.

The majority of methods for determining the metallicity for late-type M dwarfs (M5-M8) use IR spectral features (e.g., Mann et al. 2014; Newton et al. 2014), which are not within the BOSS spectral coverage. Newton et al. (2014) also showed that the spread in the $J-K$ color around the stellar locus in a $J-K, H-K$ color diagram

is primarily due to metallicity. I therefore separated the M dwarf spectra (again, not giants) into rough metallicity bins using IR color cuts from Equation 15 in Newton et al. (2014), which have a precision between 0.1 dex and 0.5 dex. I created three metallicity bins: [Fe/H] < -0.5; $-0.5 <$ [Fe/H] < 0.0; and [Fe/H] > 0.0. Even though the uncertainties are relatively high, the overlap between the high and low metallicity bins should be minimal since the difference in metallicity between the low and high metallicity bin is greater than the 0.5 dex uncertainty stated by Newton et al. (2014).

2.2.4 Co-adding

The BOSS spectra are logarithmically spaced and in vacuum wavelengths. Using the radial velocities determined as described above, I shifted all of the spectra into their rest frames. I used a similar method to Bochanski et al. (2007), except my wavelength grid was spaced evenly in logarithmic space (intervals of 5 km s^{-1}) instead of linearly spaced. The flux was then inserted (without interpolation) into the appropriate location on the flux grid corresponding to the shifted wavelength. The flux grids were then normalized to the flux at 8000 Å. The spectral resolution is increased in this process because the shifts in radial velocity can be measured to precisions of $\sim 5 - 10$ km s^{-1} and were added into a grid with a spacing of 5 km s^{-1}. The process is essentially combining many low resolution spectra into a higher resolution template, and is similar to the “drizzle" process used to combine astronomical images (Bochanski et al. 2007). During the co-addition, I also corrected for a spike in flux located around 5600 Å present in many of the spectra, caused by stitching the spectra from the red and blue BOSS cameras together. Finally, I trimmed the grids at 3650 Å and 10200 Å, to avoid areas that were not complete after the radial velocity shifts. I also propagated the uncertainty reported by BOSS for each spec-

trum throughout this process and calculated the standard deviation of the co-added templates at each spectral channel for each template.

2.3 Stellar Template Library

Here, I present 324 templates of spectral types O through M. One template of each spectral type is shown in Figure 2.1. A subset of the template spectra are shown in Table 2.1; the full table is available for download in the online journal. Each entry displays the number of BOSS spectra co-added to create the template, along with measurements of 29 spectral indices. The spectral indices, which are ratios of the flux in the region of the absorption feature divided by the continuum flux, are the features used by `PyHammer` to estimate the spectral type and metallicity. Figure 2.2 shows a subset of the template spectra for the lowest mass templates. All of the spectra are available in fits formats online[2]. For those interested in the complete sample, all the individual BOSS spectra co-added for each template are available in a Zenodo repository[4], organized by the spectral type, luminosity class, and metallicity. Figure 2.3 shows an M2 spectrum with all of the prominent absorption features labeled.

Figure 2.4 shows an expanded view of the Ca II K and Na I D metal sensitive features in different regions of the spectra (3933 and 5890 Å, respectively). The Ca II K line is prominent in high-temperature stars, while the Na I D lines are almost absent. In low-temperature stars, the trend is the opposite. I found that the Na I D lines are a useful metallicity indicator for F through early M-type stars, and the Ca II K line is a useful metallicity indicator for A and F stars. The higher metallicity spectra have deeper absorption features (larger equivalent widths) for both of these features. In the bottom panel of Figure 2.4, the lowest metallicity templates also

[2]github.com/BU-hammerTeam/PyHammer
https://doi.org/10.5281/zenodo.344471
[4]https://doi.org/10.5281/zenodo.344471

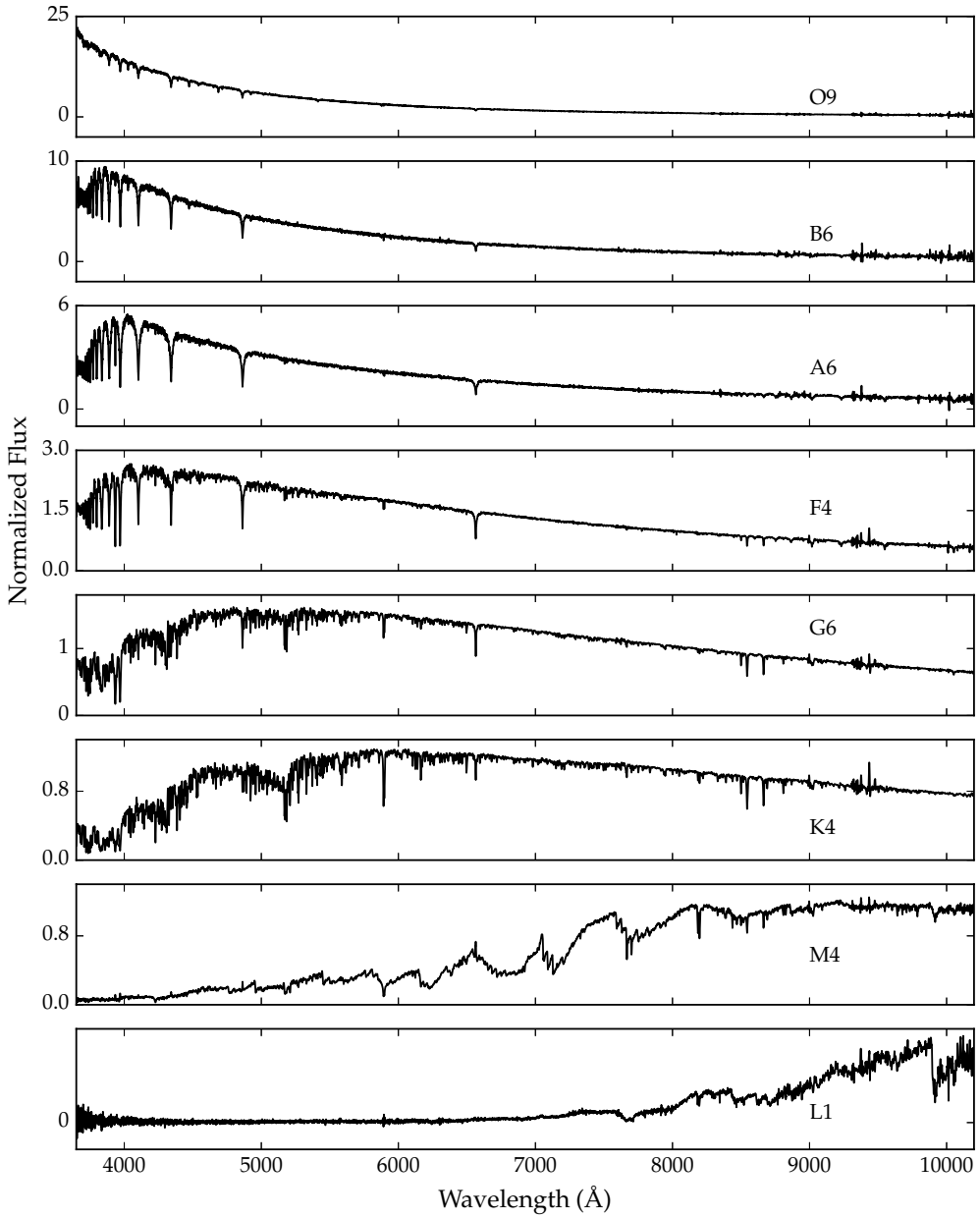

Fig. 2.1: Example of one spectrum per spectral type, where each spectrum is at solar metallicity (if applicable) and classified as a dwarf (if applicable). The spectra are all normalized at 8000 Å.

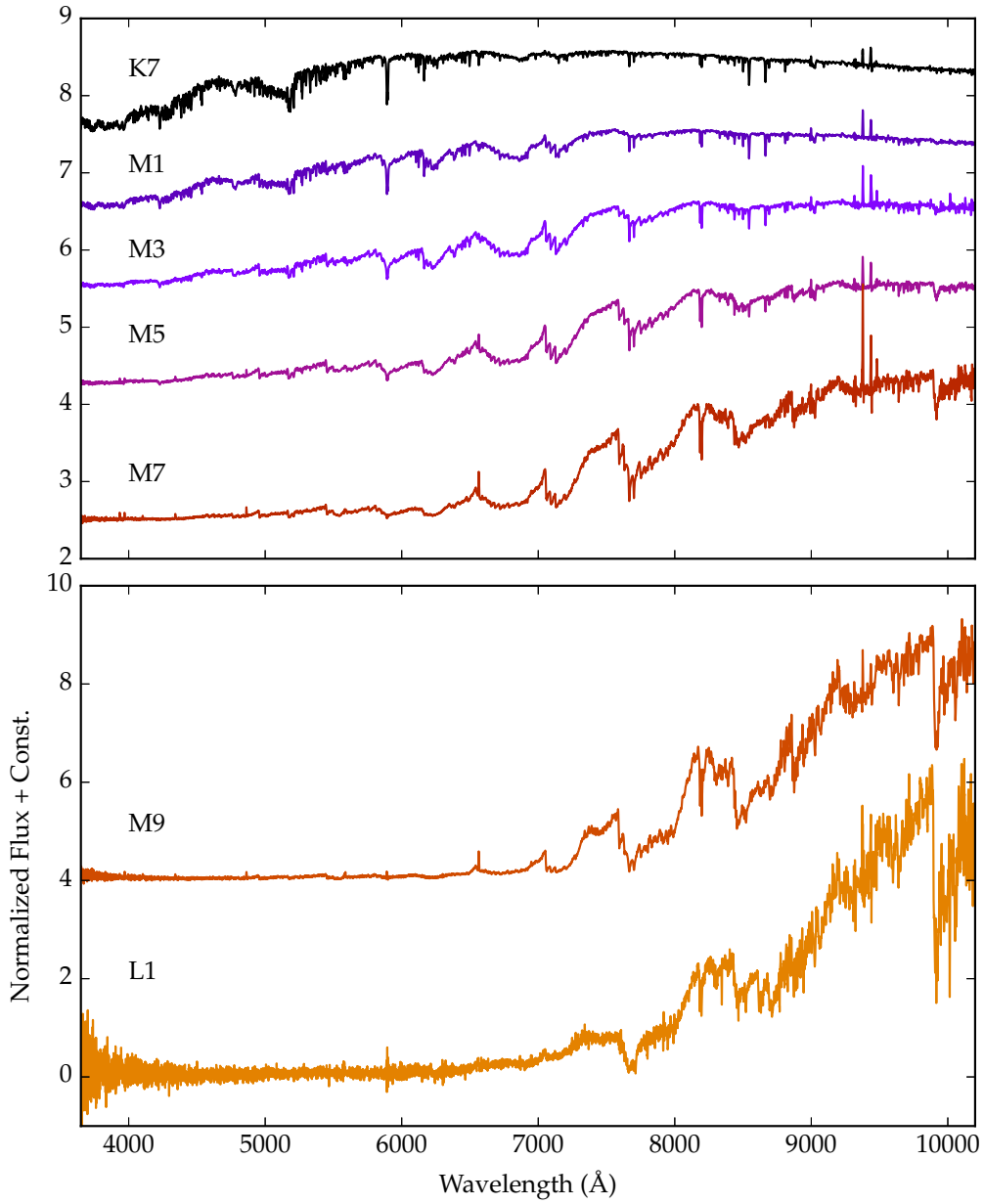

Fig. 2.2: Sample of the template spectra for the main-sequence, low-mass spectral types at solar metallicity ([Fe/H] = 0.0). The spectra are all normalized at 8000 Å, and a constant is added to each template to improve readability. The late-type M and L stars have different scales because most of their flux is concentrated redward of 8000 Å, where the normalization occurs. I therefore put them on a separate set of axes, so they would not dominate the other low-mass stars. All of the low-temperature templates are available in FITS format in the online journal

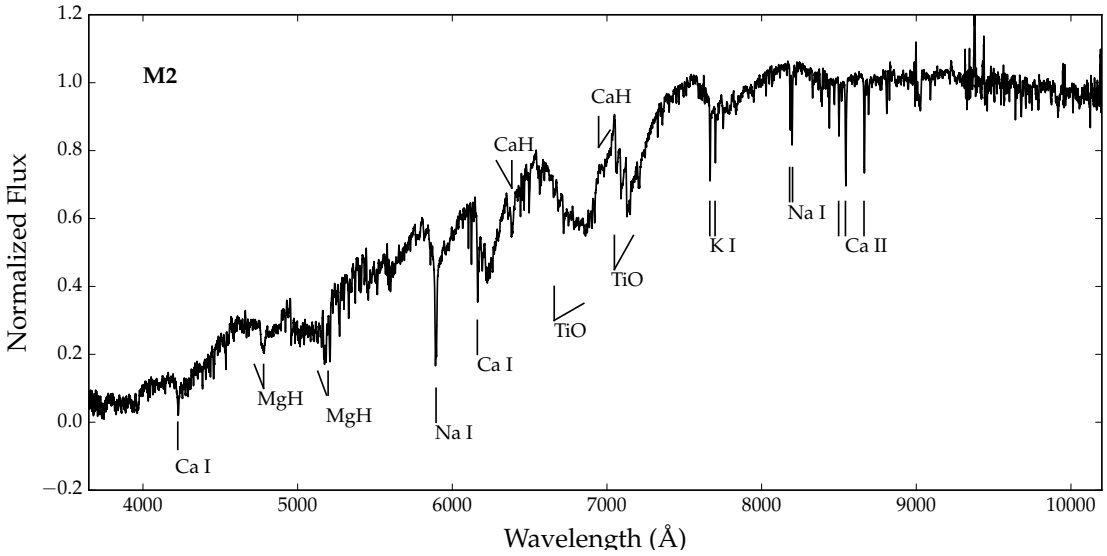

Fig. 2.3: Example of a main-sequence, low-mass (M2) spectrum with solar metallicity ([Fe/H] = 0.0). All the prominent absorption features are labeled for each spectrum. The 'V' shapes are used instead of lines to show large molecular bands.

show few features outside of the neutral sodium D doublet and are virtually flat for the F6 and G5 spectra. The K3 and M1 spectra have few low-metallicity spectra that are co-added to create the templates, and are therefore more noisy than their higher metallicity counterparts, yet still show a lack of real absorption features.

Figure 2.5 is similar to Figure 2.4 except it shows differences between dwarf and giant spectra for a range of spectral types. The top panel of Figure 2.5 shows the entire spectrum for both a dwarf and a giant for the spectral classes G5, K3 and M0. The continua (even without features) are slightly different, with more flux in giants coming from the red end, and more flux in the dwarfs coming from the blue end of the spectrum. The bottom panels show a closer look at three absorption features, which which are sensitive to surface gravity (bottom left: Mg b/MgH and Na I D, bottom right: Ca II triplet). The Mg b and MgH feature around 5100 Å is absent in metal poor giants, weaker in Population I giants as compared to dwarfs, and prominent in dwarfs (Helmi et al. 2003). The M giant does not include a metallicity estimate,

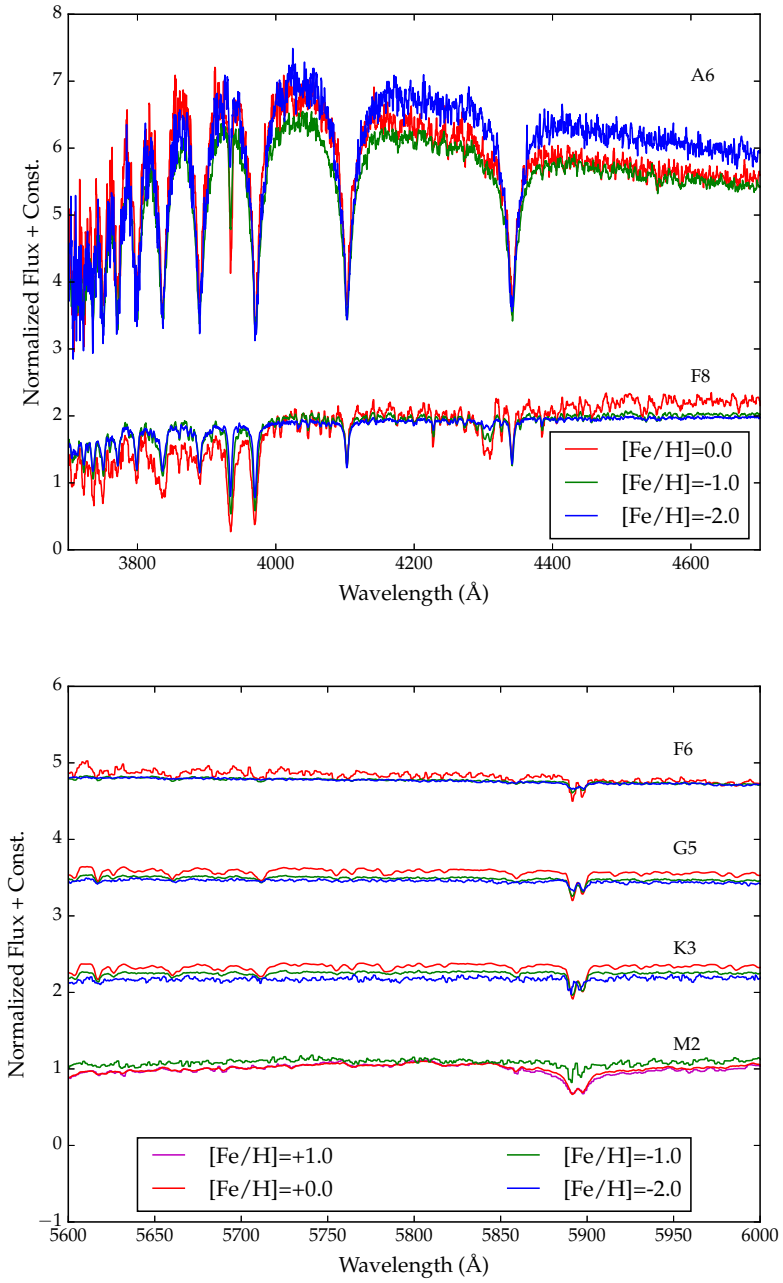

Fig. 2.4: Metallicity variations for a range of spectral subtypes, shown in two different wavelength regions. The top panel shows the region around the Ca II H and K lines ($\sim$ 3940 Å), which are metallicity sensitive for the higher temperature stars (A6, F8). The bottom panel shows the region around the sodium doublet ($\sim$ 5900 Å), which is metallicity sensitive for the spectral subclasses around F through early M-type stars. The equivalent widths of this particular sodium doublet (Na I D) are smaller for late-type M stars, making it difficult to use the feature to distinguish metallicity. The templates of the same spectral classes have no added constants to the flux, but the templates of different spectral classes have an added constant for readability.

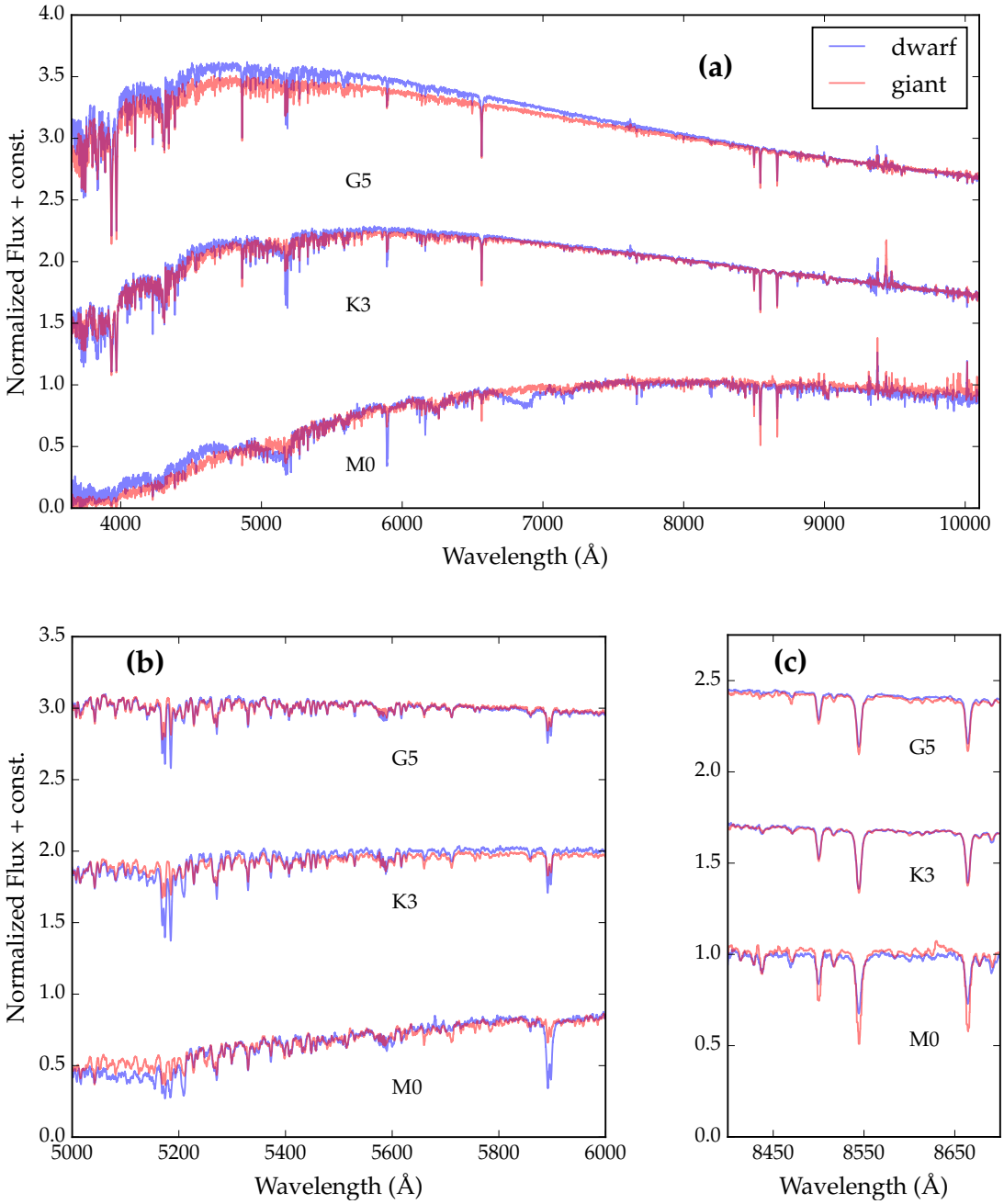

Fig. 2.5: Surface gravity comparison between dwarf and giant templates of the same metallicity ([Fe/H] = -1.0 for the G5 and K3, [Fe/H] = -0.5 for the M0 dwarf, unknown metallicity for M0 giant). The red line shows the giant template, and the blue line shows the dwarf template. Panel **(a)** shows the entire spectrum, while panel **(b)** shows the expanded region around the Na I D lines (5900Å) and Mg b/MgH feature (5200Å), and panel **(c)** shows the zoomed in region around the Ca II triplet. All of these lines are known to be sensitive to surface gravity, which is confirmed in my templates.

Table 2.1. The Template Spectra

File Name	Number of Co-Added Spectra	CaK	NaD[1]	Halpha	TiO8440
O5	10	1.015	1.013	0.892	0.912
B6	5	0.986	1.019	0.834	1.029
A6_-0.5_Dwarf	3	0.953	1.003	0.788	0.979
F6_+0.0_Dwarf	29	0.648	0.965	0.881	0.985
G6_-1.5_Giant	13	0.587	0.975	0.922	0.987
K5_-0.5_Dwarf	11	0.588	0.781	0.954	0.991
M4_+0.5_Dwarf	7	1.010	0.672	1.053	0.902
L1	34	0.613	1.391	1.043	0.683

[1]spectral indices for any doublets (e.g., Na I D) are for the blended feature and therefore include both lines

but because the Mg/MgH feature is absent, I assumed it is a sub-solar metallicity giant. The Na I D lines are also often used as an age indicator since the feature is extremely strong in dwarfs and nearly non-existent in giants (Schlieder et al. 2012). Alkali atoms in general are all extremely sensitive to density because the sole valence electron can easily be perturbed by small changes in pressure (Schlieder et al. 2012), making sodium transitions good surface gravity (and age) indicators. Lastly, the equivalent width of the calcium triplet around 8600 Å is known to be larger in giants than in dwarfs (Jones et al. 1984), which my spectra show in the bottom left panel.

In the sample, I found low-metallicity K giants, but no high-metallicity K giants or late-type M giants (of any metallicity). Stellar evolution models show that low- and high-metallicity giants occupy two different temperature regimes. Stars with lower metallicity become hotter giants since they cannot cool as efficiently, while higher metallicity giants can cool more quickly and therefore occupy the late-type M giant regime (Girardi et al. 2004; Bressan et al. 2012). With the stellar evolution

models in mind, the lack of late-type giants is expected in the SDSS data; there is a strong bias in the metallicity of the giants that can be observed with SDSS. Because of the sight lines observed in the SDSS footprint, the most distant stars (i.e., giants) are located at high Galactic latitudes. The stars located at large distances above the Galactic plane are on average between 0.5 and 1.0 dex more metal poor than their closer counterparts (West et al. 2011). Therefore, in SDSS I did not expect to see many (high metallicity) M-type giants, which is validated by Covey et al. (2008) who found that less than 2% of stars redder than a spectral type of K5 in a magnitude limited SDSS field were giants.

Along with the spectra, I report average photometric colors for each template. Table 2.2 shows a sample of my templates with the photometry information. The full table, which includes each template with all of the color information and associated uncertainties, is available to download in ascii format in the online journal. The colors are averaged over each individual spectrum co-added in a template, after those with bad photometry are removed (i.e., flagged for being deblended, containing a cosmic ray, or saturated). The RMS is the standard deviation of all of the colors for the individual spectra, and the σ is the propagated uncertainty in photometry provided by SDSS. On average, the low metallicity templates have bluer colors than the high metallicity templates. A comparison with Covey et al. (2007a) indicates that the colors are comparable.

From Figure 2.6 it is clear that low-metallicity stars are bluer on average. The overall trends (ignoring metallicity) are almost identical to those shown in Covey et al. (2007a), however when metallicity information is added, the spread in the main sequence is almost entirely due to metallicity. The top two plots in Figure 2.6 show an especially significant distinction between the low and high-metallicity stars, which demonstrates that the u-g color is extremely useful for differentiating

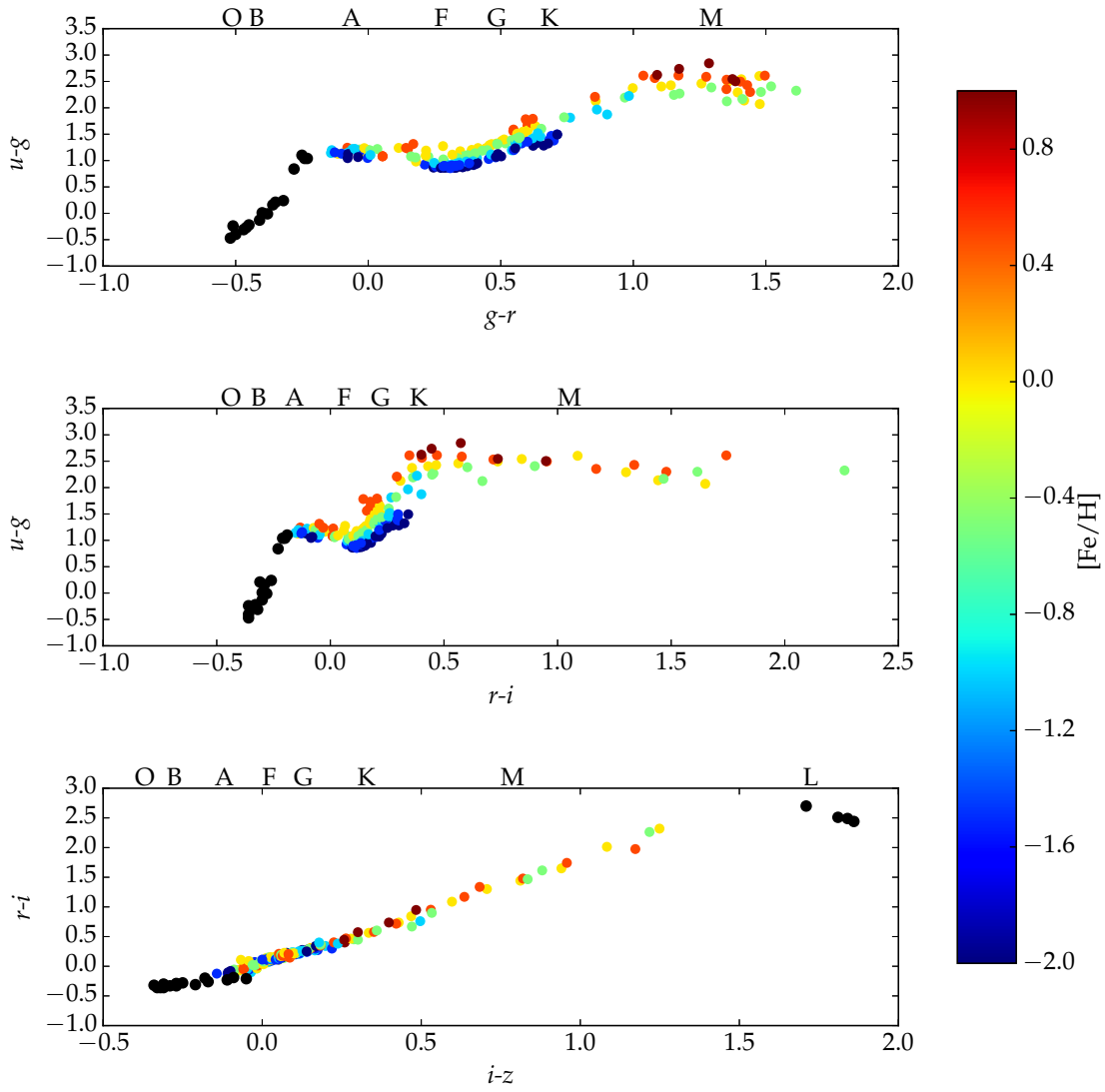

Fig. 2.6: Color-color diagrams for the photometry of all of the main sequence templates. Each template is colored by its metallicity, except for the O5-A2 and L star templates, which are not separated by metallicity bins, and are colored black. A comparison with Covey et al. (2007a) shows similar results. There is a clear trend with metallicity, especially in the top two plots, where lower metallicity templates show bluer colors on average compared to the high-metallicity templates of the same spectral type. Only the three color space combinations that display the most separation among metallicity bins are plotted here.

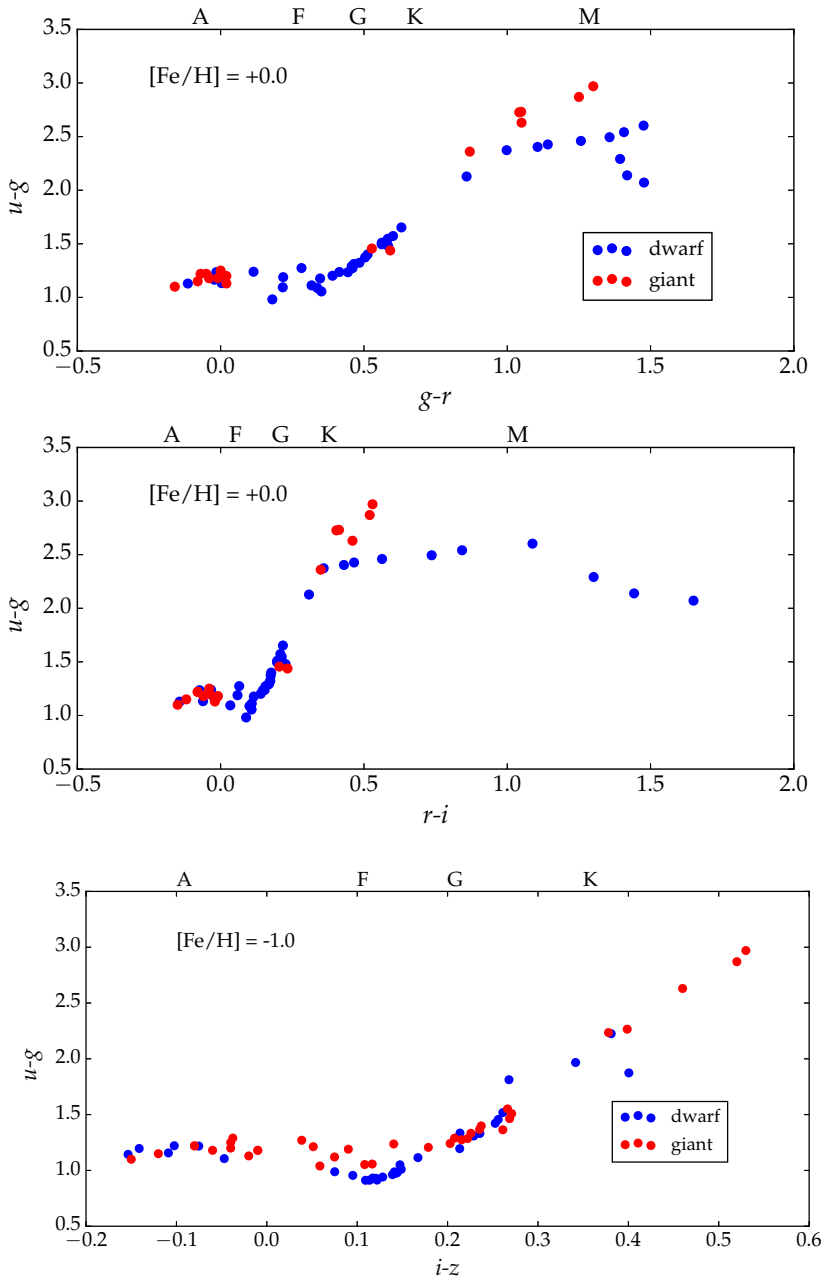

Fig. 2.7: Color-color diagrams showing the main sequence (dwarf; blue) versus giant (red) luminosity classes. To compare the two accurately I only show a single metallicity bin in each plot (top two: [Fe/H] = 0.0, bottom: [Fe/H] = -1.0). Some of the giants (A type and M type) are not separated by metallicity and are shown in all figures. The giants show significant deviation from the dwarfs at spectral types later than mid-K for all metallicity bins available. In the bottom plot, the F stars show a similar trend in the *u-g* vs *i-z* color-space, and are noticeably separated from the dwarfs. There is no clear separation in color-space for the G or A giants, and they are indistinguishable from the dwarfs in all of my plots.

metallicities. This trend is valid from F dwarfs through mid-type M dwarfs (∼M4). The A stars seem to follow to the same trend, however the photometry is not as spread out in that region of color-space, making it extremely difficult to distinguish metallicities accurately. Beyond the mid-type M dwarfs, the light emitted in the u-band is too faint to report an accurate u-band measurement. Other studies of stars in the SDSS (e.g., Ivezić et al. 2008) have observed color trends with metallicity in the past, however metallicity information for low-mass stars was not available for those studies.

Figure 2.7 shows three color-color diagrams demonstrating the color difference between luminosity classes. In general, all of the plots show that giants emit more light in redder wavelengths than dwarfs. To ensure this trend is not an effect of extinction, I compared the average extinction of each template in each band (provided by the SDSS database). I found the difference in average extinction between the dwarf and giant templates to be smaller than the propagated errors in extinction provided by SDSS, leading me to conclude that any significant change in color is not an effect of extinction and is, therefore, a real physical effect. For the higher temperature stars (F/G), the trend only exists for bins of low metallicity because there are not many templates for high-metallicity giants at high temperatures, and for low-temperature stars (K/M) the trend exists only for high metallicities because there are not many low-temperature, low-metallicity dwarf templates. However, with a complete set of data, I expect this trend to persist for all metallicity bins. The greatest separation between dwarf and giant stars occurs in the lowest temperature stars (K/M). K and M stars contain many large molecular features and absorption lines, so this prominent color difference can be attributed to the surface gravity affecting the strength of many of these lines. The higher temperature stars do not show any separation in most cases (A-type, G/K-type), and a slight separation around $i - z = 0.1$ (F-type stars).

2.4 `PyHammer`: A Tool for Spectral Parameter Extraction

In this section, I discuss the automatic and visual spectral typing code, dubbed "PyHammer" in detail. PyHammer is based on the "Hammer" by Covey et al. (2007a). The code automatically outputs best estimates for the radial velocity, spectral type, and metallicity (when metallicity information is available: A3 - M8). Here, I also present the methods for determining these estimates, tests to determine the accuracy/precision of these methods, and the resulting accuracy for each parameter that is determined. The is also a visual, or "by-eye", spectral typing feature of PyHammer allows the user to visually compare the input spectrum to any of the template spectra in a GUI window. The `PyHammer` code is available for the public on GitHub[5].

The general procedure of the code is to first interpolate the input spectrum onto the same wavelength grid as my templates and convert to vacuum wavelengths (if necessary) to allow for direct comparison. Then, I measure spectral indices and color regions and I make an initial estimate of the spectral type using these indices. With my initial spectral type estimate, I can determine the radial velocity by cross correlating the spectrum with the corresponding template. I then shift the input spectrum to its rest frame, and re-measure the 34 spectral indices to determine a more accurate estimate of the spectral type and metallicity.

The radial velocity cross correlation method is based on an IDL procedure `xcorl` (Mohanty & Basri 2003; West & Basri 2009), which was translated into python by Theissen & West (2014). The cross correlation method examines three regions of the spectrum (5000-6000 Å, 6000-7000 Å, and 7000-8000 Å), and performs a cross correlation for each region. The shift that produces a minimum in the cross-correlation

[5]github.com/BU-hammerTeam/PyHammer

Table 2.2. Photometry of Templates

Sp Type	[Fe/H]	u-g	RMS_{u-g}	σ_{u-g}	g-r	RMS_{g-r}	σ_{g-r}	r-i	RMS_{r-i}	σ_{r-i}	i-z	RMS_{i-z}	σ_{i-z}
O5V	-	-0.24	0.14	0.02	-0.51	0.02	0.02	-0.36	0.02	0.02	-0.31	0.02	0.02
O7V	-	-0.31	0.05	0.01	-0.47	0.01	0.01	-0.32	0.01	0.01	-0.34	0.02	0.02
A3V	+1.0	1.2	0.04	0.02	-0.02	0.05	0.02	-0.08	0.01	0.02	-0.05	0.04	0.03
A3V	0.0	1.17	0.01	0.01	-0.07	0.03	0.01	-0.12	0.02	0.01	-0.07	0.02	0.01
A3V	-0.5	1.12	0.04	0.02	-0.09	0.02	0.01	-0.1	0.02	0.01	-0.09	0.02	0.02
G2V	0.0	1.23	0.04	0.01	0.44	0.02	0.01	0.15	0.01	0.01	0.07	0.01	0.01
G2V	-0.5	1.19	0.03	0.01	0.43	0.01	0.01	0.16	0.0	0.01	0.06	0.01	0.01
G2V	-1.0	0.97	0.01	0.01	0.41	0.02	0.01	0.14	0.01	0.01	0.05	0.01	0.01
G2V	-2.0	0.95	0.04	0.01	0.41	0.02	0.01	0.18	0.02	0.01	0.08	0.01	0.01
M0V	1.0	2.84	0.05	0.04	1.29	0.05	0.01	0.57	0.03	0.01	0.3	0.02	0.01
M0V	0.5	2.59	0.03	0.01	1.28	0.01	0.0	0.58	0.01	0.0	0.35	0.01	0.0
M0V	0.0	2.46	0.03	0.01	1.26	0.01	0.0	0.56	0.01	0.0	0.33	0.01	0.0
M6V	0.5	2.61	0.02	0.02	1.5	0.0	0.0	1.74	0.0	0.0	0.96	0.0	0.0
M6V	0.0	2.07	0.0	0.03	1.48	0.01	0.0	1.65	0.01	0.0	0.94	0.0	0.0
M6V	-0.5	2.3	0.05	0.02	1.48	0.01	0.0	1.62	0.01	0.0	0.88	0.01	0.0
F0III	-0.5	1.25	0.01	0.02	0.27	0.0	0.01	0.07	0.02	0.01	0.05	0.0	0.02
F0III	-1.0	1.21	0.03	0.01	0.2	0.03	0.01	0.05	0.02	0.01	0.01	0.01	0.01
F0III	-1.5	1.16	0.05	0.01	0.18	0.03	0.01	0.04	0.02	0.01	0.02	0.01	0.01

function is recorded and a sigma-clipped median of the measurements from all the regions is reported as the radial velocity.

To test the radial velocity code, I compared the measured radial velocities to previously measured radial velocities across the full spectral range. To validate the radial velocities for the low-temperature stars, I compared the radial velocities of the West et al. (2011) sample of M dwarfs, derived by cross correlation with Bochanski et al. (2007) M dwarf templates, to my measured radial velocities. The M dwarf radial velocities reported in the sample (BOORV field) are accurate to $\sim$10 km s^{-1}. For the higher temperature stars, I compared my radial velocities to the radial velocities derived from the SDSS pipeline, which are accurate to 10 –15 km s^{-1}, making this comparison the least accurate. The results are shown in Figure 2.8.

To assign an initial estimate of the spectral type and metallicity, I compared the input spectrum to the template spectra in the following manner. I first measured 34 spectral indices (Table 2.3) from each individual spectrum that was used to create the templates. For all spectra of a given spectral type and metallicity (i.e., each template), I measured the weighted mean and variance of each index for all of the co-added spectra, where the weight is the variance in the index value due to uncertainties in the observed spectrum. I repeated this process for all spectral types and metallicities. To reduce computation time, the results of this procedure were saved to an external file and not repeated each time the code was run.

I compared the input spectrum to each template by computing a chi-squared value that compares the spectral indices measured from the input spectrum to the weighted mean indices described above. The variance used in the chi-squared calculation is the variance among indices of multiple stars of the same template type as described above. I reported the spectral type and metallicity of the template that produces the minimum chi-squared as the initial estimate. I chose to use indices

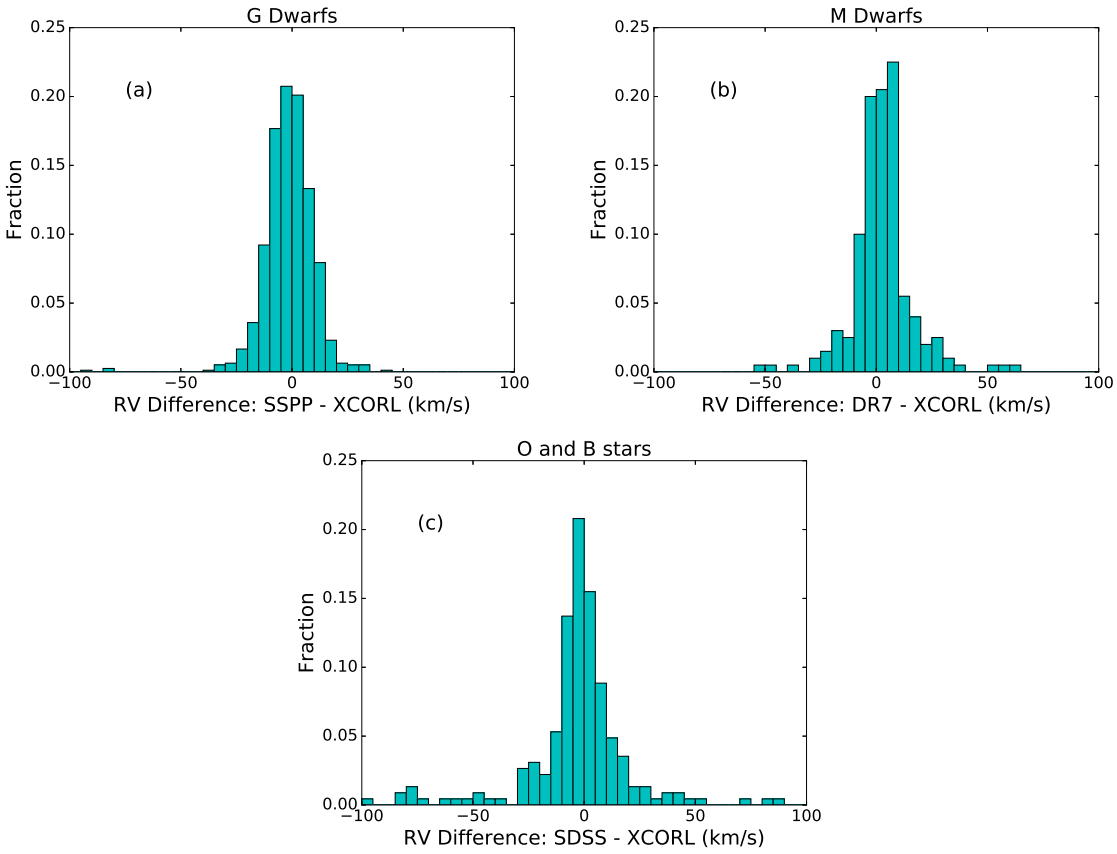

Fig. 2.8: Comparison between my measured radial velocities and **(a)** the radial velocities determined by the SSPP for the G dwarfs, **(b)** by cross correlation with Bochanski et al. (2007) templates using West et al. (2011) DR7 sample for the M dwarfs, and **(c)** the SDSS pipeline for the O and B stars. The radial velocities for the G stars have a median difference of -1 km s^{-1} and "1-sigma" (68%) of the data falls between -10.0 and 7.9 km s^{-1}. The M dwarfs have a median difference of 2 km s^{-1} and 68% of the data fall between -7.1 and 10.8 km s^{-1}. The O/B stars are significantly more spread out, and have a median difference of -1.6 km s^{-1}, with upper and lower limits of "1-sigma" at -22.7 and 10.7 km s^{-1}. My radial velocity measurements are therefore comparable in uncertainty to the previous methods for calculating radial velocities.

instead of doing a chi-squared minimization of the entire spectrum because spectral indices are normalization independent, robust against missing data, and take less computational time.

I tested the automatic spectral typing by running the code on the individual spectra that were used in constructing the templates and compared the estimated metallicity and spectral type to the actual metallicity and spectral type I determined. The results are shown in Figure 2.9. Both comparisons show good agreement, with over 50% of the estimates exactly the same as the determined spectral types and metallicities. The spread in both comparisons is also extremely small, with the standard deviation being 1.5 spectral subtypes in the spectral-type comparison, and 0.4 dex in the metallicity comparison. I conclude that even without the additional visual inspection, the automatic spectral typing and metallicity estimates are within one metallicity bin and one spectral subtype over 80% of the time.

Detailed instructions on running PyHammer as well as more advanced features of the code are provided in the README file in GitHub, and in the 'Help' menu (available when the visual classification GUIs are displayed). Here, I will give a brief overview of how to run the code and a description of some of the features available. After starting the code (type "python pyhammer.py" on the command line), an initial GUI window will appear, allowing the user to enter the name of (or create) the input and output files, specify a path to the spectra files, skip straight to the by-eye spectral typing (as opposed to doing the automatic spectral typing first), and apply a signal-to-noise cut-off. Skipping directly to the eye check stage should only be done if the automatic spectral typing has already been completed at an earlier time. If the user does not skip the automatic spectral typing, the program determines the radial velocity, metallicity and spectral type and writes these to the output file (PyHammerResults.csv by default). If the user supplies a signal-to-noise

Table 2.3. Spectral Indices Used by `PyHammer`

Spectral Index	Numerator (Å)	Denominator (Å)
Ca II K	3923.7 - 3943.7	3943.7 - 3953.7
Hδ	4086.7 - 4116.7	4136.7 - 4176.7
Ca I 4227	4216.7 - 4236.7	4236.7 - 4256.7
G-band	4285.0 - 4315.0	4260.0 - 4285.0
Hγ	4332.5 - 4347.5	4355.0 - 4370.0
Fe I 4383	4378.6 - 4388.6	4355.0 - 4370.0
Fe I 4404	4399.8 - 4409.8	4414.8 - 4424.8
Hβ	4847.0 - 4877.0	4817.0 - 4847.0
Mg I	5152.7 - 5192.7	5100.0 - 5150.0
Na D	5880.0 - 5905.0	5910.0 - 5935.0
Ca I 6162	6150.0 - 6175.0	6120.0 - 6145.0
Hα	6548.0 - 6578.0	6583.0 - 6613.0
CaH2	6814.0 - 6845.0	7042.0, 7046.0
CaH3	6960.0 - 6990.0	7042.0 - 7046.0
TiO5	7126.0 - 7135.0	7042.0 - 7046.0
VO 7434	7430.0 - 7470.0	7550.0 - 7570.0
VO 7445	7350.0 - 7400.0, 0.5625; 7510.0 - 7560.0, 0.4375	7420.0 - 7470.0
VO-B	7860.0 - 7880.0, 0.5; 8080.0 - 8100.0, 0.5	7960.0 - 8000.0
VO 7912	7900.0 - 7980.0	8100.0 - 8150.0
Rb-B	7922.6 - 7932.6, 0.5; 7962.6 - 7972.6, 0.5	7942.6 - 7952.6
Na I	8177.0 - 8201.0	8151.0 - 8175.0
TiO8	8400.0 - 8415.0	8455.0 - 8470.0
TiO 8440	8440.0 - 8470.0	8400.0 - 8420.0
Cs-A	8496.1 - 8506.1, 0.5; 8536.1 - 8546.1, 0.5	8516.1 - 8526.1
Ca II 8498	8483.0 - 8513.0	8513.0 - 8543.0
CrH-A	8580.0 - 8600.0	8621.0 - 8641.0
Ca II 8662	8650.0 - 8675.0	8625.0 - 8650.0
Fe I 8689	8684.0 - 8694.0	8664.0 - 8674.0
FeH	9880.0 - 10000.0	9820.0 - 9860.0
Color Region 1	4550-4650	4160-4210
Color Region 2	5700-5800	4160-4210
Color Region 3	7480-7580	4160-4210
Color Region 4	9100-9200	4160-4210
Color Region 5	10100-10200	4160-4210

[1]Indices with more than one numerator entry contain two numerator regions and a weight for each region, e.g. lower limit of region 1 – upper limit region 1, weight of region 1; lower limit of region 2 – upper limit of region 2, weight of region 2

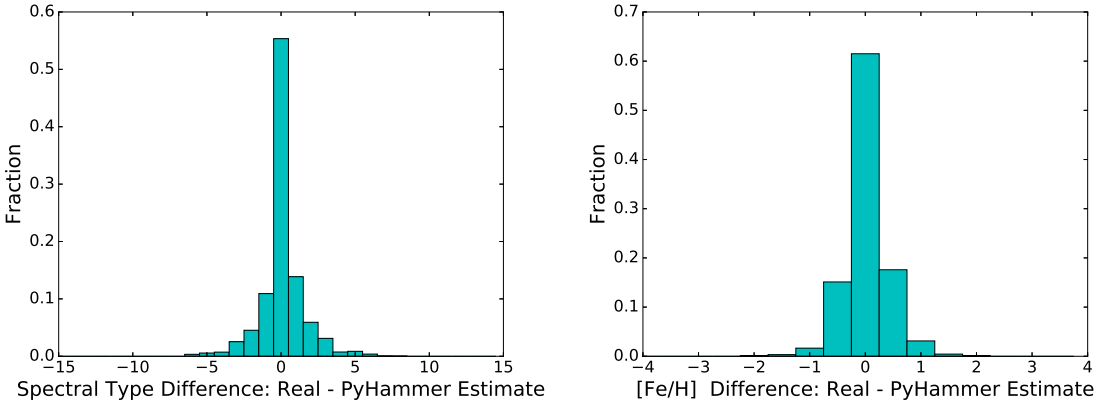

Fig. 2.9: Comparison between the hammer automatically estimated spectral types (left) and metallicities (right) and the actual spectral types and metallicities I determined for the individual BOSS spectra that were used to make the templates. The spectral type estimate returns the correct value more than 50% of the time, and the metallicity estimate returns the correct value upwards of 60% of the time. The spread in the spectral type is extremely small, with a standard deviation of 1.5. The standard deviation in the metallicity is 0.4 dex, which is smaller than one of my metallicity bins.

cut-off, any spectrum with a median signal to noise ratio (calculated simply as the median flux divided by the median uncertainty over the entire spectrum) lower than the specified value is written to RejectSpectra.csv. There is an example input file (exampleInputFile.txt) and a few spectra in the test_case folder to demonstrate how the input file should be set up, and to aid the first time user.

A screenshot of the GUI for the visual spectral typing is shown in Figure 2.10. The GUI allows the user to display the spectra and the templates on the same plot, allowing for direct comparisons. All of the normal matplotlib graphing buttons are functional, and shown in the top left corner of the GUI in Figure 2.10. By pushing the magnifying glass button, the user can zoom in on specific regions of the spectrum. While zoomed in the user can use the four sided arrow to scroll. Finally, by pressing the home button, the graph will be taken to the original view. In the 'Options'

menu at the top of the screen there are four different viewing options for the graph. The user can choose to display or not display the template RMS (in transparent blue). The user can also smooth the spectrum, and lock the smoothing since by default every new spectrum loaded will be unsmoothed. The smoothing option runs a simple boxcar smoothing over the input spectrum, which reduces noise and allows for easier comparisons for low signal to noise spectra. Finally, if the spectra are from the SDSS, the user can choose to remove the known false spike in the spectra at 5580 Å, created by the stitching together of the red and blue ends of the spectra.

Along with simply clicking through different templates on the bottom part of the GUI shown in Figure 2.10, there are many options designed to make visual spectral typing easier. The 'Earlier' and 'Later' buttons change the spectral subtype by one each time, where 'Earlier' scrolls to lower numbered subtypes (e.g., M4 to M3 or M0 to K7), and the 'Later' to higher numbered subtypes. While the 'Lower' and 'Higher' buttons change the metallicity by one bin (0.5 dex) with each click. There are also buttons with other options, which have been adopted from the original Hammer code. The 'Odd' button allows the user to input their own note into the space where the spectral type would normally be stored. I set a few standard 'odd' spectral types like white dwarf (Wd), white dwarf+M dwarf binary (Wdm), carbon star, galaxy (Gal) and unknown, but the user may also type anything he or she would like into this space. Finally, the user can proceed to the next spectrum from their input list or return to a previous spectrum using the 'Back', 'Next' buttons. Each of these buttons also has a keyboard shortcut so the entire visual spectral typing can be done with only a keyboard (to speed up the process). For more information on the keyboard shortcuts go to the 'Help' menu and click on the 'Keys' tab in the PyHammer Help window.

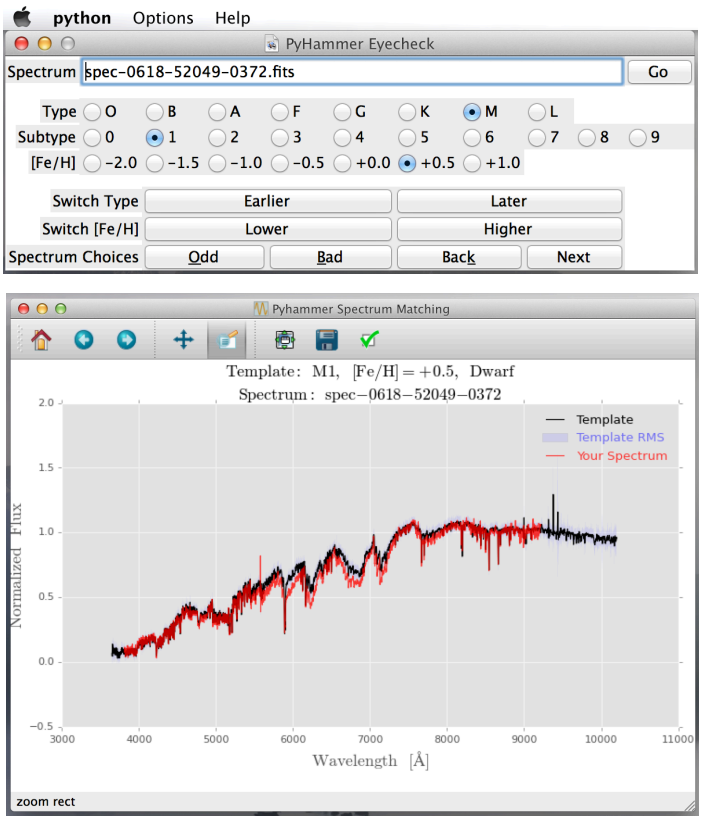

Fig. 2.10: Screenshot showing the two GUIs used for the by-eye spectral typing. The top GUI screen allows the user to display templates of different spectral type and metallicity. The bottom GUI screen initially displays the best guess template (in black), along with the standard deviation from all the co-added individual spectra at each wavelength (in semi-transparent blue). The spectrum from the user's input list is displayed in red.

2.5 Summary

I have compiled a new empirical stellar template library using data taken with the SDSS BOSS spectrograph,. My template library:

- Covers spectral types O5 through L3
- Includes dwarf and giant separation for spectral types A0 through M8
- Contains metallicity [Fe/H] bins for spectral types A3 through M8
- Reports averaged photometric colors (in SDSS bands) for all the co-added stars in each template, along with a propagated errors and standard deviations

Along with the templates, I have released the `PyHammer` code for assigning a spectral type and metallicity automatically (or by visual inspection). This code is based on the "Hammer" spectral typing facility, written by Covey et al. (2007a), but includes metallicity information and is written in Python. The automatic spectral typing portion of code returns the exact spectral type I determined using the original "Hammer" code and the metallicity I determined using the methods described in Section 2.2.3 over 50% of the time. The spread in the spectral type was 1.5 spectral sub-types, and a spread in the metallicity was 0.4 dex. Visual spectral typing allows for direct comparison between input spectra and my empirical templates in an easy to use GUI. The code is available on GitHub[4].

The library of empirical stellar spectra will be important for a wide range of research topics from extragalactic to galactic astronomy, planetary system stellar characterization, and even as an astronomical teaching tool. With large photometric surveys such as LSST, machine learning techniques will become increasingly important for characterizing large amounts of data quickly and efficiently. Along with

[4]github.com/BU-hammerTeam/PyHammer

releasing the templates, I provided lists of the individual BOSS spectra co-added to construct each template. This combination of information will be an ideal training set for machine learning, and can extend the work of Miller (2015) on F, G, and K stars to both higher and lower mass stars. This catalog represents the first empirical template library with metallicity and surface gravity separation for low-mass (M-type) stars. The catalog and the “PyHammer" spectral typing facility will be a useful tool for the community as a whole.

Chapter 3

The Effects of Metallicity on M dwarf Radii

A similar version of this Chapter was published in the Astronomical Journal as Kesseli et al. (2019).

3.1 Introduction

M subdwarfs are low-metallicity M dwarf stars and are identified by their position to the left of the main sequence on a color magnitude diagram (Sandage & Eggen 1959). Their metal-poor compositions are a characteristic of their old age, and therefore M subdwarfs make up a significant portion of the stellar populations of the Galaxy in the halo and bulge (e.g., Gizis 1997; Lépine et al. 2003; Burgasser et al. 2003). As discussed in Chapter 1.6.1, the low metallicity of the subdwarfs is theorized to alter their sizes, and metal-poor stars are expected to have smaller radii than solar-metallicty stars.

Previous studies have discovered and classified many M subdwarfs, but less has been done to determine their physical parameters (e.g., radii and effective temperatures). Gizis (1997) first introduced a classification scheme for M subdwarfs based on the molecular line strength ratios between the optical CaH ($\sim$6830 and 6975 Å) and TiO5 ($\sim$7130 Å) bands and separated M subdwarfs into three categories: the solar metallicity dwarfs (dM), the metal-poor subdwarfs (sdM), and the very metal-poor extreme subdwarfs (esdM). Lépine et al. (2007) increased the sample of known metal

poor M dwarfs to over 400 objects and expanded the classification to include a new even more metal-poor class, ultra subdwarfs (usdM).

Since then, Jao et al. (2008) devised a separate classification scheme for subdwarfs, based on physical parameters (effective temperature, metallicity and surface gravity), by comparing spectra to stellar atmosphere models. Exact values of these physical parameters could not be determined until recently because previous model atmospheres were unable to reproduce many of the molecular features present in the atmospheres of cool stars. However, Rajpurohit et al. (2014, 2016) found that the recently updated PHOENIX stellar atmosphere models (Allard et al. 2012) successfully reproduced many of the features in low metallicity stars and were therefore able to make estimates of the metallicity, surface gravity and temperature of a limited sample of M subdwarfs.

In this Chapter I present stellar radii for a greatly expanded sample of M subdwarf stars. In Section 3.2 I describe how I chose the sample, and I describe my Palomar DBSP observations and data reduction procedure. The radii are calculated by combining $T_{\rm eff}$ and $L_{\rm bol}$ using the Stefan-Boltzmann equation. I detail my method for determining the metallicity in Section 3.3, the effective temperature in Section 3.4, and the bolometric luminosity in Section 3.5. Finally, in Section 3.6 I present color and effective temperature relations that can be used to determine the radii of other M subdwarf stars.

3.2 The Sample

I constructed a grid of bright, nearby subdwarf spectra covering large ranges in spectral type and metallicity, allowing me to fully characterize a broad subset of these objects. Knowledge obtained from this nearby subset can then be used to deduce radii for more distant examples using photometric information alone.

The sample of subdwarfs spans the spectral classes of ∼K7 through ∼M7. I use the Lépine et al. (2007) subdwarf subclasses – subdwarfs (sd), extreme subdwarfs (esd), and ultra subdwarfs (usd) to roughly separate objects in the metallicity ranges $\log([Fe/H]) \approx -0.5$, -1.0, and -1.5, respectively. Many known late-K through late-M subdwarfs were classified before the Lepine et al. system was established, so some were typed against the earlier Gizis (1997) two-subclass system. Others pre-date both of these papers and are classified using a mixture of systems.

Rather than rely on published types, I combed the literature for objects classified as subdwarfs. I identified ∼250 in all, most of which are relatively bright, nearby sources found by various proper motion surveys. I then tabulated their optical, 2MASS, and *WISE* magnitudes. Using the $J - K_s$ vs. $J-$W2 diagram, I plotted these objects together with known dwarfs of solar metallicity, the subdwarf standards of Lépine et al. (2007), and the theoretical subdwarf tracks (see Figure 1 from Zhang et al. 2017) to pseudo-categorize each as d, sd, esd or usd. This color-color diagram is shown in the top panel of Figure 3.1. After removing those that appeared to be solar-metallicity dwarfs and those too far south to be observed with the 200 inch telescope at Palomar, I was able to sort the distribution of candidates by R magnitude and $J-$W2 color, the latter being a proxy for temperature or spectral type. Using this list, I created a target list having three objects in each integral spectral type bin. Three objects per bin were required to mitigate the effects of unresolved binarity on the L_{bol} determination and to have a crude assessment of the cosmic scatter per bin. One object in each bin was chosen to be the Lépine et al. (2007) standard itself, and the other two were generally chosen to be the brightest (and therefore most easily observable) at R band. This final observing list is shown in Table 3.1 as well as in Figure 3.1.

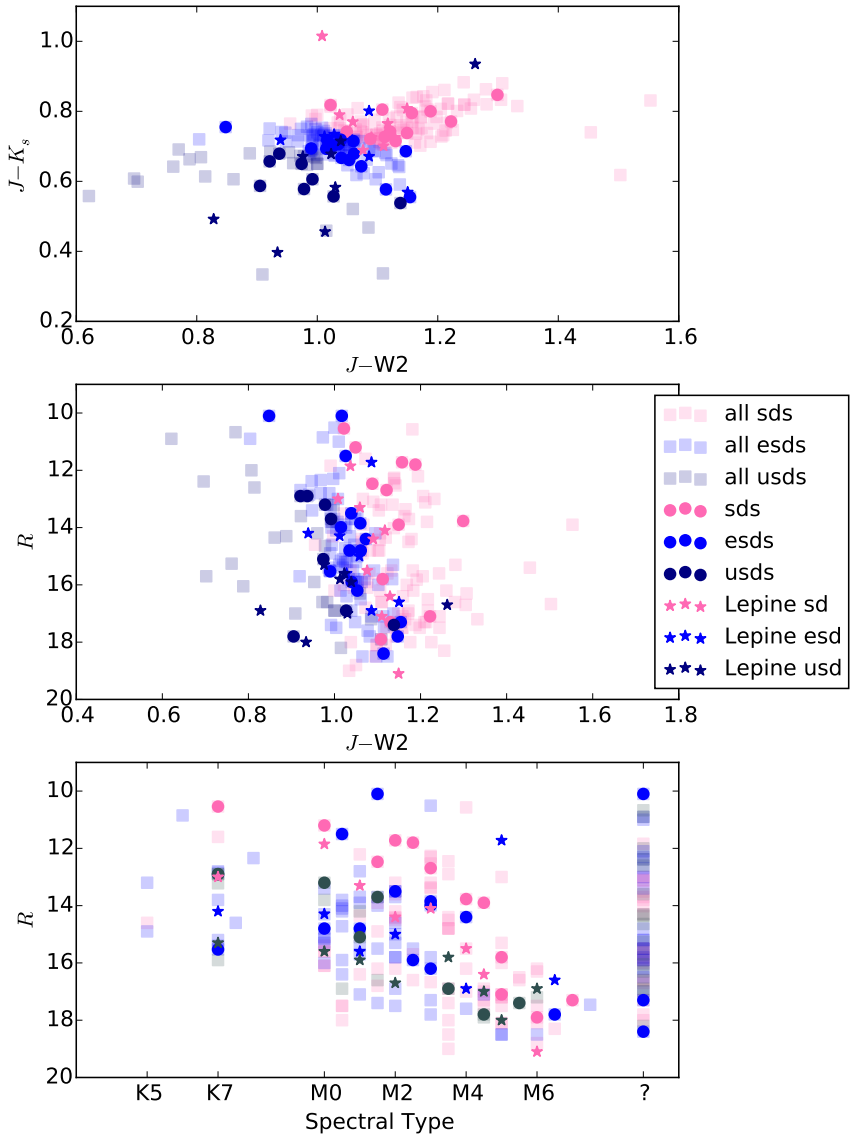

Fig. 3.1: **Top:** $J - K_s$ versus $J-$W2 diagram, used to separate the compiled ∼250 selected subdwarfs into the metallicity classes of d, sd, esd, and usd. The targets ultimately selected are colored circles, the Lépine et al. (2007) subdwarf standards are shown as colored stars, and the full original sample is shown as translucent squares. Note that one of the Lepine usd standards has dwarf-like colors; this star is LHS 1691 and I believe that its 2MASS J-band color is not correct. This star is also an outlier in later figures, such as Figure 3.9. **Middle:** R magnitude versus $J-$W2 color diagram. **Bottom:** R-band magnitude versus spectral type diagram. A target without a known spectral type is shows as a '?' on this plot. This plot illustrates how I tried to target two bright sds, esds, and usds for each spectral type estimate.

Prior to my spectroscopic observations, I created finder charts at the 2017.8 epoch of each source, using the source's 2MASS position and its published proper motion. Any source confused with a bright background source at my epoch was replaced with the next brightest star in the spectral bin. One of the subdwarf standards, LSR J1918+1728 (esdM3), is contaminated at my epoch of observation and was therefore skipped.

In order to facilitate spectral classification comparisons and to provide checks of radius measurements for stars similar to those in Mann et al. (2013b), I observed two to three solar metallicity dwarfs in each spectral subtype bin, as well. These are also listed in Table 3.1.

Data were taken during six separate nights between August of 2017 and January of 2018, using DBSP on the 200-inch Hale Telescope at Palomar Observatory. DBSP is a moderate resolution optical spectrograph that uses a dichroic to split light into separate red and blue channels that are observed simultaneously (Oke & Gunn 1982). The observer can choose from four different dichroics and can choose the grating angle to set the wavelength coverage and spectral resolution. For all of the nights I chose the dichroic that split the light at a wavelength of 6800Å. For the blue side I used a 600/4000 grating and for the red side a 600/10000 grating. I chose grating angles of $\sim 29^\circ$ and $\sim 32^\circ$, leading to a wavelength coverage of $\sim 3900 - 6950$Å and $\sim 6610 - 9970$Å and a mean resolving power of ∼2,000 and ∼3,000 for the blue and red sides, respectively.

I performed all of the data reduction using the python command line tool for IRAF (PyRAF). Bias subtraction, flat fielding, spectral extraction, cosmic ray removal, wavelength calibration and flux calibration were performed on the red and blue images separately. Wavelength calibration frames using a Fe-Ar lamp for the

blue side and a He-Ne-Ar lamp for the red side were taken at the beginning of each night.

The red and blue wavelength scales were separately shifted to rest by cross correlation with a model stellar spectrum of spectral type M1 for the hotter stars and M5 for the cooler stars. I next stitched the spectra together by normalizing the spectra to each other at the stitch point. The stitch point was chosen by visual inspection of each spectrum to be a point with relatively low noise and free of any large absorption features, and with a wavelength between $6650 - 6775$Å.

For a small subset of my targets, I also obtained high resolution near-infrared spectra from iSHELL (Rayner et al. 2012) on NASA's 3.0-meter Infrared Telescope Facility (IRTF) on Mauna Kea, Hawaii. I used the wider slit width, giving a spectral resolution of about R$\sim$35,000 for my chosen wavelength region ($2.09 - 2.38\mu m$). In total I collected spectra of three dwarfs, four subdwarfs, one extreme subdwarf and one ultra subdwarf, to test my metallicity estimate techniques (see Section 3.3 for details). I completed the data reduction of the iSHELL spectra using the Spextool for iSHELL package[1]. Spextool (Cushing et al. 2004) has been updated in the newest release to be compatible with iSHELL data, and performs dark subtraction, flat fielding, order tracing and extraction, linearity correction and returns a wavelength solution calibrated using ThAr lamps. I removed telluric absorption features using the `xtellcor` (Vacca et al. 2003) function, which is also part of the larger Spextool reduction package.

3.3 The Metallicity of Subdwarfs

As discussed in Sections 1.6.1 and 2.2.3, precise metallicities of M dwarfs are difficult to determine. In Section 2.4 I discussed a tool I created to estimate metallic-

[1] `http://irtfweb.ifa.hawaii.edu/research/dr_resources/`

Table 3.1. Spectra-type grid of subdwarf targets

Sp. Type Range (1)	Dwarfs (2)	Subdwarfs (3)	Extreme Subdwarfs (4)	Ultra Subdwarfs (5)
K7-8	Gl 143.1	LHS 1703*	LHS 3276*	LHS 1454*
	—	LHS 170	LHS 104	LSR J0621+3652
	—	LHS 173	LHS 522	LSR J2115+3804
M0-0.5	Gl 270*	LHS 12*	LHS 360*	LHS 2843*
	—	LHS 42	LHS 489	LHS 182
	—	LHS 174	LHS 2355	LSR J1956+4428
M1-1.5	Gl 229A*	LHS 2163*	LHS 1994*	LHS 1863*
	Gl 908	LHS 482	LHS 364	LHS 518
	—	LHS 178	LHS 318	LSR J2205+5353
M2-2.5	Gl 411*	LHS 228*	LHS 2326*	LHS 1691*
	Gl 393	LHS 2852	LHS 3555	LSR J0020+5526
	—	LHS 20	LHS 161	WISE J0707+1705
M3-3.5	Gl 436*	LSR J0705+0506*	[LSR J1918+1728*]	[LHS 325*]
	Gl 109	LHS 272	LHS 1174	LSR J0522+3814
	Gl 388	LHS 156	LHS 3263	LHS 3382
M4-4.5	Gl 402*	LHS 2674*/LHS 504*	LSR J1340+1902*	LHS 1032*
	Gl 447	NLTT 3247	LHS 375	LHS 4028
	LHS 3255	LHS 3409	LHS 3090	LHS 453
M5-5.5	Gl 51*	LHS 2061*	LHS 2405*	LHS 2500*
	[LP 467-16]	LHS 3189	LHS 515	LSR J2122+3656
	—	LHS 3390	LHS 2096	LHS 205a
M6-6.5	Gl 406*	[LHS 2746*]	LHS 2023*	LSR J0621+1219*
	Teegarden	LHS 1166	2MASS J0822+1700	LHS 1625
	—	LHS 1074	LHS 1742a	LHS 1826
M7-7.5	—	LHS 377	—	—

Note. — An asterisk indicates a spectral standard. The three spectral standards in braces were not, however, observed: LSR J1918+1728 because it was confused at the observation epoch with a background star, LHS 2746 because it was too faint for the observing conditions, and LHS 325 because of a typographical error in the observing list. LP 467-16 was observed but was later determined to be a binary and I therefore do not list parameters for it. A few of the object names are abbreviated in the table: "Teegarden" is Teegarden's Star; "2MASS J0822+1700" is 2MASS J08223369+1700199, and "WISE J0707+1705" is WISEA J070720.50+170532.7.

ities of M dwarfs and in Section 1.6.1 I mentioned other novel techniques to do this. Unfortunately, these methods are focused on solar-metallicity or near-solar metallicity stars and are not calibrated for the low metallicities present in this sample. Therefore, here I used two different methods: one to determine the metallicity of the dwarf and dwarf/subdwarf stars ([Fe/H] > -0.5 dex), and another to determine the metallicities of the more metal-poor subdwarfs, as well as the extreme and ultra subdwarfs.

For the near solar metallicity stars the majority of the previously-mentioned methods (see Section 1.6.1) use spectral features in the near-infrared, while here my spectra are optical. Mann et al. (2013a) published [Fe/H] relations that utilized optical spectra; however, their relations are highly dependent on the Na doublet at 8200Å, which is contaminated by telluric features in my spectra and therefore it is difficult to measure an equivalent width. Because of this, I used the near-infrared color relation from Newton et al. (2014) to estimate [Fe/H] for all the dwarfs and subdwarfs in the sample. Figure 3.2 shows how the photometric [Fe/H] compares to spectroscopic estimates of [Fe/H] from Gaidos et al. (2014) and Mann et al. (2015) for the 10 overlapping objects. I find a mean scatter of 0.15 dex and I adopt this as the uncertainty in [Fe/H] for the dwarfs and subdwarfs.

Low-metallicity extreme and ultra subdwarfs are often categorized using a ζ parameter, which relates the CaH2 (6814−6846 Å) and CaH3 (6960−6990 Å) band ratios to the TiO5 (7126−7135 Å) band, since the CaH band is primarily sensitive to temperature while the TiO5 band is sensitive to both temperature and metallicity (Dhital et al. 2012). Using high resolution spectra of subdwarfs and extreme subdwarfs, Woolf et al. (2009) determined a relationship between ζ and [Fe/H]. I used this relation and measured a ζ value and hence [Fe/H] for each of the stars in the sample. The relation was recalibrated by Mann et al. (2013c), but I find that the change in

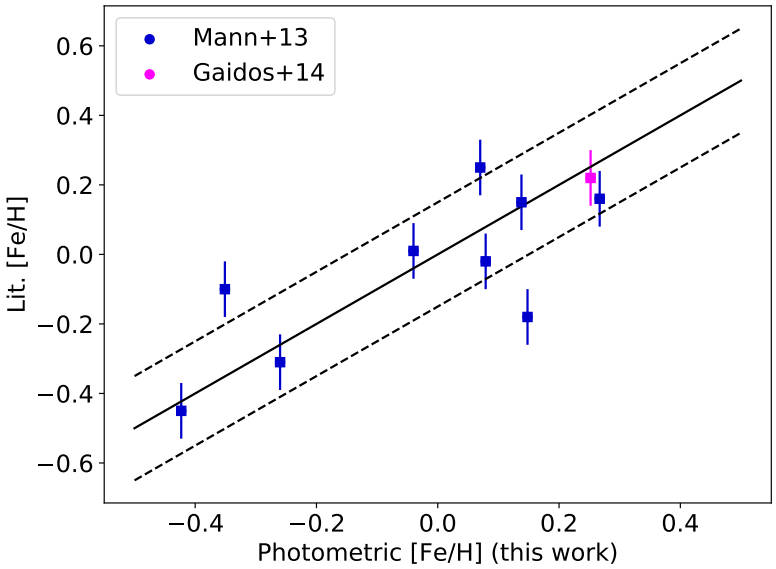

Fig. 3.2: Comparison between my values of [Fe/H] and previously measured literature [Fe/H] values for the 10 overlapping objects. My values of [Fe/H] were determined photometrically using the near-IR color to metallicity relation from Newton et al. (2014). The literature values of [Fe/H] were determined spectroscopically by Gaidos et al. (2014) and Mann et al. (2015), both using the method outlined in Mann et al. (2013a). I find that the photometric metallicities show the same trend as the spectroscopic metallicities and that there is no bias towards over or underestimating the metallicities using photometric relations. The black solid line represents a one-to-one fit, and shows where all the points would lie if my photometrically determined [Fe/H] values matched the literature values exactly. I find a mean scatter around this line of 0.15 dex, and I adopt this value as the uncertainty for all of my [Fe/H] values determined using this method.

the derived value of [Fe/H] is significantly smaller than the quoted uncertainty of the relation (0.3 dex), and so I report the original [Fe/H] values determined with the Woolf et al. (2009) relation.

As an extra check, I used the high-resolution (R∼35,000) near infrared iSHELL spectra of three dwarfs, four subdwarfs, one extreme subdwarf and one ultra subdwarf, to test the metallicities determined with the above methods. Figure 3.3 shows an example of the high resolution spectra and how the sodium doublet changes with

metallicity. I calculated metallicities using the relation presented in Newton et al. (2014) that uses the equivalent width of the sodium doublet at 2.2 μm to determine the metallicity with an uncertainty of 0.12 dex. I find that these metallicities agreed with the metallicities previously reported by Mann et al. (2015) for the three dwarf stars, and that the metallicities I derive from the high resolution spectra are consistent with the metallicities derived using the Woolf et al. (2009) relation. One of the extreme subdwarfs (LHS 173) has a metallicity reported from the APOGEE Stellar Parameters and Chemical Abundances Pipeline (ASPCAP) (Schmidt et al. 2016). My derived metallicity from the ζ parameter and the metallicity from (ASPCAP) are within 0.05 dex, which further validates my derived metallicites.

3.4 Determining Effective Temperatures

To calculate the effective temperature, I fit each spectrum to the BT-SETTL model grid using a method similar to that of Mann et al. (2013b, 2015). The BT-SETTL grid was created using the PHOENIX stellar atmosphere code (Allard et al. 2012). I chose to use the BT-SETTL grid that utilized the Caffau et al. (2011) solar abundances (CIFIST grid[2]) since Mann et al. (2013b) found that this grid of abundances gave the smallest errors in effective temperature when comparing model-fit effective temperature values to precisely known effective temperatures determined through long baseline optical interferometry in combination with the Stefan Boltzmann Law (see Section 1.4.2 and 1.4.3).

The model grid I used contained effective temperatures ranging from 2600 to 4500 K in 100 K bins, metallicities ranging from -2.5 to $+0.5$ dex in 0.5 dex bins, and surface gravities ($\log g$) of 4.5, 5.0, or 5.5 dex [$cm\ s^{-2}$]. This was the smallest-resolution grid publicly available for the CIFIST models.

[2] `https://phoenix.ens-lyon.fr/Grids/BT-Settl/CIFIST2011/`

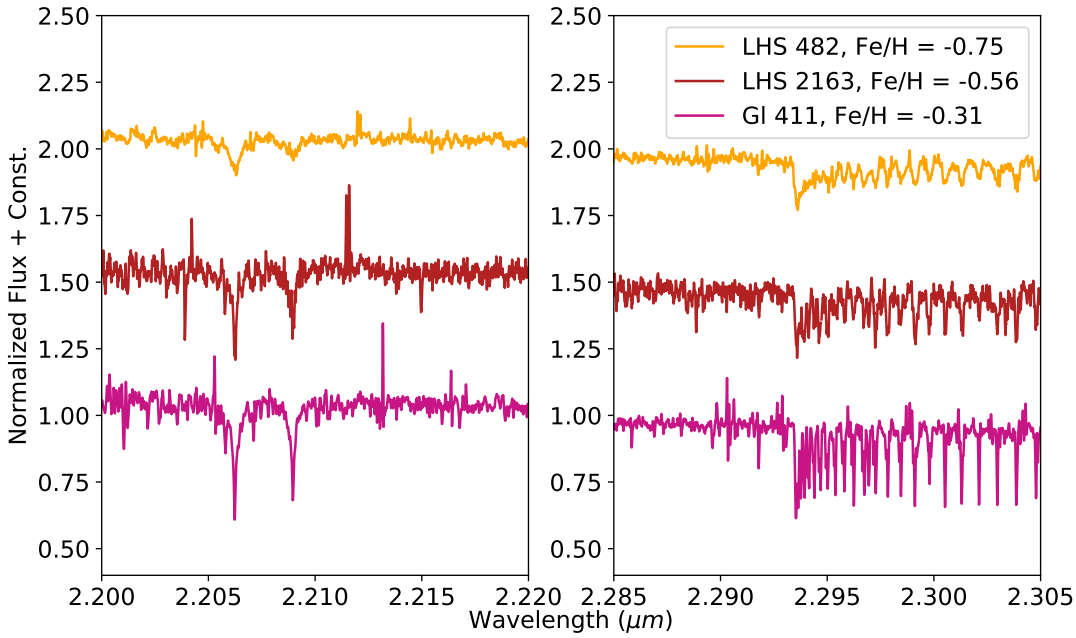

Fig. 3.3: iSHELL K-band spectra of Gl 411, LHS 2163, and LHS 482. The spectra have all been shifted to rest by cross correlation with model templates. The left plot is centered on the sodium doublet (2.2 μm) and the right plot is centered on the CO bandhead (2.3 μm). These plots show the effect of decreased metallicity on these line strengths and how I can use the sodium doublet to estimate the stellar metallicity. I also note that LHS 482 is rotationally broadened, which is intriguing since low metallicity (-0.75 dex) is reminiscent of old age while rapid rotation is reminiscent of youth (West et al. 2015). This is the only star in the iSHELL sample which shows rotational broadening and I merely note it here as a potential future target of interest.

To compare the models to an observed spectrum I convolved the models with a Gaussian kernel. I used the full width at half maximum (FWHM) of the spectrum and converted to the standard deviation ($\sigma \simeq \mathrm{FWHM}/2.355$), which was then used as the standard deviations of the Gaussian kernel. I then determined a goodness-of-fit statistic (G) for each model k, given by the following equation from Cushing et al. (2008):

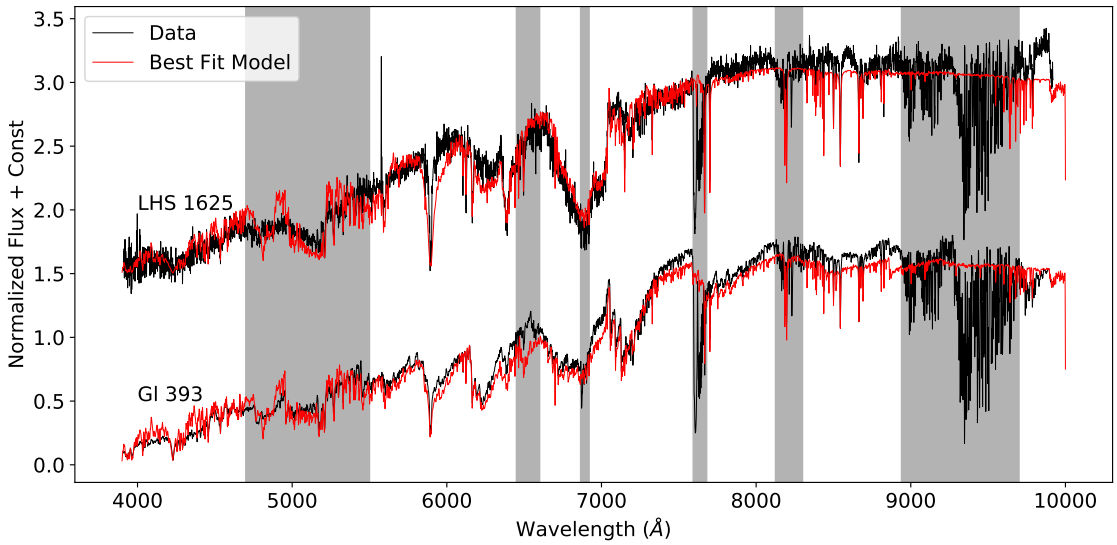

Fig. 3.4: Example of two of my spectra (black) and their respective best-fit model spectra (red). The gray regions are the regions that have weights of zero. The four regions red-ward of 6800 Å are excluded due to telluric features. The region between ∼6400−6600Å is a region where there is a known issue with a poorly modeled TiO absorption band (Reylé et al. 2011). The region around 5000Å does not match the majority of the spectra (regardless of effective temperature or metallicity), and the scaling of the MgH band is particularly problematic. LHS 1625 has a spectral type of usdM6, a best-fit effective temperature of 3400 K, a best-fit $\log(g)$ of 5.5, and a [Fe/H] of −1.5. Gl 393 has a spectral type of dM2, a best-fit effective temperature of 3500 K, a best-fit $\log(g)$ of 5.0, and a [Fe/H] of 0.0.

$$G_k = \sum_{i=1}^{n} \left(\frac{w_i (F_i - C_k \mathcal{F}_{i,k})}{\sigma_i} \right)^2 \tag{3.1}$$

where n is the total number of data pixels, w_i is a weight assigned to each data pixel, F_i is the flux density of each data pixel, $\mathcal{F}_{i,k}$ is the flux density of each model k pixel, σ_i is the uncertainty in each data pixel, and C_k is a normalization constant. For absolute flux calibrated stars, C_k is equal to R^2/D^2; however, since R is unknown, I followed Mann et al. (2013b) and set this constant so that the mean of F and F_k

were the same. The model spectrum chosen as the best fit (and therefore the effective temperature estimate) was the one which minimized the goodness-of-fit statistic (G).

The weights w_i were set to either 0 or 1 so as to exclude regions in the spectra that were contaminated by telluric features, or regions where models did not accurately fit observed spectra of low-mass stars. These regions are shown with gray boxes in Figure 3.4. More details on which regions were excluded and why are given in the caption for Figure 3.4.

To test the accuracy of these effective temperature measurements I compared them to the effective temperatures of stars in my sample that have previous literature values (Figure 3.5). The technique in Mann et al. (2015) has been calibrated against effective temperatures derived using long baseline optical interferometry and shows typical uncertainties of 60 K, but does not contain subdwarf stars. Effective temperature estimates from Rajpurohit et al. (2014, 2016) measure the effective temperatures by fitting mid-to-high resolution optical and near-IR spectra to the same BT-Settl model grid as used here, but only measure effective temperatures for a small subset of M subdwarf stars. My effective temperature estimates are consistent with all three previous literature effective temperature methods and show a mean fractional deviation of less than 1%. I find that 83% of the measurements fall within 1σ of the literature values and all of the measurements fall within 2σ of the literature measurements, leading me to conclude that my estimates are accurate.

I also compared the effective temperatures to those reported by Gaia DR 2 (Andrae et al. 2018). Andrae et al. (2018) use an empirically trained machine learning algorithm to determine a relation between Gaia G-, R-, and B-band photometry and previously determined $T_{\rm eff}$ measurements in the literature. I find that the effective temperatures listed in Gaia DR2 are higher than my effective temperatures by 10% on average, and that the discrepancy is larger for cooler stars (see Figure 3.6). This

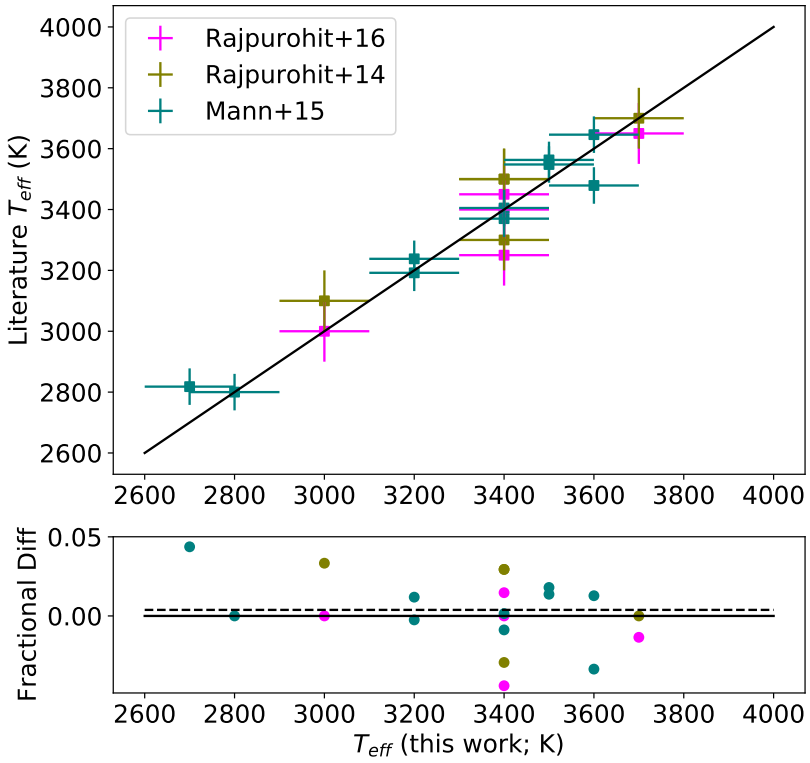

Fig. 3.5: Comparison between my temperatures and those measured by previous studies. If my values and the literature values are exactly the same the fractional difference on the bottom plot would be exactly 0.0 (black solid line). The fractional difference is defined as the literature effective temperature minus my measured effective temperature divided by my effective temperature. I find a mean fractional difference of 0.3% (dotted line). All of my effective temperatures deviate from previous literature values by 100 K or less except for one which deviates by 150 K. The 100 K mismatches seen between my values and those of Rajpurohit et al. (2014) are probably due to the coarse grid size (100 K) of both studies.

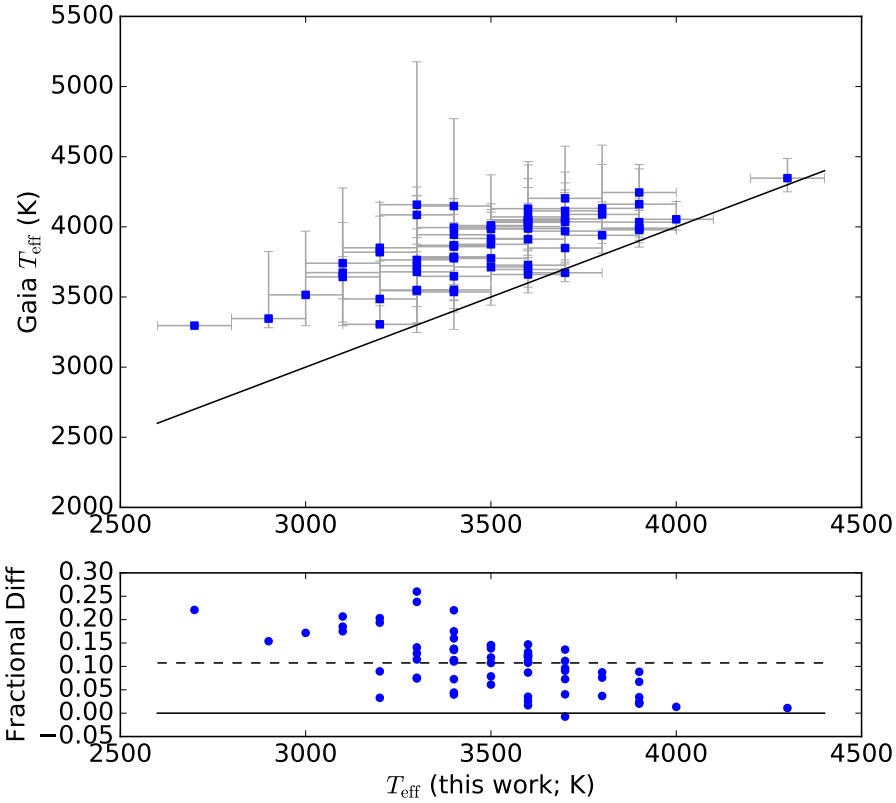

Fig. 3.6: Comparison between the temperatures reported here and those reported in Gaia DR2 (Andrae et al. 2018). Gaia overestimates the temperatures by a mean value of 10%, however the temperatures below $\sim$ 3200 K are overestimated by an even greater amount (almost 20%).

discrepancy is not surprising because the stars in this sample are at the edge of parameter space included in the machine learning training; the vast majority of the stars had near solar metallicities (95% had [Fe/H] > -0.82 dex) and $T_{\rm eff}$ above 4000 K. Because of this, I do not use Gaia DR2 temperatures for any of the remaining analysis.

3.5 Measuring the Bolometric Luminosity

I obtained broad-band photometry for all of the sources in the sample, spanning the blue end of the optical region to mid-IR wavelengths. Optical photometry was obtained from the Sloan Digital Sky Survey's 12^{th} data release (SDSS DR12; Alam et al. 2015), the Pan-STARRS1 survey (Chambers et al. 2016), and from Gaia's Red and Blue Photometers (Gaia Collaboration et al. 2016). All of the near-infrared (NIR) photometry was obtained from the 2MASS All-Sky Point Source Catalog (2MASS PSC; Skrutskie et al. 2006), with one source supplemented from the corresponding Reject Table (this source is noted in Table 3.2). The *Wide-Field Infrared Survey Explorer* (WISE; Wright et al. 2010) AllWISE Point Source Catalog served as the source of mid-IR photometry. Both $WISE$ and 2MASS photometry were downloaded from IRSA[3].

I imposed quality cuts to ensure that the photometry was accurate, and I examined each source by eye to ensure that there was no major background contamination. I only used SDSS photometry that had been flagged as "clean", which selects the primary photometry for each source and rejects sources with any deblending problems, interpolation issues or saturation. The main issue with much of the Pan-STARRS photometry is the relatively high saturation limit, which is conservatively estimated to be 14.5, 15, 15, 14, and 13 for the g, r, i, z, and y filters, respectively. Many fields are quoted to have reliable photometry up to a magnitude brighter than this, but to be conservative I chose to include only photometry brighter than these limits by at most a half magnitude, and only when there was no other indication of poor photometry (e.g., bad quality flags, or PSF did not include the entire source). For both $WISE$ and 2MASS data I did not include any photometry that was flagged as contaminated, saturated, or had a quality flag indicating that the photometry had

[3] `http://irsa.ipac.caltech.edu/frontpage/`

a signal-to-noise ratio (SNR) less than five. I also visually inspected the $WISE$ W3 and W4 bands, and did not include any photometry from these bands when the source was not visually discernible from the background. Since there are no quality flags for the Gaia DR2 data, I followed guidelines from Evans et al. (2018) and eliminated any sources with a color excess exceeding $1.3 + 0.06(G_{\rm BP}$ - $G_{\rm RP})^2$, where $G_{\rm BP}$ is the Gaia blue-band magnitude and $G_{\rm RP}$ is the Gaia red-band magnitude. This relation removes any sources that have been affected by severe crowding, or calibration and processing issues. The final compiled photometry for each target is listed in Table 3.2.

I converted magnitudes to flux densities using the equation

$$F_\nu = F_{\nu 0} \times 10^{-m/2.5} \tag{3.2}$$

where F_ν is the flux density, m is the magnitude, and $F_{\nu 0}$ is the zero magnitude flux density. Gaia, 2MASS and $WISE$ magnitudes are given in the Vega photometric system, and $F_{\nu 0}$ is a constant that gives the same response as Vega for a given frequency (ν). The zero magnitudes for 2MASS and $WISE$ are given in the Explanatory Supplements[4,5], and for Gaia they were calculated using the Gaia B- and R-band filters and a model of Vega by the SVO Filter Profile Services[6]. For $WISE$, I used the zero magnitudes derived using a constant power-law spectrum, as recommended in the documentation since the sources were not steeply rising in the mid-IR. Pan-STARRS photometry is given in the AB magnitude system (Oke & Gunn 1983) and thus has a constant zero magnitude flux for all bands. The SDSS magnitude system was intended to be an AB system, but is known to require slight adjustments (Fukugita et al. 1996), which are given in Holberg & Bergeron (2006). To convert

[4] https://www.ipac.caltech.edu/2mass/releases/allsky/doc/sec6_4a.html
[5] http://wise2.ipac.caltech.edu/docs/release/allsky/expsup/sec4_4h.html
[6] http://svo2.cab.inta-csic.es/svo/theory/fps/index.php?mode=browse

SDSS magnitudes to fluxes, I used the equations provided by the SDSS documentation[7] since the SDSS magnitudes are asinh magnitudes, not pogson magnitudes, and Equation 3.2 therefore cannot be used.

I converted F_ν to F_λ using $F_\lambda = F_\nu(c/\lambda_c^2)$, where c is the speed of light and λ_c if the center of each filter bandpass, and given in Table 3.2. These final values of F_λ are the photometry values shown in Figure 3.7 and are what I used for the remainder of the calculations involving photometry.

Once the photometry was converted to physical flux densities, I used these points to anchor a spectrum. I chose to use the BT-SETTL model spectra throughout, since the flux calibration of the blue end of the spectra has known issues and there are large telluric absorption features contaminating the red side of the spectra. The best-fit BT-SETTL model from my effective temperature estimates (see Section 3.4) was normalized to fit the photometry. The normalization constant was determined by generating synthetic photometry from the model spectrum in a method similar to that of Filippazzo et al. (2015). The synthetic photometry was generated from the best-fit model spectrum using filter transmission curves from the SVO Filter Profile Services and the following equation

$$F_{\lambda,synth} = \frac{\int T(\lambda) F_{\lambda,model}(\lambda) d\lambda}{\int T(\lambda) d\lambda} \tag{3.3}$$

where $T(\lambda)$ is the transmission curve from SVO, interpolated onto the same wavelength grid as the model spectrum ($F_{\lambda,model}$). The normalization constant was then found by minimizing the squared difference between the synthetic and catalog photometry. The optimal minimization (and hence value of the normalization constant) was determined using the scipy routine, `scipy.optimize.minimize_scalar`.

[7] `http://www.sdss.org/dr12/algorithms/magnitudes/`

Table 3.2. Photometry for all subdwarf targets

Star	SDSS u 0.35 μm	σ_u	SDSS g 0.48 μm	σ_g	Pan-STARRS g 0.481 μm	$\sigma_{PS1\ g}$	Gaia $G_{\rm BP}$ 0.5044 μm	$\sigma_{G_{\rm BP}}$	Pan-STARRS r 0.617 μm	$\sigma_{PS1\ r}$	...*
LHS1032	22.5	0.3	19.03	0.03	18.71	0.02	18.15	0.018	17.211	0.003	
LHS104	17.06	0.01	14.48	0.02	–	–	13.969	0.001	–	–	
LHS1074	24.1	1.1	20.18	0.02	19.84	0.02	19.25	0.06	18.374	0.004	
LHS1166	22.4	0.3	19.99	0.02	19.64	0.01	19.22	0.06	18.247	0.003	
LHS1174	21.1	0.1	18.03	0.02	17.81	0.006	17.28	0.01	16.378	0.004	
LHS12	15.75	0.01	13.1950	0.0005	–	–	12.492	0.002	–	–	
LHS1454	–	–	–	–	17.17	0.005	16.788	0.007	15.931	0.002	
LHS156	–	–	–	–	15.651	0.001	15.205	0.003	–	–	
LHS161	18.39	0.02	15.55	0.02	15.368	0.001	14.926	0.004	–	–	
LHS1625	–	–	–	–	20.13	0.03	19.48	0.02	18.52	0.01	
LHS1691	–	–	–	–	18.352	0.003	17.803	0.009	16.874	0.004	
LHS170	–	–	–	–	–	–	10.891	0.001	–	–	
LHS1703	17.82	0.03	15.18	0.04	14.846	3.0E-04	14.496	0.0020	–	–	

Note. — *See online version of Kesseli et al. (2019) or email the author for full table, which includes all 88 objects and all photometry

The bolometric luminosity was determined from

$$L_{\rm bol} = 4\pi D^2 \int_{0.1\ \mu m}^{500\ \mu m} C \times F_\lambda d\lambda \tag{3.4}$$

where C is the normalization constant determined above, F_λ is the model flux, and D is the distance determined from Gaia DR2 parallaxes (Gaia Collaboration et al. 2018). Instead of using the inverted parallax to obtain D, I used the distances reported by Bailer-Jones et al. (2018) for Gaia DR2, which are publicly available within the Gaia archive external catalog, `external.gaiadr2_geometric_distance`. The Bailer-Jones et al. (2018) distances are more reliable because they account for the nonlinearity of the transformation from parallax to distance. This nonlinearity is corrected using a Bayesian distance prior that varies as a function of galactic longitude and latitude. Finally, I used a simple trapezoidal integration (`numpy.trapz`) to numerically integrate F_λ over the stated wavelength range.

To determine how the model parameters ($T_{\rm eff}$, [Fe/H], and log g) influenced the bolometric luminosity calculation, I investigated the ways in which varying these parameters altered my estimates of $L_{\rm bol}$. I found that by changing the model by one grid point, $\log_{10}(L_{\rm bol}/L_{\rm Sun})$ changed by an average of 0.008 ± 0.005, 0.007 ± 0.005, and 0.002 ± 0.002 for a change in $T_{\rm eff}$ of 100K, and [Fe/H] and log g of 0.5 dex, respectively. If all three are changed in conjunction, the change in $\log_{10}(L_{\rm bol}/L_{\rm Sun})$ was on average 0.015 ± 0.008; however, I do not expect the estimates to deviate this substantially in all three parameters. These errors are larger than the propagated uncertainties, and so I adopt the change of all three parameters in conjunction as a conservative estimate of the uncertainty in the bolometric flux (the uncertainty in the parallax is then incorporated to determine the total uncertainty in $L_{\rm bol}$).

I also compared the ways in which the use of real spectra versus models altered the values of $L_{\rm bol}$. Three of my targets had previously published spectra that

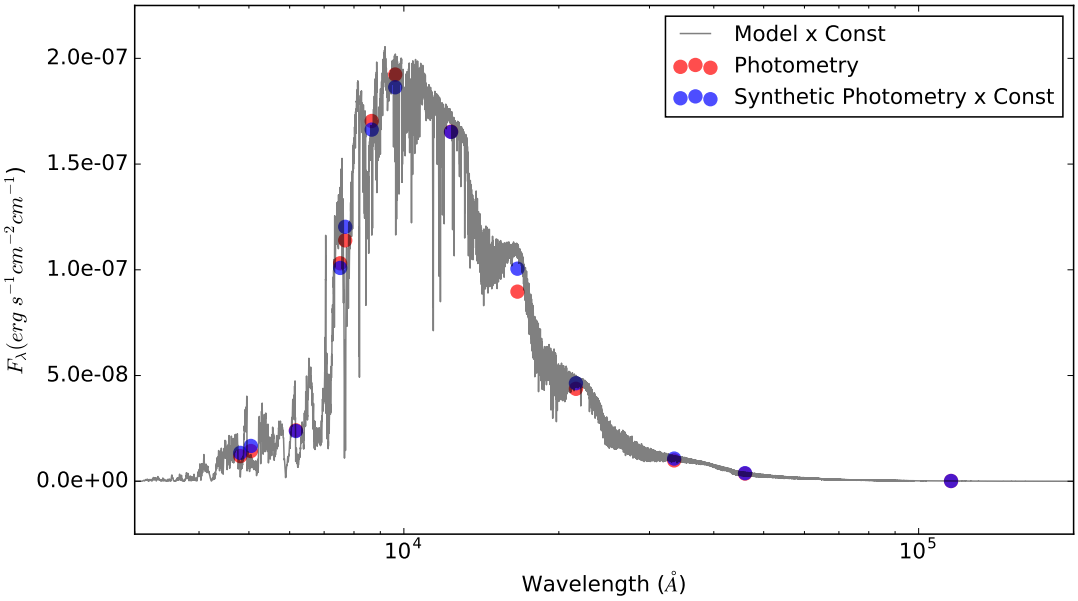

Fig. 3.7: Spectral energy distribution (SED) of LHS 377. The red points show all the available photometry for the source, converted into F_λ. The errorbars from the photometry are plotted but are similar than the points. The blue points are the synthetic photometry created using the filter bandpasses and gray model spectrum. The synthetic photometry and the model are both multiplied by the normalization constant C. To determine the bolometric flux and in turn the bolometric luminosity, I integrate under the gray model multiplied by C.

spanned the near- and mid-IR (LHS 1174, LHS 377, LSR J2122+36, all from the SpeX Prism Spectral Libraries (Burgasser 2014)[8]). In combination with the optical spectra reported here, a majority of the flux-contributing region of the SED was covered by real spectra. I found that by using the real spectra instead of the best-fit model, $log_{10}(L_{bol}/L_{Sun})$ changed by 0.01. This value is well within the uncertainties I adopted based on changing the model, so I conclude that using a model instead of a real spectrum is indeed valid (as long as the above uncertainties are included).

[8] `http://pono.ucsd.edu/~adam/browndwarfs/spexprism/`

3.6 Results and Updated Radius Relations

The effective temperatures (calculated in Section 3.4) and bolometric luminosities (calculated in Section 3.5) were combined to determine a radius using the Stefan-Boltzmann Law: $R = \sqrt{L_{\rm bol}/(4\pi\sigma T_{\rm eff}^4)}$. The derived parameters (including $T_{\rm eff}$, $L_{\rm bol}$, and R) for all of the sources are given in Table 3.3. Figure 3.8 shows how the radii change with decreasing metallicity for a given effective temperature. I find that stellar evolutionary models from Baraffe et al. (1997) accurately predict the radii of low-metallicity subdwarfs. For a given effective temperature, the radius can deviate by a factor of almost five for a change in metallicity of 2.5 dex.

3.6.1 Color Relations

Broadband colors are readily available for a massive number of sources thanks to surveys such as Gaia and 2MASS. I therefore present Gaia and 2MASS color-to-radius and absolute magnitude-to-radius relations for my sources. Figure 3.9 shows different optical and IR color-to-radius relations. I find that $J-K$ is not well fitted by a simple equation, but both Gaia $R-J$ and Gaia $R-B$ can be fitted with equations relating these colors to the stellar radius. I chose a decreasing exponential equation to describe the data, which was physically motivated by the fact that the stellar radii cannot collapse to sizes smaller than $0.1 R_{\rm Sun}$ due to degeneracy pressure. The following exponential describes the data:

$$R = A\ e^{-[b(color)+c[Fe/H]]} \tag{3.5}$$

where the best fit constants for Gaia $R-J$ are 5.02, 2.04, and -1.06 and for Gaia $B-R$ are 4.0, 1.17, and -1.04 for A, b, and c, respectively. Even with a metallicity dependent relation I still find a scatter in the radius of $\sim 20\%$.

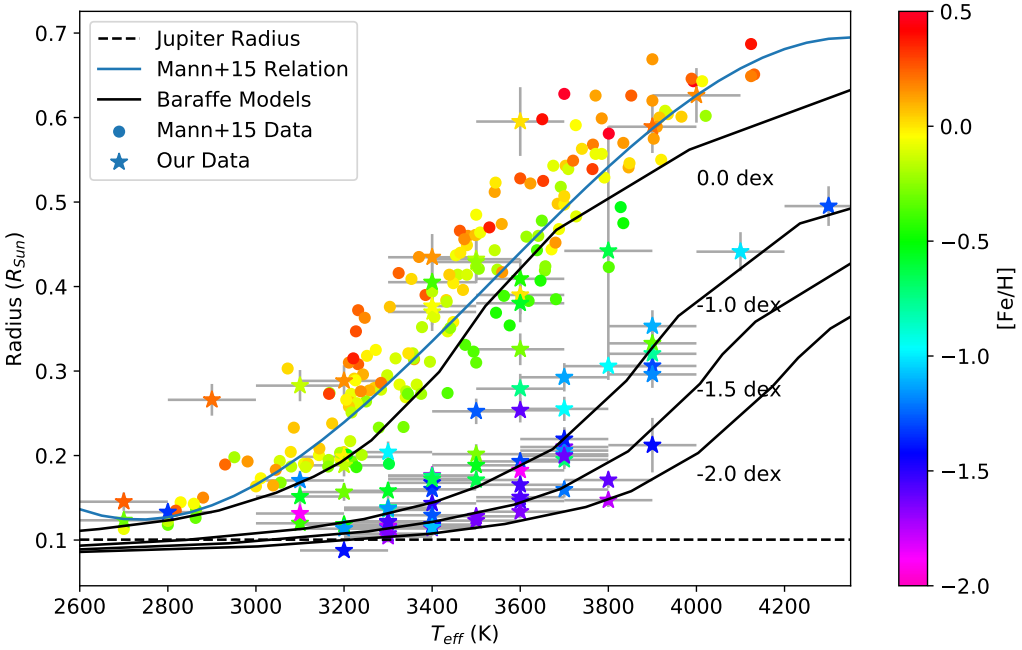

Fig. 3.8: Results of the effective temperature and radius determinations of all the stars in my sample (star markers), as well as previously determined effective temperatures and radii from Mann et al. (2015) (circle markers). The points are colored by their metallicity ([Fe/H]). The empirically determined relation from Mann et al. (2015) for solar metallicity stars is shown as a blue line, while the relations from the Baraffe stellar evolutionary models (Baraffe et al. 1997) are shown in black. The subdwarfs fall along the stellar evolution curves and thus validate the predicted factor of four or more change in radius for extreme and ultra subdwarfs for a given effective temperature.

Table 3.3: Derived subdwarf parameters

Star Name	Spectral Class	$T_{\rm eff}$ (K)	σ_T (K)	$log(L_{\rm bol}/L_{\rm Sun})$	$\sigma_{\log(L_{bol}/L_{\rm Sun})}$	Radius ($R_{\rm Sun}$)	σ_R ($R_{\rm Sun}$)	[Fe/H]	$\sigma_{[Fe/H]}$	[Fe/H] method
2MASSJ0822+1700	usdM6	3200	100	−3.139	0.031	0.088	0.006	−1.4	0.3	Spec
Gl109	dM3	3400	100	−1.783	0.058	0.37	0.033	−0.1	0.08	Lit[1]
Gl143.1	dK7	4000	100	−1.044	0.011	0.626	0.033	0.17	0.15	Phot
Gl229A	dM1	3600.0	100	−1.271	0.035	0.595	0.041	0.02	0.08	Lit[1]
Gl270	dM0	3900	100	−1.141	0.011	0.589	0.03	0.23	0.15	Phot
Gl388	dM3	3400	100	−1.643	0.02	0.435	0.027	0.15	0.08	Lit[1]
Gl393	dM2	3500	100	−1.597	0.01	0.432	0.025	−0.18	0.08	Lit[1]
Gl402	dM4	3200	100	−2.105	0.013	0.288	0.019	0.16	0.08	Lit[1]
Gl406	dM6	2700	100	−2.995	0.007	0.145	0.011	0.25	0.08	Lit[1]
Gl411	dM2	3400	100	−1.704	0.037	0.405	0.029	−0.38	0.08	Lit[1]
Gl436	dM3	3600	100	−1.638	0.015	0.39	0.023	0.01	0.08	Lit[1]
Gl447	dM4	3200	100	−2.43	0.014	0.198	0.013	−0.02	0.08	Lit[1]
Gl51	dM5	2900	100	−2.346	0.013	0.266	0.019	0.22	0.08	Lit[2]
Gl908	dM1	3600	100	−1.596	0.011	0.409	0.023	−0.45	0.08	Lit[1]
LHS1032	usdM4	3400	100	−2.775	0.02	0.118	0.007	−1.4	0.3	Spec
LHS104	esdK7	3900	100	−1.711	0.006	0.306	0.016	−1.29	0.3	Spec
LHS1074	sdM6	3200	100	−2.88	0.028	0.118	0.008	−0.52	0.3	Spec

Continued

[1]Mann et al. (2015)
[2]Gaidos et al. (2014)

Star Name	Spectral Class	$T_{\rm eff}$ (K)	σ_T (K)	$\log(L_{\rm bol}/L_{\rm Sun})$	$\sigma_{\log(L_{\rm bol}/L_{\rm Sun})}$	Radius ($R_{\rm Sun}$)	σ_R ($R_{\rm Sun}$)	[Fe/H]	$\sigma_{[Fe/H]}$	[Fe/H] method
LHS1166	sdM6	3100	100	−2.924	0.024	0.12	0.008	−0.39	0.3	Spec
LHS1174	esdM3	3400	100	−2.513	0.013	0.16	0.01	−1.31	0.3	Spec
LHS12	d/sdM0	3900	100	−1.642	0.019	0.331	0.018	−0.33	0.15	Phot
LHS1454	usdK7	3800	100	−2.262	0.012	0.171	0.009	−1.59	0.3	Spec
LHS156	sdM3	3500	100	−2.403	0.009	0.171	0.01	−0.64	0.3	Spec
LHS161	esdM2	3700	100	−2.166	0.006	0.201	0.011	−1.1	0.3	Spec
LHS1625	usdM6	3400	100	−2.809	0.041	0.114	0.009	−1.64	0.3	Spec
LHS1691	usdM2	3400	100	−2.429	0.014	0.176	0.011	−1.8	0.3	Spec
LHS170	esdK7	4300	100	−1.123	0.008	0.495	0.023	−1.28	0.3	Spec
LHS1703	esdK7	3900	100	−1.587	0.012	0.352	0.019	−1.1	0.3	Spec
LHS173	esdK7	4100	100	−1.305	0.016	0.441	0.023	−0.94	0.18	Lit[2]
LHS174	sdM0	3800	100	−1.434	0.32	0.442	0.165	−0.63	0.3	Spec
LHS1742a	esdM6	3300	100	−2.912	0.333	0.107	0.042	−0.97	0.3	Spec
LHS178	d/sdM1	3600	100	−1.795	0.013	0.326	0.019	−0.29	0.3	Spec
LHS182	usdM0	3700	100	−2.128	0.085	0.21	0.024	−1.66	0.3	Spec
LHS1826	usdM6	3300	100	−2.94	0.019	0.104	0.007	−1.73	0.3	Spec
LHS1863	usdM1	3600	100	−2.015	0.01	0.253	0.014	−1.59	0.3	Spec
LHS1994	esdM1	3700	100	−1.844	0.017	0.291	0.017	−1.13	0.3	Spec
LHS20	d/sdM2	3500	100	−2.26	0.011	0.202	0.012	−0.28	0.15	Spec

Continued

[2]Schmidt et al. (2016)

Star Name	Spectral Class	$T_{\rm eff}$ (K)	σ_T (K)	$\log(L_{\rm bol}/L_{\rm Sun})$	$\sigma_{\log(L_{\rm bol}/L_{\rm Sun})}$	Radius ($R_{\rm Sun}$)	σ_R ($R_{\rm Sun}$)	[Fe/H]	$\sigma_{[Fe/H]}$	[Fe/H] method
LHS2023	esdM6	3200	100	−2.917	0.022	0.113	0.008	−1.15	0.3	Spec
LHS205a	usdM5	3400	100	−2.783	0.028	0.117	0.008	−1.43	0.3	Spec
LHS2061	sdM5	3300	100	−2.691	0.019	0.138	0.009	−0.76	0.3	Spec
LHS2096	esdM5	3300	100	−2.852	0.018	0.115	0.007	−1.25	0.3	Spec
LHS2163	sdM1	3600	100	−1.661	0.017	0.38	0.022	−0.56	0.12	iSHELL Spec
LHS228	sdM2	3500	100	−2.32	0.019	0.188	0.012	−0.55	0.3	Spec
LHS2326	esdM2	3300	100	−2.353	0.009	0.204	0.013	−0.98	0.3	Spec
LHS2355	usdM0	3800	100	−2.393	0.014	0.147	0.008	−1.76	0.3	Spec
LHS2405	d/sdM4	3500	100	−1.604	0.011	0.429	0.025	−0.24	0.15	Spec
LHS2500	usdM5	3100	100	−2.845	0.039	0.131	0.01	−1.88	0.3	Spec
LHS2674	sdM4	3300	100	−2.573	0.022	0.158	0.01	−0.57	0.3	Spec
LHS272	sdM3	3400	100	−2.431	0.01	0.175	0.011	−0.72	0.3	Spec
LHS2843	esdM0	3500	100	−2.068	0.015	0.251	0.015	−1.26	0.3	Spec
LHS2852	sdM2	3400	100	−1.767	0.01	0.377	0.023	−0.05	0.12	iSHELL Spec
LHS3090	usdM4	3400	100	−2.609	0.015	0.143	0.009	−1.5	0.3	Spec
LHS318	esdM1	3600	100	−2.25	0.01	0.193	0.011	−1.3	0.3	Spec
LHS3189	d/sdM1	3100	100	−2.72	0.022	0.151	0.01	−0.57	0.15	Phot
LHS3255	dM4	3100	100	−2.177	0.009	0.283	0.018	−0.15	0.15	Phot
LHS326	esdM3	3700	100	−2.147	0.007	0.206	0.011	−1.18	0.3	Spec
LHS3263	esdM3	3700	100	−2.369	0.019	0.159	0.009	−1.22	0.3	Spec
LHS3276	esdK7	3900	100	−1.741	0.014	0.295	0.016	−1.18	0.3	Spec

Continued

Star Name	Spectral Class	$T_{\rm eff}$ (K)	σ_T (K)	$\log(L_{\rm bol}/L_{\rm Sun})$	$\sigma_{\log(L_{\rm bol}/L_{\rm Sun})}$	Radius ($R_{\rm Sun}$)	σ_R ($R_{\rm Sun}$)	[Fe/H]	$\sigma_{[Fe/H]}$	[Fe/H] method
LHS3382	usdM3	3400	100	−2.472	0.013	0.167	0.01	−1.38	0.3	Spec
LHS3390	sdM5	3300	100	−2.708	0.014	0.135	0.008	−0.83	0.3	Spec
LHS3409	d/sdM4	3200	100	−2.635	0.019	0.157	0.01	−0.31	0.12	iSHELL Spec
LHS3555	usdM2	3300	100	−2.842	0.022	0.116	0.008	−1.78	0.3	Spec
LHS360	esdM0	3700	100	−1.96	0.013	0.255	0.014	−0.96	0.3	Spec
LHS364	usdM1	3600	100	−2.491	0.014	0.146	0.008	−1.54	0.3	Spec
LHS375	esdM4	3400	100	−2.697	0.01	0.129	0.008	−1.27	0.3	Spec
LHS377	sdM7	3000	100	−2.993	0.019	0.118	0.008	−0.41	0.3	Spec
LHS4028	usdM4	3500	100	−2.692	0.018	0.123	0.007	−1.64	0.3	Spec
LHS42	esdM0	3800	100	−1.756	0.008	0.306	0.016	−0.96	0.12	iSHELL Spec
LHS453	usdM4	3300	100	−2.799	0.026	0.122	0.008	−1.77	0.3	Spec
LHS482	sdM1	3600	100	−1.929	0.026	0.279	0.018	−0.75	0.12	iSHELL Spec
LHS489	usdM0	3600	100	−2.299	0.017	0.182	0.011	−1.88	0.3	Spec
LHS504	d/sdM5	3100	100	−2.588	0.026	0.176	0.012	−0.18	0.3	Spec
LHS515	esdM5	3400	100	−2.8	0.014	0.115	0.007	−1.08	0.3	Spec
LHS518	sdK7	3900	100	−1.671	0.018	0.32	0.018	−0.79	0.3	Spec
LHS522	usdK7	3900	100	−2.027	0.127	0.212	0.033	−1.41	0.3	Spec
LSRJ0020+5526	sdM2	3700	100	−2.194	0.015	0.195	0.011	−0.7	0.3	Spec
LSRJ0522+3814	usdM3	3500	100	−2.655	0.01	0.128	0.007	−1.63	0.3	Spec
LSRJ0621+1219	usdM6	3300	100	−2.912	0.014	0.107	0.007	−1.65	0.3	Spec
LSRJ0621+3652	usdK7	3700	100	−2.091	0.008	0.219	0.012	−1.38	0.3	Spec

Continued

Star Name	Spectral Class	$T_{\rm eff}$ (K)	σ_T (K)	$\log(L_{\rm bol}/L_{\rm Sun})$	$\sigma_{\log(L_{\rm bol}/L_{\rm Sun})}$	Radius ($R_{\rm Sun}$)	σ_R ($R_{\rm Sun}$)	[Fe/H]	$\sigma_{[Fe/H]}$	[Fe/H] method
LSRJ0705+0506	sdM4	3400	100	−2.451	0.013	0.171	0.01	−0.64	0.15	Phot
LSRJ1340+1902	esdM4	3300	100	−2.698	0.016	0.137	0.009	−1.15	0.3	Spec
LSRJ1956+4428	usdM0	3600	100	−2.465	0.008	0.15	0.008	−1.56	0.3	Spec
LSRJ2115+3804	usdK7	3700	100	−2.174	0.007	0.199	0.011	−1.62	0.3	Spec
LSRJ2122+3656	esdM5	3300	100	−2.802	0.011	0.122	0.008	−1.34	0.3	Spec
LSRJ2205+5353	usdM1	3600	100	−2.384	0.009	0.165	0.009	−1.55	0.3	Spec
NLTT3247	dM4	3200	100	−2.475	0.026	0.188	0.013	−0.09	0.15	Phot
Teegarden	dM6	2700	100	−3.137	0.001	0.123	0.009	−0.31	0.08	Lit[1]
WISE0238+3617	usdM3	3300	100	−2.807	0.015	0.121	0.008	−1.56	0.3	Spec
WISE0707+1705	usdM2	3600	100	−2.57	0.012	0.133	0.008	−1.65	0.3	Spec

I also fit color to metallicity relations for my sample. Like previous studies (e.g., Mann et al. 2013a; Newton et al. 2014; Mann et al. 2015) I find that $J-K_s$ gives the best fit for a single color to [Fe/H] relation, and find the following best-fit equation:

$$[Fe/H] = 4.22(J - K_s) - 3.86 \tag{3.6}$$

where the 1-σ scatter is 0.37 dex.

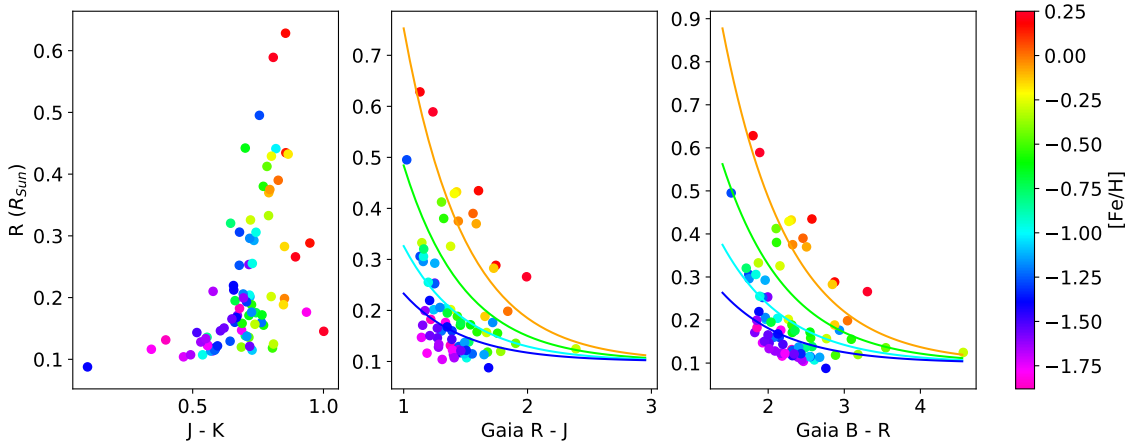

Fig. 3.9: 2MASS and Gaia broadband colors versus stellar radius. Stars with similar colors show large variations in radius for different metallicities. Overplotted on the two plots on the right are my new color−Radius relations for metallicity values of 0.0 (orange), −0.5 (green), −1.0 (cyan), and −1.5 (blue). Even with these metallicity dependent relations I find a 1−σ scatter of $\sim$ 20% in the radius. The fits are given in Equation 3.5.

3.6.2 Absolute Magnitude Relations

Previous studies have found that the scatter in radius relations due to metallicity can be reduced (or even eliminated) by using absolute infrared photometry versus radius relations (M_{K_s}− Radius: e.g., Boyajian et al. 2012; Mann et al. 2015). However, the spread in metallicity explored in previous studies was only about 1.0 dex (from +0.5 to −0.5 dex). Here, I calculate absolute K-band magnitudes for the

complete sample and I find that, while there is significantly less scatter for radii determined using an $M_{K_s}-$ Radius relation, the relation is still metallicity dependent (see Figure 3.10). For the lowest metallicity stars ($[Fe/H] < -1.0$ dex), I measure radii that are on average 10% smaller than the radii that would be determined using the M_K- Radius relation that does not include metallicity as a parameter (Equation 4: Mann et al. 2015). Equation 5 of Mann et al. (2015) gives a relation that includes metallicity as a parameter:

$$R = (a + bM_{K_s} + cM_{K_s}^2) \times (1 + f[Fe/H]), \tag{3.7}$$

where they find best fit values of 1.9305, -0.3466, 0.01647, and 0.04458 for a, b, c, and f, respectively. I find that this relation fits the data better, but still overestimates the radii of the low-metallicity (< 0.5 dex) stars by an average of 5%. I use the data reported here to determine new coefficients that are valid for [Fe/H] values down to -2.0 dex, and find values of 1.875 ± 0.05, -0.337 ± 0.01, 0.0161 ± 0.0009, and 0.079 ± 0.01 for a, b, c, and f, respectively. The scatter in the residuals of the $M_{K_s}-$ Radius relation is 6% and is valid for M_{K_s} values of 4 to 11 and metallicities from $+0.5$ dex to -2.0 dex.

The absolute K_s-band relation greatly reduces the uncertainty in the radius compared to the color$-$radius relation (Equation 3.5) and so I recommend using it to obtain more accurate radii whenever possible.

3.7 Discussion

3.7.1 Internal Consistency Check

I performed a self-consistency check on the radius determinations by comparing the apparent flux levels in each spectrum to the flux of the best fitting model, scaled by the dilution factor R^2/D^2, to determine the apparent flux from the model at

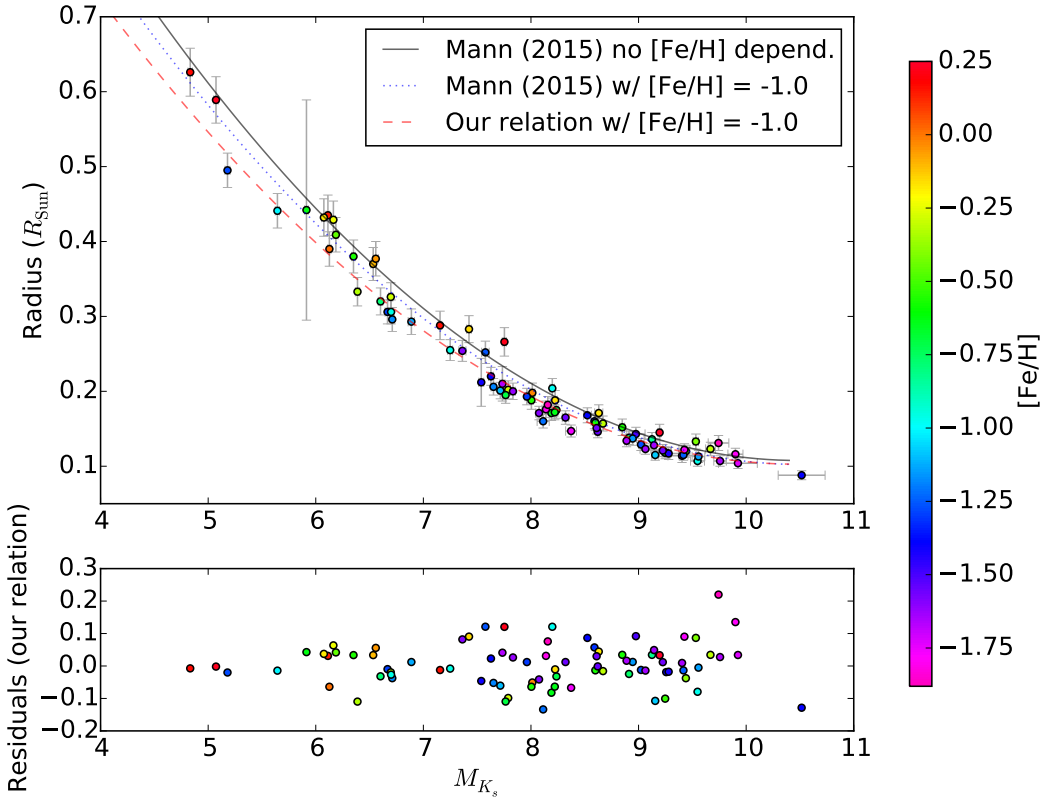

Fig. 3.10: Absolute K_s-band versus radius relation for the entire sample of stars. In black is the best fit relation from Mann et al. (2015), which is valid for stars with $[Fe/H] > -0.6$ and does not include metallicity as a parameter. In blue, I plot the metallicity dependent relation, which has the form of Equation 3.7, extrapolated past its tested metallicity limit (-0.6 dex) at a value of -1.0 dex. I find that while this better fits the data, it still over-predicts the radii of the lowest metallicity stars in the sample. In red, I plot the new metallicity dependent relation at a value of -1.0 dex. The bottom panel shows the residuals between my data and the our new relation. While there is still some intrinsic scatter, it is no longer correlated with metallicity.

Earth. Plotted in Figure 3.11 is an example of this consistency check. Any target for which the observed flux calibrated (black) spectrum fell outside of the $R^2/D^2 \pm \sigma_{R^2/D^2}$ scaled model (transparent blue) was noted as being inconsistent.

I find that 9 out of the 88 spectra fall outside of the $1-\sigma$ errorbars: Gl 436, Gl 447, Gl 51, LHS 170, LHS 375, LHS 2843, LHS 2852, LHS 3189, LHS 3255, LHS 3555. These 9 targets are some of the most extreme outliers in Figure 3.8, which suggests that the true scatter in the $T_{\rm eff}-$Radius relation is actually smaller than what is shown in Figure 3.8. The majority of this discrepancy most likely is due to the uncertainty in $T_{\rm eff}$, and for the one source with previously determined parameters (Gl 436) this is the case; my $T_{\rm eff}$ estimate differs by $\sim$150 K from what Mann et al. (2015) report and thus my radius estimate differs by 0.06 $R_{\rm Sun}$. I hypothesize that the radius discrepancy in a few of the sources is due to inaccurate metallicities, which leads to poor fits to the models. LHS 170 is the hottest star in my sample, and for that reason its metallicity estimate may not be accurate since the methods used for determining metallicity for my sample are only valid for spectral types later than $\sim$K7. LHS 2852 has differing spectroscopic and photometric metallicities even though it is in a part of parameter space where both methods should be valid, leading me to conclude that there is potentially something unusual about its metallicity.

Because almost 90% of the sources pass my internal consistency check, I am confident that the overall trends observed in the data are accurate. I conclude that the 1σ errorbars are not underestimated, and if anything they are overestimated.

3.7.2 Variations in Chemical Abundances

Many of the spectra have unusual spectral features that are not reproduced by the stellar atmosphere models, or have colors and spectroscopic metallicities that are at odds. Figure 3.12 shows these spectra with the features in question labeled. 2MASS J0822+1700 contains prominent Rb I lines (first noted in Lépine

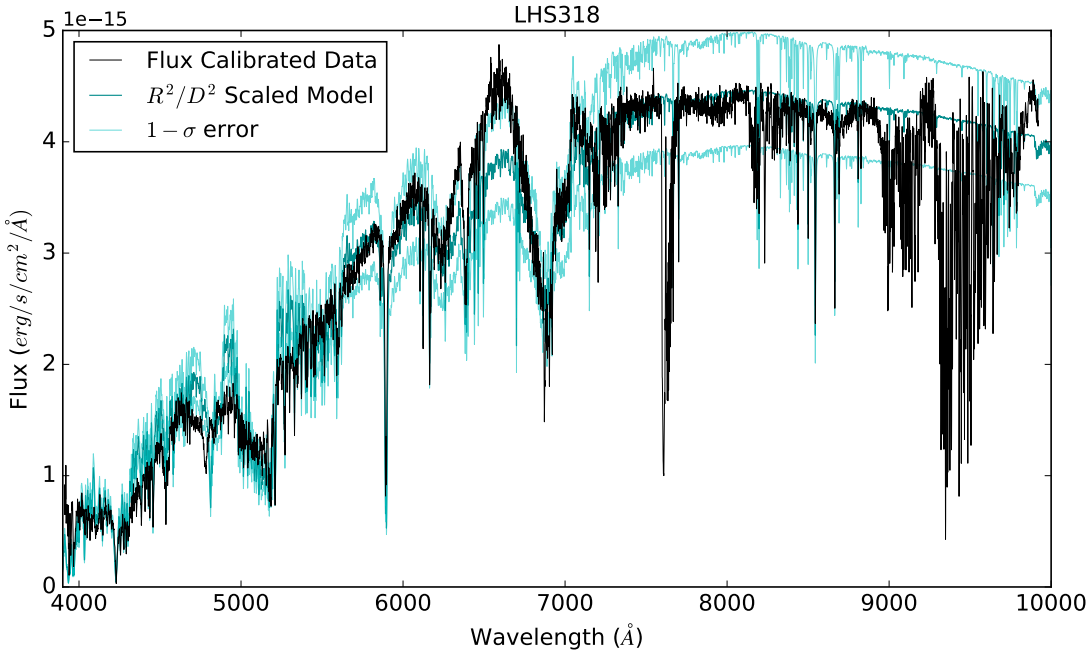

Fig. 3.11: An example of the internal consistency check. The flux calibrated observed spectrum is plotted in black, while the R^2/D^2 scaled model is plotted in teal. The two more transparent teal spectra show the model spectrum scaled using the 1σ uncertainties on the radius. Note the large mismatch between the scaled model and the data around 7500 and between 9000 and 10000 Å is due to telluric contamination in the spectra.

et al. (2004)), which are not seen in any other spectra in this sample or in the models. Rb is a slow neutron capture (s-process) element formed during the AGB phase of stellar evolution, so these interesting objects could have formed near an AGB star and hence be polluted by an overabundance of Rb compared to [Fe/H]. This effect has been seen in warmer halo stars that exhibit enhancements in s-process elements (Beers & Christlieb 2005).

WISE 0238+3617 has a significantly broader Na doublet (labeled Na 'D' in Figure 3.12) than any of the other spectra, as well as a deeper Na I doublet ($\sim$ 8200 Å), deeper K I lines, and weaker Ca II lines. Kirkpatrick et al. (2016), who first

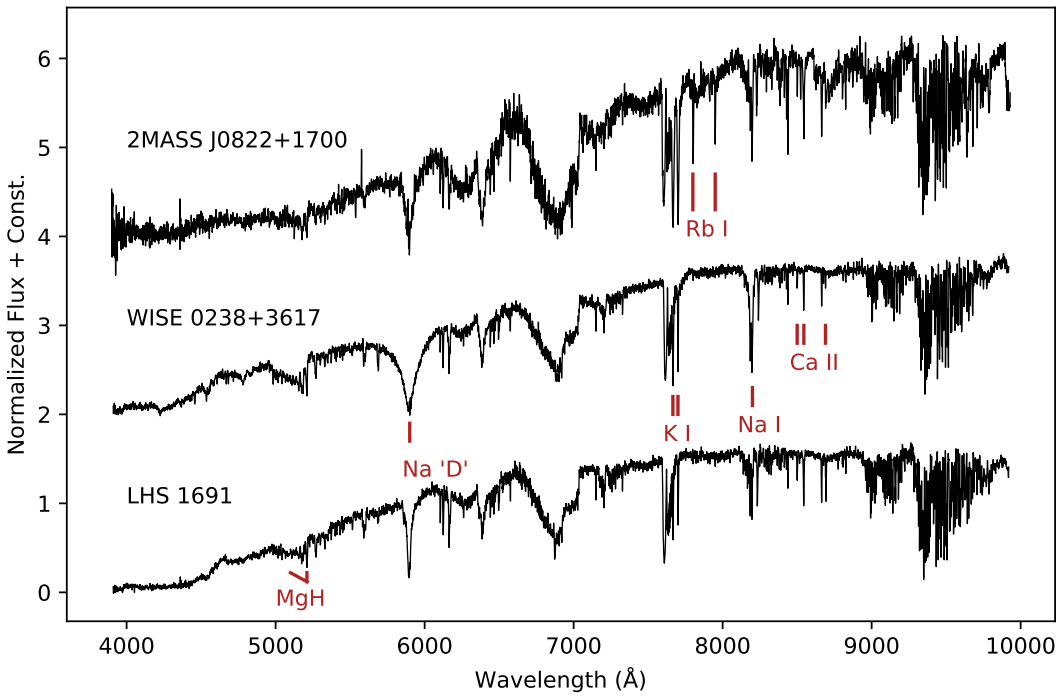

Fig. 3.12: Figure showing three of the spectra that have peculiar features. 2MASS J0822+1700 has Rb I lines that are not seen in any other spectra. WISE 0238+3617 has an extremely broad Na 'D' doublet, slightly stronger Na I and K I, as well as weaker Ca II lines. LHS 1691 has a particularly weak MgH band and the bluest end of the spectrum is noticeably smoother than spectra of similar spectral type.

published its spectrum, theorized that the broad Na doublet was indicative of an extremely low metallicity (< -2.0 dex). The extremely broad Na doublet could be indicative of an over-enhancement of Na. Na is produced during C burning in SN II, so this star could have environmental enhancement, but more information is needed to verify this claim.

LHS 1691 has weak absorption from the MgH band compared to other spectra of similar spectral type. Evidence for two populations of metal poor stars with different Mg abundances (low- and high-Mg groups) has been seen by many groups

in the halo population (e.g., Hayes et al. 2018). The weak MgH absorption in LHS 1691 suggests that this star is potentially part of a low-Mg population. There are other stars in my sample with varying strengths in MgH for similar spectral types, which could be indicative of the spread in the [Mg/Fe] versus [Fe/H] measured by Hayes et al. (2018) (see Figure 3 in Hayes et al. 2018). Since Mg is an α element, publicly available models with varying α abundances for single [Fe/H] values would be useful to better model subdwarfs and estimate α abundances for different stars.

Some of the spectra also have spectroscopic features that are reminiscent of subdwarfs (little TiO absorption), but near-IR colors that would point towards a dwarf star metallicity when the relation from Newton et al. (2014) is applied. LHS 1691 is the most extreme of these cases, where spectroscopically it is classified as an ultra subdwarf (-1.8 dex), but the photometric metallicity relation estimates a metallicity of $+0.3$ dex. Other stars that exhibit this behavior but are not as extreme are: WISE 0238+3617, LHS 2843, LHS 3382, and LHS 104. It is unclear what causes this interesting effect and I merely note it here. I expect to explore theis further at a later time.

All of the above-mentioned unusual spectral features lead me to conclude that a single metallicity value with corresponding α abundance cannot always reproduce observed features in the spectra, and that in reality the chemical composition of the stars in my sample is more complex than I had assumed.

3.8 Summary

I found that for a given temperature, an ultra subdwarf can be smaller than a dwarf star by up to a factor of five, and that the Baraffe et al. (1997) stellar evolution models are in agreement with the data, providing some of the first validation of these models for the lowest stellar temperatures and metallicities. I also presented relations

that can be used to convert direct observables, such as color and absolute K-band magnitude, to stellar radii for metallicities down to -2.0 dex with radius uncertainties of $\sim 20\%$ and 6%, respectively.

Chapter 4

The Effects of Strong Magnetic Fields on M dwarf Radii

A similar version of this Chapter was published by the Astronomical Journal in Kesseli et al. (2018).

4.1 Introduction

Measurements of M dwarf radii from EBs reveal sizes that are as much as $10-15\%$ larger than theoretical predictions from stellar evolutionary models, and are on average inflated by $\sim 5\%$ (e.g., Torres & Ribas 2002; Kraus et al. 2011; Han et al. 2017). As discussed in Chapter 1.6.2, several studies have proposed that the larger-than-expected radii of M dwarf stars in EBs are a result of activity and enhanced magnetic fields (often around a few kiloGauss for M dwarf stars; Donati et al. 2006; Chabrier et al. 2007; López-Morales 2007). Alternatively, the inflation may solely be an effect present in EBs due to differing evolutionary histories or inaccuracies in parameter extraction from EB data (see Section 1.4.1 for more details).

Magnetic field strength and magnetic activity have long been known to be coupled to rotation (Parker 1955), and more recent observations affirm that M dwarf stars with rotation periods less than $\sim$5 days all show evidence of magnetic activity through chromospheric emission (e.g., West et al. 2015; Newton et al. 2017). In this scenario, EBs are preferentially inflated because of observational biases: they tend to have short orbital periods ($P < 5$ days) and are correspondingly synchronously

rotating. To account for inflation suggested by this theory, studies such as Kraus et al. (2011) have suggested adding a rotation parameter into Mass−Radius relations for M dwarfs.

A large fraction of *single* M dwarfs are also found to be rapid rotators. Newton et al. (2016) found that more than one-third of the mid-to-late M dwarf stars with measured rotation periods in the MEarth survey have rotational periods less than one day. If rotation-induced magnetic fields cause larger-than-expected radii in EBs, then a large number of single stars should also have larger-than-expected radii. As of now, there is not a sample of rapidly rotating single stars with precise radius measurements; the mid-to-late M dwarf stars for which interferometric radii measurements are available (Proxima Centauri and Barnard's Star; Boyajian et al. 2012) have rotation periods around 80-130 days (Benedict et al. 1998).

To determine the effects of rapid rotation (and hence strong magnetic fields) have on the radii of stars, a sample of rapidly rotating, single, fully convective stars needs to be studied to determine the level of inflation present. In this Chapter, I test the role of rapid rotation on M dwarf radii by measuring the statistical distribution of radii modulated by the inclination ($\sin i$) of 88 single, rapidly rotating M dwarfs.

To determine the $R \sin i$ distribution, I combined photometric rotation periods with $v \sin i$ values that I measured in this work. My measurements of $v \sin i$ are obtained through rotational broadening of absorption lines. The measured $v \sin i$ and published rotational periods ($P_{\rm rot}$) are related to the stellar radius (R) as follows:

$$R \sin i = v \sin i \; P_{\rm rot} \; / \; (2\pi) \tag{4.1}$$

In the following sections I will detail how I determined each of these values and then how I used the $R \sin i$ distribution to determine the amount of radius inflation present in the sample.

4.2 Literature Rotation Periods

All of the photometric rotation periods are from the MEarth survey (Charbonneau et al. 2009). Since 2008, MEarth has been photometrically monitoring close to 2000 targets selected to be mid-to-late (M3−M6) M dwarf stars with an average photometric precision of 1.5% (Berta et al. 2012; Dittmann et al. 2014). The survey was designed to find transiting exoplanets around nearby M dwarf stars, however Newton et al. (2016) used the photometry to determine rotation periods by fitting modulations due to starspots passing into and out of view.

I selected stars that had a secure periodic detection of photometric modulation (class 'A' or 'B' rotators from Newton et al. 2016). I also required the stars to have a period of less than 5 days, to ensure they were all magnetically active and had $v \sin i$ values that could be resolved with the spectrographs that I used. A large portion of the sample have H-α measurements, and every star with a measurement is magnetically active (Newton et al. 2017). I only observed stars with K_s-band magnitudes brighter than 11, since fainter magnitudes required significantly longer exposure times and often returned poorer SNRs. To isolate the single stars, I eliminated from the sample any stars that were flagged as binaries by Newton et al. (2017), which includes both removal of blended or elongated PSFs and sources flagged as being overluminous for their given color. The multiplicity fraction of M dwarf stars is not precisely known, however current estimates state that $26 \pm 3\%$ of M dwarf stars are multiples (Duchêne & Kraus 2013). 23% of the targets in my sample were flagged as binaries, leading me to conclude that binaries and multiples have been removed from the sample. I also visually inspected all the cross-correlation functions to look for multiple peaks and found only one of the targets to be a previously unknown spectroscopic binary (noted in Table 4.1). Finally, because MEarth stars were selected to be mid-to-late M dwarf stars, all of the stars in the sample have mass estimates

reported in Dittmann et al. (2014) that put them around or past the fully convective limit ($M_\star \lesssim 0.4 M_{\rm Sun}$). After these cuts, I was left with 110 potential targets from Newton et al. (2016), 83 of which I observed, and 7 more that had precise $v \sin i$ measurements from the literature (discussed in more detail in Section 4.3.2).

4.3 Rotational Broadening

4.3.1 Observations and Data Reduction

Data were collected between October 2016 and November 2017 using the Immersion GRating INfrared Spectrograph (IGRINS; Park et al. 2014) on Lowell Observatory's 4.3-meter Discovery Channel Telescope (DCT) at and the 2.7-meter Harlan J. Smith Telescope at McDonald Observatory. I also used iSHELL (Rayner et al. 2016) on NASA's 3.0-meter Infrared Telescope Facility (IRTF) on Mauna Kea, Hawaii. IGRINS is a high-resolution (R $\simeq$ 45,000) infrared spectrograph that simultaneously collects H and K-band spectra (Mace et al. 2016). iSHELL has a spectral resolution of 75,000 at my chosen wavelength region in the K-band ($2.26 - 2.55 \mu m$). The instrument, telescope and observation date for each target are shown in Table 4.1. Exposure times were chosen in order to achieve a signal-to-noise ratio (SNR) of $\sim$100. I found that spectra with a SNR significantly lower than 100 yielded large uncertainties in the final calculated $v \sin i$ value and, hence, yielded less precise radius estimates.

With the spectral resolution of IGRINS and iSHELL, I was able to resolve rotational broadening for $v \sin i$ values larger than $\sim$3$-$4 km s^{-1} and $\sim$1$-$2 km s^{-1}, respectively. In order to resolve rotational broadening in the largest number of stars, I used IGRINS to observe stars with rotation periods less than a day ($v_{rot} \gtrsim 10$ km s^{-1}) and iSHELL to observe stars with rotation periods between one and five days ($3 \lesssim v_{rot} \lesssim 10$ km s^{-1}).

I performed the data reduction of IGRINS spectra using the publicly available pipeline (Lee et al. 2017).[1] The pipeline automatically performs dark subtraction, flat fielding, and subtracts out sky emission (i.e., OH airglow) using an ABBA nodding pattern. The pipeline also returns a wavelength solution, calculated using the OH emission lines before their removal. The final product is a 1-D spectrum, which is calibrated but still contains telluric absorption features. I completed the data reduction of the iSHELL spectra using the Spextool for iSHELL package[2]. Spextool (Cushing et al. 2004) was originally created for reduction of SpeX data; however, it has been updated in the newest release to be compatible with iSHELL data. I used the `xspextool` function to perform the dark subtraction, flat fielding, order tracing and extraction, linearity correction and wavelength extraction. `xspextool` also returns a wavelength solution calibrated using ThAr lamps.

Large parts of the H and K-bands are dominated by telluric lines. I removed telluric absorption features using the `xtellcor` function (Vacca et al. 2003), which is also part of the larger Spextool reduction package. Since Spextool is not formatted for IGRINS spectra, I utilized `xtellcor_general` for telluric correction of IGRINS spectra. `xtellcor_general` can be used with any instrument, given the spectral resolution, an A0 standard spectrum, and a target spectrum. A0 standard stars were taken throughout the night during all observations and were required to deviate in airmass from the target by less than 0.2. Examples of my reduced and telluric corrected spectra are shown in Figure 4.1.

4.3.2 $v \sin i$ Calculation

The method I used to determine $v \sin i$ values is similar to that of many previously published studies (e.g., West & Basri 2009; Muirhead et al. 2013; Reiners

[1] `https://github.com/igrins/plp`
[2] `http://irtfweb.ifa.hawaii.edu/research/dr_resources/`

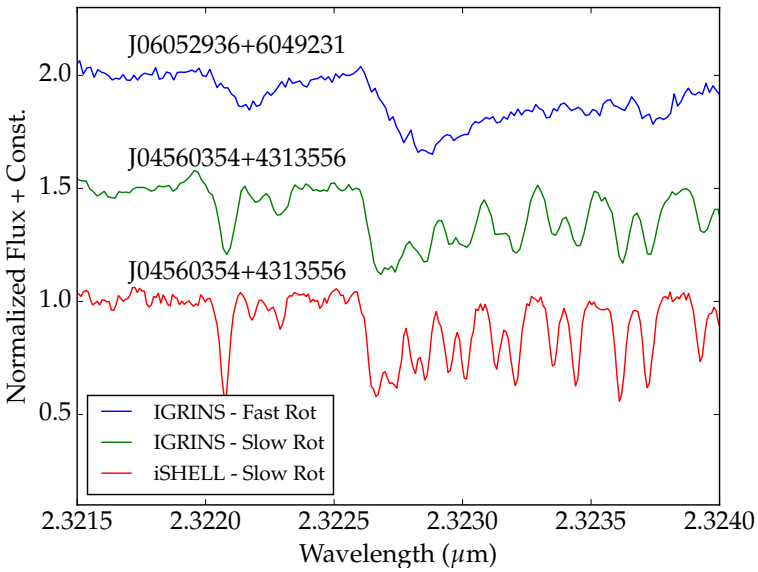

Fig. 4.1: IGRINS and iSHELL spectra from the sample, centered on the 1-0 vibrational CO bandhead ($\sim 2.3\mu m$). The blue line shows a rapidly rotating M dwarf with a measured $v \sin i$ of 29.8 km/s (J06052936+6049231) taken with IGRINS. The green line below shows a slowly rotating M dwarf (J04560354+4313556) also taken with IGRINS. The rapidly rotating M dwarf clearly has much broader and shorter absorption lines than the slowly rotating M dwarf. The bottom red line shows the same slowly rotating M dwarf star (again, J04560354+4313556) but taken with iSHELL. The difference in broadening between the two spectra of J04560354+4313556 is entirely due to the resolution difference between the spectrographs. This plot demonstrates why I was able to observe slower rotators with iSHELL.

et al. 2017). To determine the rotational broadening, I compared the rapidly rotating M dwarf stars to slowly rotating M dwarf stars (P $>$ 50 days), also from the Newton et al. (2016) sample. In the slowly rotating stars, the rotational broadening is undetectable, and any broadening seen is due to the intrinsic broadening of the spectrograph (see Figure 4.1 for an example of how the change in resolution of the two spectrographs broadens the spectra).

To start, the slow rotators were artificially broadened using the $v \sin i$ kernel, `rotBroad`, available in the PyAstronomy library.[3] The rotational broadening kernel

[3] `https://github.com/sczesla/PyAstronomy`

requires a linear limb darkening coefficient (μ) as input. I referred to Claret et al. (2012) to determine the appropriate value of μ, and found that for my sample of stars ($2900 \lesssim T_{eff} \lesssim 3400$) and for H and K-band observations, the linear limb darkening coefficient varies between $\sim 0.3 - 0.4$. So as to not have the choice of limb darkening coefficient bias the final results, I treated it as a nuisance parameter in the Bayesian analysis (see Section 4.4.2 for details). For all of the reported $v \sin i$ values, I used a coefficient of 0.35 since it falls in the middle of the allowed range.

Next, to determine the $v \sin i$ value, the artificially broadened slow rotators were cross-correlated with the original unbroadened spectrum of the slow rotator. The width of the cross-correlation function monotonically increases with increasing rotational broadening. I created a relation between the full width at half maximum (FWHM) of the cross-correlation function to the $v \sin i$ input value of the kernel used to artificially broaden the spectrum. I then cross-correlated the fast rotators to the slowly rotating M dwarf star and interpolated from the FWHM relation to determine a $v \sin i$ value for each fast rotator. Example cross-correlation functions, showing the artificially broadened spectra cross-correlated with the unbroadened spectrum (blue-yellow), and the rapidly rotating target spectrum cross-correlated with the unbroadened spectrum (red), are shown in Figure 4.2.

I performed this analysis on individual orders and excluded orders that:

- had low signal-to-noise: the first and last few orders of all spectra are excluded as well as any orders with obvious noise spikes
- were dominated by telluric features
- contained large atomic features (i.e., Na doublet $\sim 2.2 \mu m$), which are subject to non-Gaussian pressure broadening and therefore can lead to over-estimated $v \sin i$ measurements

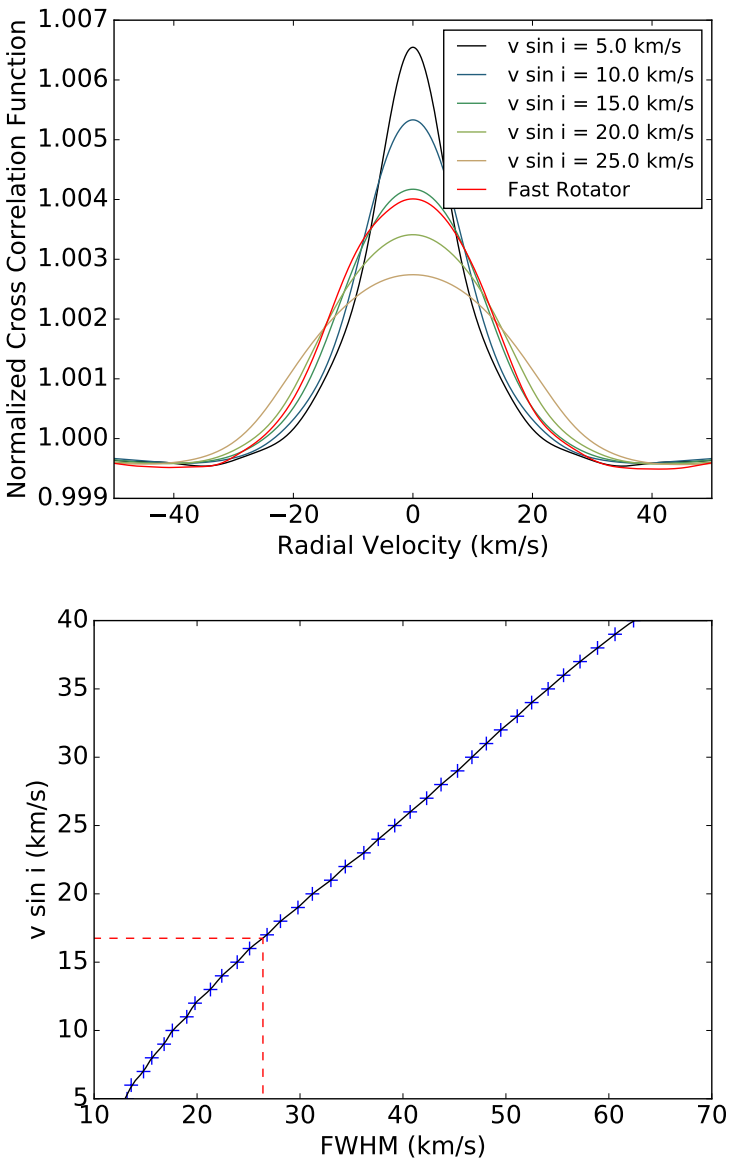

Fig. 4.2: **Top:** Resulting cross-correlation function between a slowly rotating M4.9 (Alonso-Floriano et al. 2015) dwarf star (J04560354+4313556) and a rapidly rotating M5.9 (Shkolnik et al. 2009) dwarf star (J10204406+0814234), as well as the slow rotator with a few artificially broadened spectra. The darkest blue lines have the smallest $v \sin i$ kernel applied to the slow rotator's spectrum, while the yellow lines used the largest $v \sin i$ kernel. **Bottom:** My relation for the measured FWHM versus the $v \sin i$ value for the stars mentioned above. The blue plus signs show the measured FWHM values for the artificially broadened slow rotators, and the black line shows the interpolated relation. The red dashed line shows the measured FWHM of the rapid rotator, and the interpolated $v \sin i$ value. For this specific order I measure a $v \sin i$ of 16.75 km s^{-1}.

I found that the CO bands ($\sim 2.3\mu m$) were ideal for this calculation and returned especially precise measurements of $v \sin i$. The relatively high mean molecular weight of CO and the low Landè g factors for these particular CO transitions reduce the dependence of the line widths on magnetic fields and pressure broadening, respectively. For spectra obtained with iSHELL all of my $v \sin i$ measurements were obtained from orders containing CO band features. For spectra obtained with IGRINS, the CO bands dominated about half the orders that were used. Because of this, I am confident that the broadening I measured is due to rotation and not magnetic or pressure broadening. Uncertainties were calculated from the standard deviation between $v \sin i$ measurements in different orders.

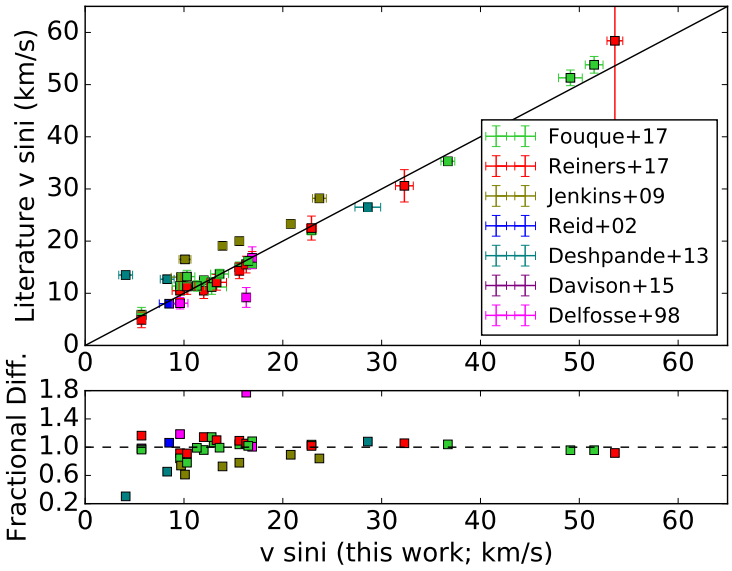

Fig. 4.3: Previously recorded literature values of $v \sin i$ compared to $v \sin i$ values measured in this work. The fractional difference in the bottom panel is given by the $v \sin i$ (this work) divided by the $v \sin i$ from the literature.

Some of my targets have measured $v \sin i$ values in the literature, and I compared my results to these previous measurements. These are shown in Figure 4.3 and listed in Table 4.1. Although I found a similar trend in the data, the spread is larger than

the reported uncertainties. Even with this spread, I am confident in my measurements because I achieved the greatest agreement (74% of points within 1σ, all within 2σ) between surveys that used the spectrographs with the highest resolution ($R \sim 57,000$, Davison et al. 2015; $R > 80,000$, Reiners et al. 2017; $R \sim 65,000$, Fouqué et al. 2018). All the points with greater levels of discrepancy were measurements taken with spectrographs with lower resolution than my survey ($R < 45,000$).

Because of the consistent measurements with both Reiners et al. (2017) and Fouqué et al. (2018), I added 7 of their $v \sin i$ measurements to my sample. These measurements met all of the criteria listed in Section 4.2, but I did not measure a $v \sin i$ value for these objects. This increased my total sample to 88 stars. The targets added from Reiners et al. (2017) and Fouqué et al. (2018) are listed in Table 4.1.

4.4 The Bayesian Statistical Approach

I combined my measured $v \sin i$ values with rotation periods using Equation 4.1, and in a method similar to that of previous studies (Jackson et al. 2009, 2016, 2018), I determined the average inflation (if any) of the radii of the stars in comparison to previously published radius predictions. Unlike previous studies, however, here I used a completely Bayesian framework for the statistical analysis.

In the following analysis the predicted radius is referred to as R_p. Table 4.2 outlines how I arrived at R_p and how I have labeled each method in the below text. All methods began with absolute K_s-band magnitudes (M_{K_s}) for each star, which were determined by combining 2MASS apparent K_s-band magnitudes with parallax measurements reported in Dittmann et al. (2014). M_{K_s} was transformed into a radius directly, or first into a mass (using an M_{K_s} - Mass relation) and subsequently into a radius (using a Mass-Radius relation). I have also denoted which relations use empirical data and which relations are from stellar evolutionary models.

The Dartmouth Stellar Evolution Model isochrones utilize the updated 2012 photometric systems and were created using the online Web Tool [4]. The Padova stellar evolutionary models were obtained using the online[5] using PARSEC v1.0. The Mesa Isochrones and Stellar Tracks (MIST) models were generated using the online web interpolator[6]. All three of the stellar evolutionary models used a 5 Gyr isochrone and a metallicity of 0.14 dex (i.e., the average metallicity of rapid rotators with metallicities estimated in Newton et al. 2014). The BHAC model used a 5 Gyr isochrone as well, however super-solar metallicity isochrones are not publicly available so I used the solar metallicity isochrone. I chose a 5 Gyr isochrone because I do not have individual age estimates, and previous studies that compared radii to model predictions almost exclusively used this age (e.g., Boyajian et al. 2012; Han et al. 2017). I discuss the effects of changing the metallicity and age of the isochrone in Section 4.6.

My goal was to estimate the percentage by which the radii are inflated given the predicted radii (R_p) and the measured $R \sin i$ values of the sample. Thereafter, I refer to these as $\mathbf{R_p}$ and **Rsini**, respectively, where the boldface text indicates that these are arrays of values. I introduced an inflation parameter (η), which can take a value ranging from 0.9 to 1.25 (corresponding to a radius inflation of -10% through 25%). To simulate different levels of radius inflation, each value in $\mathbf{R_p}$ was multiplied by η then compared to **Rsini**.

[4] `http://stellar.dartmouth.edu/models/isolf_new.html`
[5] `http://stev.oapd.inaf.it/cgi-bin/cmd_3.0`
[6] `http://waps.cfa.harvard.edu/MIST/interp_isos.html`

Table 4.1: Target list and measured $v \sin i$ values

2MASS name	Observation Date (UT)	Telescope	Instrument	$P_{\rm rot}$ (d)[1]	$v \sin i$ (km/s)	$\sigma_{v \sin i}$ (km/s)	Previous $v \sin i$	Previous $\sigma_{v \sin i}$	Reference
				Continued					
J00243478+3002295	24 Sept 2017	DCT	IGRINS	1.077	13.0	0.5	12.2	0.8	F17[2]
J00304867+7742338	24 Sept 2017	DCT	IGRINS	0.137	30.5	0.9			
J00544803+2731035	2 Aug 2017	IRTF	iSHELL	1.697	9.0	0.7			
J01015952+5410577	25 Sept 2017	DCT	IGRINS	0.278	31.9	0.9	30.6	3.1	R17[3]
J01533076+0147559	10 Nov 2017	DCT	IGRINS	0.199	34.3	3.3			
J01534955+4427284	26 Sept 2017	DCT	IGRINS	0.216	47.6	2.9			
J01564570+3033288	2 Aug 2017	IRTF	iSHELL	1.581	6.7	0.8			
J01584517+4049445	24 Sept 2017	DCT	IGRINS	0.486	21.8	0.5			
J02032864+2134168	11 Nov 2017	DCT	IGRINS	0.32	27.7	1.5			
J02071032+6417114	1 Sept 2017	IRTF	iSHELL	1.177	11.3	0.9	11.4	1.0	F17
J02170993+3526330	25 Sept 2017	DCT	IGRINS	0.276	23.5	0.7	28.2	0.7	J09[4]
J02204625+0258375	24 Sept 2017	DCT	IGRINS	0.503	20.7	0.4	23.3	0.7	J09
J02351494+0247534	26 Sept 2017	DCT	IGRINS	0.472	7.9	0.7			
J02364412+2240265	25 Sept 2017	DCT	IGRINS	0.37	12.7	1.4	11.2	1.4	F17
J02514973+2929131	26 Sept 2017	DCT	IGRINS	0.895	19.2	1.7			
J03205965+1854233	24 Sept 2017	DCT	IGRINS	0.614	8.4	1.1	8.0	-	R02[5]
J03284958+2629122	6 Nov 2017	IRTF	iSHELL	3.235	2.8	0.4			
J03304890+5413551	14 Nov 2017	DCT	IGRINS	0.117	47.7	2.1			

[2]Fouqué et al. (2018)
[3]Reiners et al. (2017)
[4]Jenkins et al. (2009)
[5]Reid et al. (2002)

2MASS name	Observation Date (UT)	Telescope	Instrument	$P_{\rm rot}$ (d)	$v \sin i$ (km/s)	$\sigma_{v \sin i}$ (km/s)	Previous $v \sin i$	Previous $\sigma_{v \sin i}$	Reference
J03360868+3118398	24 Sept 2017	DCT	IGRINS	0.856	15.7	0.4			
J03425325+2326495	26 Sept 2017	DCT	IGRINS	0.834	8.3	0.7	12.7	0.5	D13[6]
J03571999+4107426	12 Nov 2017	DCT	IGRINS	0.567	6.5	0.8			
J04121693+6443560	6 Nov 2017	IRTF	iSHELL	1.594	7.2	0.2			
J04140201+8215360	10 Nov 2017	DCT	IGRINS	0.277	17.0	0.8			
J04171852+0849220	25 Sept 2017	DCT	IGRINS	0.185	37.3	1.1			
J04201254+8454062	12 Nov 2017	DCT	IGRINS	0.695	15.2	0.7			
J04302527+3951000	12 Nov 2017	DCT	IGRINS	0.718	14.2	0.5	13.6	0.8	F17
J04333393+2044461	11 Nov 2017	DCT	IGRINS	0.335	27.1	2.0			
J04434430+1505565	14 Nov 2017	DCT	IGRINS	0.419	22.3	0.5			
J04490464+5138412	12 Nov 2017	DCT	IGRINS	0.724	9.7	0.7			
J05041476+1103238	11 Nov 2017	DCT	IGRINS	0.842	10.8	1.4			
J05062489+5247187	10 Nov 2017	DCT	IGRINS	0.648	14.5	1.1			
J05405390+0854183	10 Nov 2017	DCT	IGRINS	0.332	15.5	0.6			
J05595569+5834155	11 Nov 2017	DCT	IGRINS	0.951	9.2	1.7			
J06000351+0242236	6 Nov 2017	IRTF	iSHELL	1.809	5.7	0.4	5.8,5.9	0.3,1.4	D15[7],F17
J06052936+6049231	10 Nov 2017	DCT	IGRINS	0.31	29.7	2.6			
J06073185+4712266	28 Jan 2017	DCT	IGRINS	0.862	20.8	0.8			
J06235123+4540050	6 Nov 2017	IRTF	iSHELL	2.515	6.7	0.6			
J06481555+0326243	12 Nov 2017	DCT	IGRINS	0.458	9.2	0.7			
J07454039+4931488	11 Nov 2017	DCT	IGRINS	0.253	18.5	1.8			
J07464203+5726534	30 Jan 2017	DCT	IGRINS	0.82	17.6	0.8			

[6]Deshpande et al. (2013)
[7]Davison et al. (2015)

2MASS name	Observation Date (UT)	Telescope	Instrument	$P_{\rm rot}$ (d)	$v \sin i$ (km/s)	$\sigma_{v \sin i}$ (km/s)	Previous $v \sin i$	Previous $\sigma_{v \sin i}$	Reference
J07555396+8323049	11 May 2017	HJS[8]	IGRINS	1.107	13.4	1.2			
J08012112+5624042	11 Nov 2017	DCT	IGRINS	0.117	66.0	0.5			
J08055713+0417035	10 Nov 2017	DCT	IGRINS	0.176	29.7	1.5			
J08212804+5220587	12 Nov 2017	DCT	IGRINS	0.472	12.7	0.4			
J08294949+2646348	28 Jan 2017	DCT	IGRINS	0.459	9.6	0.8	8.1,10.5,11.4	1.1,1.5,0.7	D98[9],R17,F17
J08505062+5253462	6 Nov 2017	IRTF	iSHELL	1.754	9.6	1.1	13.1	0.7	J09
J08593592+5343505	29 Jan 2017	DCT	IGRINS	0.581	26.9	0.8			
J09002359+2150054	30 Jan 2017	DCT	IGRINS	0.439	15.5	0.4	20.0,14.3,15.0	0.6,1.5,1.0	J09,R17,F17
J09245082+3041373	10 Nov 2017	DCT	IGRINS	0.373	44.9	3.1			
J09535523+2056460	30 Jan 2017	DCT	IGRINS	0.615	10.1	0.6	16.5	0.4	J09
J09585650+0558000	29 Jan 2017	DCT	IGRINS	0.453	22.3	0.4			
J09591880+4350256	30 Jan 2017	DCT	IGRINS	0.755	22.5	0.7			
J10011109+8109226	11 May 2017	HJS	IGRINS	0.302	21.3	3.1			
J10024936+4827333	29 Jan 2017	DCT	IGRINS	0.268	18.4	0.4			
J10030191+3433197	30 Jan 2017	DCT	IGRINS	0.859	11.9	0.2			
J10204406+0814234	10 Nov 2017	DCT	IGRINS	1.087	17.1	1.0			
J10252645+0512391	12 Nov 2017	DCT	IGRINS	0.102	59.9	2.1			
J10521423+0555098	30 Jan 2017	DCT	IGRINS	0.692	13.6	0.4	19.1	0.2	J09
J11005043+1204108	30 Jan 2017	DCT	IGRINS	0.298	28.6	1.3	26.5	0.8	D13
J11224274+3755484	8 May 2017	HJS	IGRINS	0.358	13.3	0.8			
J11432359+2518137	10 Nov 2017	DCT	IGRINS	1.326	13.5	0.9	13.7	0.9	F17
J11483548+0741403	28 Jan 2017	DCT	IGRINS	0.708	14.0	0.5			
J12041256+0514128	29 Jan 2017	DCT	IGRINS	0.154	23.0	0.5			

[8]Harlan J. Smith
[9]Delfosse et al. (1998)

2MASS name	Observation Date (UT)	Telescope	Instrument	$P_{\rm rot}$ (d)	$v \sin i$ (km/s)	$\sigma_{v \sin i}$ (km/s)	Previous $v \sin i$	Previous $\sigma_{v \sin i}$	Reference
J12185939+1107338	30 Jan 2017	DCT	IGRINS	0.491	16.3	0.4	9.2,15.6	1.9,0.8	D98,F17
J12265737+2700536	28 Jan 2017	DCT	IGRINS	0.733	4.0	0.7	13.5	0.6	D13
J13003350+0541081	29 Jan 2017	DCT	IGRINS	0.6	16.9	0.5	16.8,15.6	2.1,0.8	D98,F17
J13093495+2859065	28 Jan 2017	DCT	IGRINS	0.215	48.6	1.1	51.3	1.5	F17
J13533877+7737083	-	-	-	1.231	-	-	8.9	1.5	R17
J14224340+1624464	29 Jan 2017	DCT	IGRINS	0.889	8.0	0.5			
J14311348+7526423	30 Jan 2017	DCT	IGRINS	0.631	14.3	0.4			
J15163731+5355457	30 Jan 2017	DCT	IGRINS	0.525	19.2	0.4			
J15164073+3910486	30 Jan 2017	DCT	IGRINS	0.581	16.3	0.4			
J16400599+0042188	-	-	-	0.311	-	-	31.0	0.8	F17
J16402068+6736046	-	-	-	0.378	-	-	10.8	0.7	F17
J18021660+6415445	11 May 2017	HJS	IGRINS	0.28	10.3	0.9	11.3,13.2	1.5,1.2	R17,F17
J18315610+7730367	-	-	-	0.861	-	-	15.8	0.7	F17
J18481752+0741210	-	-	-	2.756	-	-	2.4	1.5	R17
J19510930+4628598	May 2017	HJS	IGRINS	0.593	22.9	0.5	22.1	0.9	F17
J20045709+0321076	17 Oct 2016	DCT	IGRINS	0.788	12.0	0.5			
J22482247+1232105	17 Oct 2016	DCT	IGRINS	0.633	7.7	1.1			
J22502051+5136265	24 Sept 2017	DCT	IGRINS	0.883	11.0	0.5			
J22541111+2527562	18 Oct 2016	DCT	IGRINS	0.356	8.7	0.5			
J23025250+4338157	18 Oct 2016	DCT	IGRINS	0.348	29.0	1.5			
J23270216+2710367	25 Sept 2017	DCT	IGRINS	0.922	13.0	0.5			
J23310587+0842314[10]	25 Sept 2017	DCT	IGRINS	1.647	9.1	0.8			
J23383392+0624518	19 Oct 2016	DCT	IGRINS	0.251	31.7	1.1			
J23512227+2344207	-	-	-	3.211	-	-	5.2	0.9	F17

[10]Spectroscopic Binary

2MASS name	Observation Date (UT)	Telescope	Instrument	$P_{\rm rot}$ (d)	$v \sin i$ (km/s)	$\sigma_{v \sin i}$ (km/s)	Previous $v \sin i$	Previous $\sigma_{v \sin i}$	Reference
J23545147+3831363	-	-	-	4.755	-	-	3.6	1.5	R17

In Bayesian inference, oftentimes there are parameters in the model that are not parameters of interest— called nuisance parameters. There are two such parameters in my analysis. The first is a cutoff in the $\sin i$ value. By using spot modulation to determine stellar rotation periods, an inclination bias may have been introduced into the sample since stars with pole-on orientations are not detectable: the spots do not rotate into and out of view and therefore do not cause photometric modulation. I used the variable κ to represent the cutoff below which I do not measure any $\sin i$ values. The linear limb darkening coefficient (μ), which was used as an input to the $v \sin i$ kernel, was treated as the second nuisance parameter. In Section 4.4.2 I show how I marginalized over these parameters so they are not included in the final results, but for now I leave them in the analysis.

I determined the most likely value of η using Bayes' theorem. Following the notation of Gregory (2005), I construct the following form of Bayes' theorem:

$$\begin{aligned} p(\eta, \mu, \kappa | \mathbf{Rsini}, \mathbf{R_p}) &= \frac{p(\eta, \mu, \kappa | \mathbf{R_p})\ p(\mathbf{Rsini} | \eta, \mu, \kappa, \mathbf{R_p})}{p(\mathbf{Rsini} | \mathbf{R_p})} \\ &= \prod_{j=1}^{88} \frac{p(\eta, \mu, \kappa | R_{p,j})\ p((R \sin i)_j | \eta, \mu, \kappa, R_{p,j})}{p((R \sin i)_j | R_{p,j})}, \end{aligned} \tag{4.2}$$

where the subscripted and unbolded symbols represent values for an individual star, which are each multiplied together in the product to get the posterior probability function, ($p(\eta, \mu, \kappa | \mathbf{Rsini}, \mathbf{R_p})$). The posterior probability function is a probability distribution for different values of η (and κ, μ), given the data (**Rsini**) and assuming that $\mathbf{R_p}$ is correct. The most likely value of η is given by the peak of the posterior probability function. Any previously known information about inflation can be incorporated into the prior, $p(\eta | \mathbf{R_p})$. Because I did not have much information on how likely different inflation values were, I used a uniform prior for the analysis (the

Table 4.2. Radius prediction methods

Method Name	M_{K_s} - Mass Reference	Mass - Radius Reference	M_{K_s} - Radius Reference	Reported in
Benedict+Boyajian	Benedict et al. (2016)*	Boyajian et al. (2012)*	None	None
Mann15	None	None	Mann et al. (2015)*	None
Dittmann14	Delfosse et al. (2000)*	Boyajian et al. (2012)*	None	Dittmann et al. (2014)
Newton16	Delfosse et al. (2000)*	Bayless & Orosz (2006)*	None	Newton et al. (2016)
Benedict+Dartmouth	Benedict et al. (2016)*	Dotter et al. (2008) †	None	None
Dartmouth	None	None	Dotter et al. (2008)†	None
Benedict+Padova	Benedict et al. (2016)*	Bressan et al. (2012)†	None	None
Benedict+MIST	Benedict et al. (2016)*	Choi et al. (2016)†	None	None
Benedict+BHAC	Benedict et al. (2016)*	Baraffe et al. (2015)†	None	None

*Empirically derived relation

†Stellar Evolutionary Model

exact choice of prior is discussed in more detail in Section 4.5). The likelihood function is given by $p(\mathbf{Rsini}|\eta, \mu, \kappa, \mathbf{R_p})$ and is the probability of obtaining the data. Lastly, $p(\mathbf{Rsini}|\mathbf{R_p})$ is the normalization factor and is the integrated probability over all values of η, μ and κ, within their respective prior boundaries.

4.4.1 Constructing the Likelihood Function

To construct the likelihood function, I combined a series of probability distribution functions (PDFs) to determine $p((R\sin i)_j|\eta, \mu, \kappa, R_{p,j})$ for each star. Here I will not discuss the nuisance parameters, μ and κ, Discussion of μ and κ will be given in the next section (4.4.2). For the remainder of this section, I used the radii obtained using the Dittmann et al. (2014) method from Table 4.2 as R_p, and in Section 4.5 I show the results from other radius predictions.

I followed the formalism of Gregory (2005) for combining PDFs to construct the likelihood functions. I start by defining the variables I used throughout:

$$x = \sin i \tag{4.3}$$

$$y = (R\sin i)_j \tag{4.4}$$

$$z = \eta \times R_{p,j}\sin i \tag{4.5}$$

where x and z are variables with different probabilities and y is my measurement. I calculated the PDFs for x and, subsequently, z. The PDFs are written using the notation $f_X(x)$, where X is the proposition that the value x is within $x + dx$.

$$f_X(x) = \frac{x}{\sqrt{1-x^2}}dx \tag{4.6}$$

$f_X(x)$ gives the geometric probability of measuring $\sin i$, assuming a randomly oriented rotational axis with uniform probability over a sphere. The PDF for z is more complicated, and I first combined the PDFs of $R_{p,j}$ and x. The PDF of $R_{p,j}$ is a normal Gaussian of the form:

$$f_{R_p}(r) = \frac{1}{\sqrt{2\pi\sigma_{r,j}^2}} \exp \frac{-(r - \eta R_{p,j})^2}{2\sigma_{r,j}^2} \tag{4.7}$$

where $\sigma_{r,j}$ is the uncertainty associated with each radius estimate (here 5%; Dittmann et al. 2014). $f_X(x)$ and $f_{R_p}(r)$ are then combined using a product distribution.

$$f_Z(z) = \int_{-\infty}^{\infty} f_X(x) f_{R_p}(z/x) \frac{1}{|x|} dx \tag{4.8}$$

I combined the measurement uncertainty associated with y with the PDF to create the final likelihood function for an individual star. I combined the measurement uncertainties with $f_Z(z)$ using a convolution given by

$$p((R \sin i)_j | \eta, \mu, \kappa, R_{p,j}) = \int_{-\infty}^{\infty} dz f_Z(z) f_E(y - z) \tag{4.9}$$

where $f_E(y-z)$ is the PDF of the measurement uncertainty and given by the following normal Gaussian distribution

$$f_E(y - z) = \frac{1}{\sqrt{2\pi\sigma_{m,j}^2}} \exp \frac{-(y - z)^2}{2\sigma_{m,j}^2} \tag{4.10}$$

where $\sigma_{m,j}$ is the uncertainty associated with each of my $(R \sin i)_j$ measurements, and includes both the propagated uncertainties in my $v \sin i$ measurements and the uncertainties in the periods reported by Newton et al. (2016). Combining Equations

4.10 and 4.8 with Equation 4.9, I obtained the final equation for the likelihood function

$$p((R\sin i)_j|\eta,\mu,\kappa,R_{p,j}) = \int_{z=-\infty}^{z=\infty}\int_{x=0}^{x=1} \frac{1}{\sqrt{4\pi^2\sigma_{m,j}^2\sigma_{r,j}^2}}\frac{x}{\sqrt{1-x^2}}\frac{1}{|x|}\times \exp\left(\frac{-(z/x-\eta R_{p,j})^2}{2\sigma_{r,j}^2}+\frac{-(y-z)^2}{2\sigma_{m,j}^2}\right)dz\ dx. \tag{4.11}$$

Since Equation 4.11 cannot be integrated analytically, I integrated it numerically using the `scipy integrate.dblquad` function, which is specifically tailored for numerical integration of double integrals. The value returned by the integral for $p((R\sin i)_j|\eta,\mu,\kappa,R_{p,j})$ is the probability of the data given the model for one single $(R\sin i)_j$ measurement. I repeated this integration for each object and combined the probabilities by multiplying all the individual probability values together. Then, to construct the likelihood function I again repeated the process for the entire range of η to obtain a probability of measuring the data for each η in the inflation range.

4.4.2 Marginalizing Over Nuisance Parameters

To remove the nuisance parameters from the final likelihood function, I integrated over them to create a marginalized likelihood function. This is given mathematically by the following:

$$p(\eta|\mathbf{Rsini},\mathbf{R_p}) = \int_{\kappa=0.0}^{\kappa=0.4}\int_{\mu=0.3}^{\mu=0.4} d\kappa\ d\mu\ p(\eta,\mu,\kappa|\mathbf{Rsini},\mathbf{R_p}) \tag{4.12}$$

I first explored the $\sin i$ distribution bias (κ). I cut off the tail of the $\sin i$ PDF used in the likelihood function analysis at a range of $\sin i$ values from 0.0 through 0.4. The PDFs for the $R\sin i$ distributions for a single star are shown in Figure 4.4.

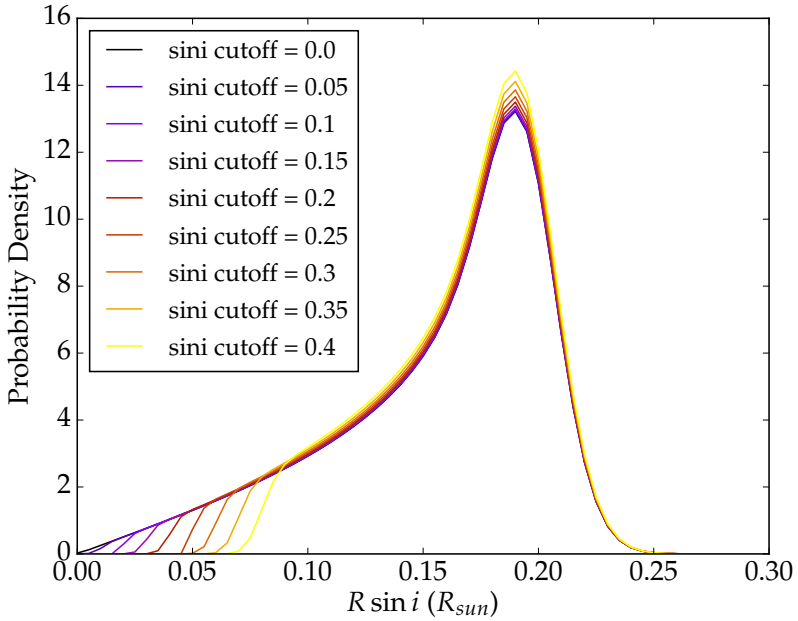

Fig. 4.4: Probability distribution functions of $R \sin i$ for a single star. This star was assigned a radius of 0.2 $R_{\rm Sun}$. The purple line ($\sin i$ cutoff of 0.0) shows the full $R \sin i$ expected distribution that I used in all my previous analyses. Larger $\sin i$ cutoffs show what the PDF would look like if I assumed that the sample from Newton et al. (2016) did not include stars with inclinations close to pole-on. The larger the $\sin i$ cutoff, the more biased the sample is against pole-on inclinations.

Following in my likelihood analysis as before, I created likelihood functions, but this time for a range of $\sin i$ cutoff values. The resulting likelihood functions are shown in Figure 4.5. The figure shows that the most likely $\sin i$ cutoff is 0.2, meaning that the Newton et al. (2016) sample does not include stars with inclinations within $\sim 12^\circ$ of pole-on. Given my data, it is unlikely that there exists a $\sin i$ cutoff $\gtrsim$0.25, and there exists a sharp drop off in probability at this point.

I integrated over κ at each value of η and plotted the marginalized likelihood function in Figure 4.6. Also plotted in the same figure is the original likelihood function where I did not consider the effects of a $\sin i$ cutoff. I found that there is a slight shift in the likelihood function to smaller values of radius inflation, however

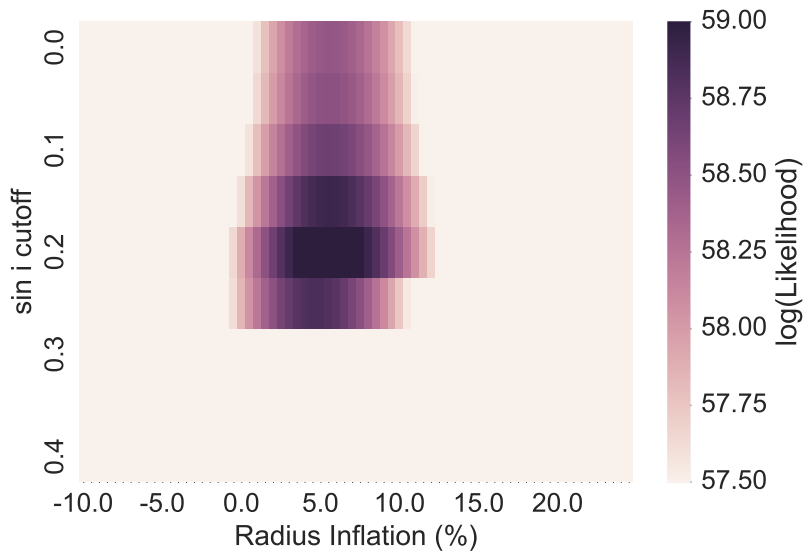

Fig. 4.5: Likelihood functions for a range of $\sin i$ cutoff values. By looking at a single $\sin i$ cutoff row, it is clear that the likelihood function peaks around 5% inflation, consistent with my previous results. There is also a maximum probability at a $\sin i$ cutoff of 0.2, with a sharp drop-off after 0.25.

this shift is smaller than the resolution of the grid and significantly smaller than the error bars. Therefore, the effects from any $\sin i$ bias present in literature rotation periods are not significant and are not the cause of the measured radius inflation.

I performed the same analysis for the limb darkening coefficient as I did for the $\sin i$ cutoff value. According to Claret et al. (2012), my stellar sample covers a range of linear limb darkening coefficients from $\mu \sim 0.3 - 0.4$ for observations in K-band. I therefore calculated $v \sin i$ values for a range of linear limb darkening coefficients from 0.3 to 0.4 and integrated over the limb darkening coefficients to obtain a marginalized likelihood function. I was left with a likelihood function that depends only on the parameter of interest (η). I show the likelihood functions for different values of μ and the marginalized likelihood function in Figure 4.7.

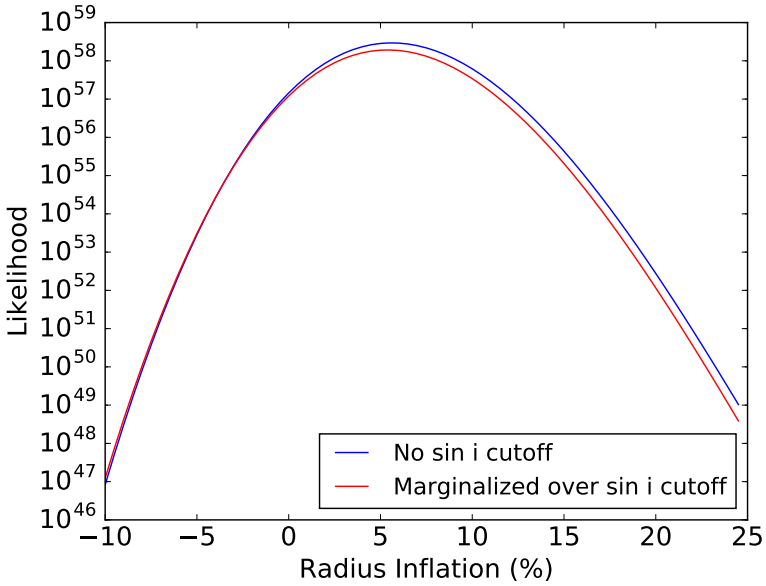

Fig. 4.6: Marginalized likelihood function (red) and original likelihood function (blue). The peak of the likelihood function is shifted slightly to lower radius inflation values for the marginalized likelihood function, however the shift is less than 0.5% (the resolution of our grid), and both functions peak at the same radius inflation value.

4.5 Results

Here, I performed the same steps of constructing a likelihood function but instead of using the radius values in Dittmann et al. (2014), I used other radius values and relations. The results of my Bayesian analysis for each method are shown in Figure 4.8. This figure shows that the least amount of discrepancy between the observed data and results is Benedict+Boyajian, which combines the most recent empirically derived mass and radius relations. All of the empirical relations show better agreement between the observed data and radius predictions than the radius predictions that utilize stellar evolutionary models.

To determine the statistical significance of whether an inflated model is preferred, I employed both the odds ratio and the Bayesian information criterion (BIC).

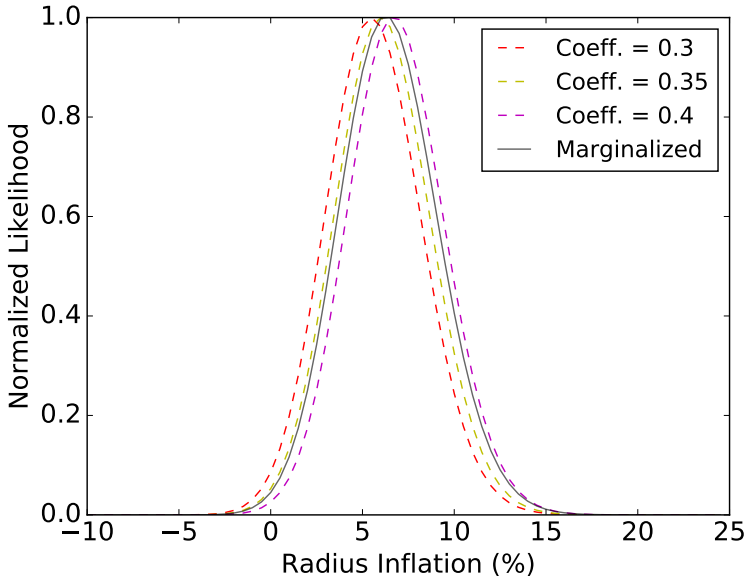

Fig. 4.7: The resulting likelihood functions using a linear limb darkening coefficient of 0.3 (red) and 0.35 (yellow) and 0.4 (magenta), and the likelihood function marginalized over the limb darkening coefficient (grey). By using a limb darkening coefficient at the top and bottom of the range set by my stellar sample, the peak likelihood is changed by $\sim 1\%$. This value is within the 1-sigma error bars for the likelihood function.

The odds ratio tests the relative probabilities of two theories and takes into account both likelihoods and priors. This serves to penalize theories that are more complex and explore more parameter space, however it can be a problem if the prior is not well defined, since different priors can significantly change the odds ratio. As stated previously I used a uniform prior since I did not have much specific prior information on inflation. In this case, the odds ratio is equal to the Bayes factor (B_{10}). The BIC on the other hand is an *approximation* of the log of the Bayes factor, but does not require a prior. It still penalizes complex theories, however, by taking into account the number of free parameters.

I used the equation for the Bayes factor derived in Eq. 3.24 of Gregory (2005):

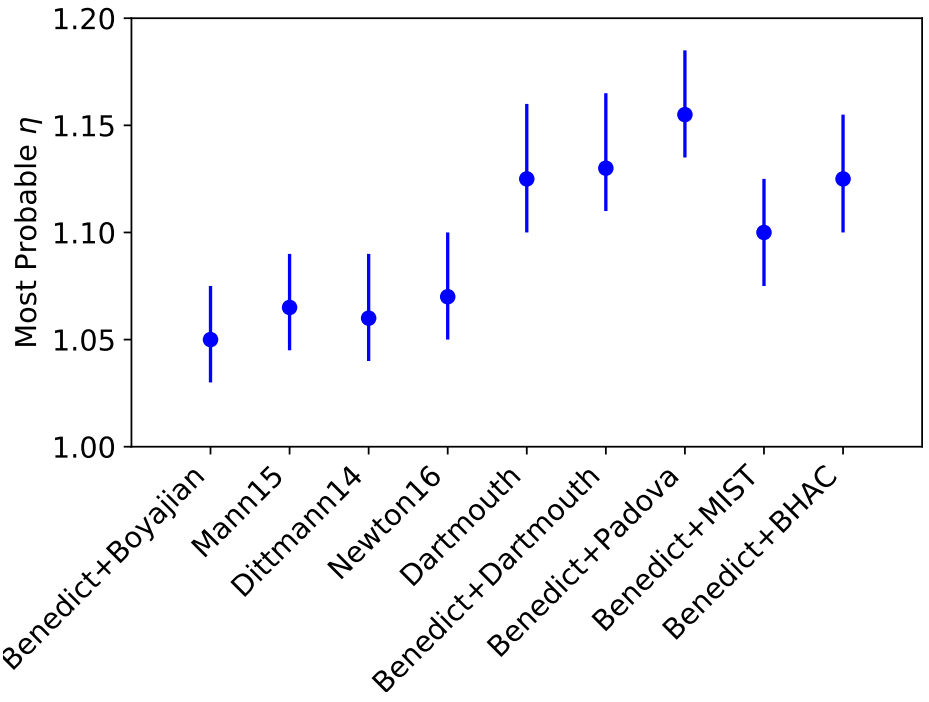

Fig. 4.8: Results from the marginalized likelihood PDFs for the different radius estimates in Table 4.2. The central blue point for each method denotes where the peak of the likelihood function falls. The error bars are one sigma error bars and show where 68% of the combined probability lies. All of the methods that use empirical relations instead of stellar evolutionary models show significantly lower levels of discrepancy between the data and the predicted radius values.

$$B_{10} \approx \frac{L(\hat{\eta})\delta\eta}{L(\eta_0)\Delta\eta}, \tag{4.13}$$

where η is the free parameter (the inflation percent in this case), $L(\hat{\eta})$ is the likelihood at the maximum inflation, $L(\eta_0)$ is the likelihood at 0% inflation, $\delta\eta$ is the RMS about the maximum inflation of the likelihood function, and $\Delta\eta$ is the width of the uniform prior. I tried two different priors. For prior 1, I chose the radius inflation range to be between 0 and 15% since these are the results often quoted from EBs (e.g., Torres & Ribas 2002). For the second prior I used the entire explored range of parameter space (from -10% to 25%, where the negative sign denotes a deflated radius).

Table 4.3. Significance of radius inflation

Method Name	Radius Under-prediction (%)	Odds Ratio (Prior 1)	P-value (Prior 1)	Odds Ratio (Prior 2)	P-value (Prior 2)	ΔBIC	Statement of Significance
Benedict+Boyajian	$5^{+2.5}_{-2}$	0.991	-	0.431	-	-0.424	No evidence of inflation
Mann15	$6.5^{+2.5}_{-2}$	3.33	0.032	1.45	0.12	0.788	Positive evidence of inflation
Dittmann14	6^{+3}_{-2}	2.966	0.038	1.290	0.15	0.567	Positive evidence of inflation
Newton16	7^{+3}_{-2}	8.882	0.009	3.862	0.026	1.663	Positive evidence of inflation
Dartmouth	$12.5^{+3.5}_{-2.5}$	2.9×10^3	1.11×10^{-5}	1.27×10^3	2.76×10^{-5}	7.276	Strong evidence of inflation
Benedict+Dartmouth	$13_{-2.5}^{+3}$	8.37×10^4	2.92×10^{-7}	3.64×10^4	7.14×10^{-7}	10.72	Very Strong evidence of inflation
Benedict+Padova	16.5^{+3}_{-2}	1.48×10^7	1.21×10^{-9}	6.45×10^6	2.9×10^{-9}	16.0	Very Strong evidence of inflation
Benedict+MIST	10^{+3}_{-2}	240.8	1.76×10^{-4}	104.7	4.57×10^{-4}	4.96	Strong evidence of inflation
Benedict+BHAC	12.5^{+3}_{-2}	1.97×10^4	1.38×10^{-6}	8.57×10^3	3.41×10^{-6}	9.27	Strong evidence of inflation

To calculate the BIC I used the Schwarz criterion as stated in Kass & Raftery (1995):

$$BIC = -2 \times ln(L(\eta)) + k \times ln(N), \tag{4.14}$$

where k is the number of free parameters (one for the model with inflation and zero for the model with a fixed inflation of 0%) and N is the sample size. I then calculated the BIC for both $L(\hat{\eta})$ and $L(\eta_0)$ and subtracted them to obtain ΔBIC. As stated in Kass & Raftery (1995), ΔBIC is approximately equal to two times log_e of the Bayes factor. Kass & Raftery (1995) also provide a detailed analysis of the way in which both the Bayes factor and the BIC translate to statements of statistical significance.

Finally, to allow for easier interpretation of the results, I translated our Bayes factors into frequentist p-values using the equation $B_{ij} = -(e\ p\ ln(p))^{-1}$, where p is the p-value and $p < e$ (Sellke et al. 2001). The results are summarized in Table 4.3. I found that all three predictions that involve stellar evolutionary models show 'Strong' to 'Very Strong' evidence that the observed M dwarf stars are larger than model radius estimates. The radii reported in both Newton et al. (2016) and Dittmann et al. (2014) show 2- to 3-σ levels of discrepancy between the quoted radii and the measured radii (where the measured radii are on average $6-7$% larger than reported radii). However, when I used the newest empirical relations from Benedict et al. (2016) and Boyajian et al. (2012) I found that neither the odds ratios nor the BIC can rule out the null hypothesis (i.e., that there is no inflation). Even though the maximum likelihood occurs for radii 5% larger than the relations predict, the increase in total probability is insufficient to overcome the penalty imposed by adding a free parameter.

4.6 Potential Biases

To ensure that my results are accurate and that there was no bias in the sample, I explored all of the possibilities I imagined where this could occur.

4.6.1 Differential Rotation

Because spots are primarily located at high latitudes on M dwarf stars (Barnes et al. 2015), and $v \sin i$ measurements are primarily sensitive to equatorial rotation, any discrepancies between the measured $v \sin i$ values and spot modulation periods could be due to differential rotation. However, both observations and models of differential rotation on low-mass, rapidly rotating stars yield extremely small shear values which cannot account for the discrepancies that I found. Using *Kepler* data of more than 10,000 stars, Reinhold & Gizon (2015) showed that there is a relationship between the horizontal rotation shear and the rotation period, where stars with faster rotation periods exhibited smaller shears. Reinhold & Gizon (2015) also found that stars categorized as having the most stable rotation period (deviations less than 0.001 days) all had periods of less than 10 days, and the distribution peaked at periods less than 1 day. This same result has also been found previously with smaller data sets (e.g., Hall 1991; Donahue et al. 1996).

A relationship between differential rotation and effective temperature was found by Barnes et al. (2005), where stars with cooler effective temperatures were found to have less differential rotation. Models of differential rotation provide further evidence that the shear decreases with increasing rotation period and decreasing mass (Küker & Rüdiger 2011). Therefore my sample of low-mass rapidly rotating stars should have little, if any, differential rotation since I am exploring the parameter space that is least affected by rotational shears. In Figure 4.9 I show the relation from Reinhold

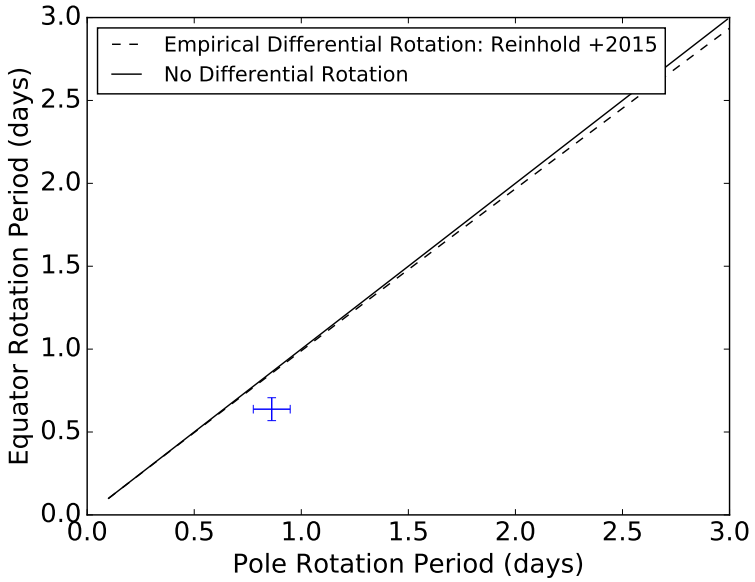

Fig. 4.9: The polar rotation period (minimum rotation period) determined through spot modulation and reported in Newton et al. (2016) versus the equatorial rotation period (maximum rotation period) determined through our $v \sin i$ measurements. The solid line, where both periods are the same, is the expected result for no differential rotation. The dotted line shows the relation from Reinhold & Gizon (2015). The empirical relation from Küker & Rüdiger (2011) has even smaller deviations from the line showing no differential rotation, therefore I do not display it on this plot. A target with a large deviation between the rotational and $v \sin i$ period is shown in blue, with observed errors. To calculate an equivalent period from the measured $v \sin i$ I assumed $\sin i = 90°$, which gave the largest equivalent period (i.e., minimizes the difference between the two periods). I can conclude that differential rotation cannot account for the observed discrepancy.

& Gizon (2015) to illustrate that differential rotation cannot account for the larger rotational broadening values compared to rotational periods.

4.6.2 Isochrone Age and Metallicity

Since the stars in my sample are rapid rotators and are magnetically active, they are also likely to be young. There is evidence that M dwarf stars do not follow an exact Skumanich-like relation between rotation period and age (Skumanich 1972). Rather, instead a rotation period dichotomy exists for these objects (Newton et al.

2016). West et al. (2008) found that, up to an age of 5−7 Gyr, fully convective M dwarf stars can continue to be magnetically active and retain rotation periods of less than 10 days. After an age of $5 - 7$ Gyr, it appears that these objects shed angular momentum and they rapidly migrate to rotational periods that are greater than ∼30 days (Newton et al. 2016). This makes precise gyrochonology difficult for these stars. However, for M dwarfs it is well established that rapid rotators are on average younger than are slow rotators (West et al. 2008, 2015). I therefore did not explore the use of isochrones with ages greater than 5 Gyrs.

I explored a number of scenarios with isochrones of younger ages. Using a 1 Gyr isochrone from the Dartmouth models, I found almost the same likelihood function, however with a 0.5% increase to even higher levels of inflation. Both the MIST and BHAC models offer isochrone grids down to ages of a few million years. I found changes of less than 1% in the most likely inflation at an age of 500 Myrs for both sets of models. At 250 Myrs, the MIST models return an η of 4.5%, which is no longer statistically significant. Performing the same analysis for the BHAC models, I found that at 200 Myrs I still measured an η value of 9%, and it was not until 120 Myrs that I no longer measured a statistically significant value of η. It is highly unlikely that all of the stars in the sample are this young since none of the stars are associated with star clusters or moving groups, and parallax measurements from Dittmann et al. (2014) indicate that the stars are located on the main-sequence. Further evidence that age is not the sole contributing factor of the observed inflation comes from comparison with rotation periods that are seen in young clusters such as the Pleiades and NGC 2516. For mid-to-late M dwarfs, neither of these young ($\sim 120-150$ Myrs) clusters are observed to contain stars with rotation periods longer than about 1.5 to 2 days (Scholz et al. 2011; Rebull et al. 2016a,b), however many of the stars in my sample that have the largest observed mismatch between the rotation

period and the rotational broadening have rotation periods in the $1-5$ day period regime and are therefore probably older than 150 Myrs. It is possible that some of the stars have ages of $200-300$ Myrs since they would be almost indistinguishable from main-sequence stars and some of the measured inflation could be due to age. This would not, however, explain the similarity between the $R\sin i$ distribution and radii from interferometry, which are measured on older, slowly rotating stars. Therefore, the majority of the observed inflation is not due to age.

In a study of the metallicity of the MEarth sample, Newton et al. (2014) found the average metallicity of the rapidly rotating stars to be 0.14 ± 0.1 dex. Therefore, in my analysis I adopted a metallicity of 0.14 dex when comparing to isochrones. I found that, by using a solar metallicity isochrone, the average inflation changed by $1-1.5\%$. Since this change in metallicity is more than one standard deviation and it can only account for a small amount of the observed inflation, I conclude that metallicity alone cannot be responsible for the inflation I find in my sample.

4.6.3 Microturbulence

Microturbulence is another mechanism by which the spectra of stars can be broadened, and some of the broadening I measured could be due to microturbulence rather than rotational broadening. This would not be a problem if microturbulence affected the spectra of the slowly rotating templates and the rapid rotators to the same degree. However, microturbulence could potentially affect the spectra of the young rapid rotators to a greater degree. I performed a simple order of magnitude test to determine the degree to which microturblence would be required to relieve the $5-6\%$ discrepancy between empirical relations and our $R\sin i$ measurements. For a simple order of magnitude estimate, I assumed that microturbulence and rotational broadening added in quadrature. I then estimated that the total broadening (v_{tot}) is related to the broadening from microturblence and rotation as follows: $v_{tot} =$

$\sqrt{v_{rot}^2 + v_{micro}^2}$. I found that in order to negate a 5% offset between data and empirical relations or models, microturblence needed to contribute 4 km/s of broadening. Since microturbulence is estimated to contribute $1-2$ km/s of broadening to low-mass stars (Reid & Hawley 2005), it is unlikely that the entire offset between empirical relations and my measured $R \sin i$ values is due to microturbulence. However, a $1-2$ km/s of broadening could account for about $0.5-1.5\%$ of the discrepancy between the radius prediction methods and the data, and the true values of η for each method (see Figure 4.8) could be about 0.005-0.015 smaller.

4.7 Discussion

I found that stellar evolutionary models under-predict the radii of low-mass stars by between 10 and 16.5% depending on the model, and that including radius inflation is strongly favored over model predictions that lack radius inflation. This is higher than the average inflation seen in EB systems ($\sim 5\%$ from a literature compilation in Han et al. 2017), so I tested whether this inflation was consistent over the whole mass range. I split the data into two mass bins containing a roughly equal number of targets, one with stars with masses in the range $0.08 M_{\rm Sun} < M < 0.18 M_{\rm Sun}$ and the second with stars with masses in the range $0.18 M_{\rm Sun} < M < 0.4 M_{\rm Sun}$. I then computed separate likelihood functions for each of these, results of which are shown in Figure 4.10. Compared to different stellar evolution models, I found that the higher mass bin had an average radius inflation of $5-7^{+4.5}_{-3.5}\%$, which is consistent with results from EBs. In the lower mass bin, I found that the average inflation was $13-17.5^{+4}_{-3}\%$ depending on the model used. In this low mass range there are few known EBs and only two stars with long baseline optical interferometry measurements with which to calibrate models.

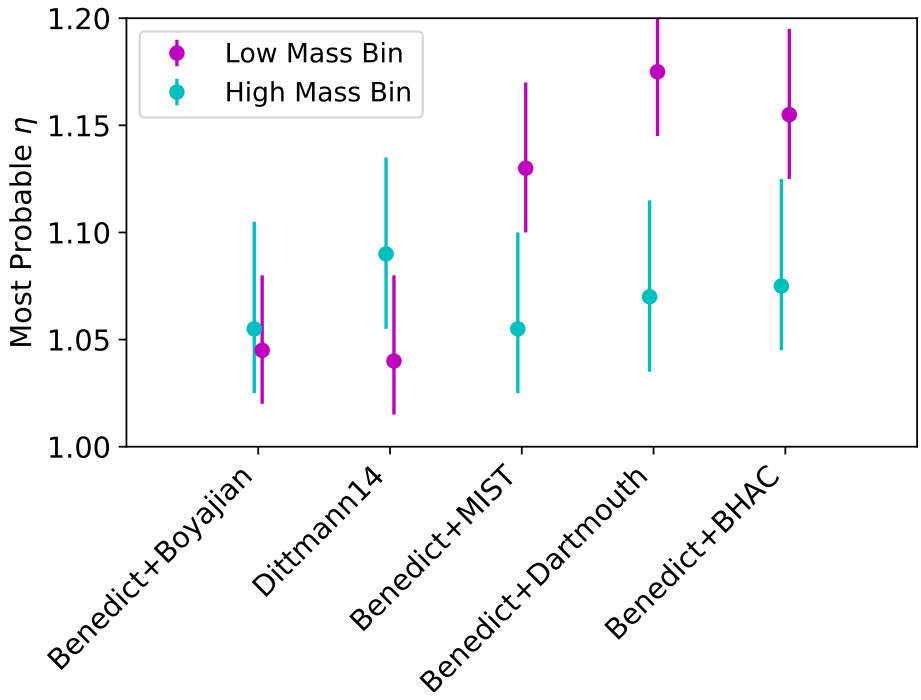

Fig. 4.10: Same as Figure 4.8, but with the stellar sample split into two similarly sized mass bins. The lower mass bin contains stars with $0.08M_{\rm Sun} < M < 0.18M_{\rm Sun}$, while the higher mass bin contains stars with $0.18M_{\rm Sun} < M < 0.4M_{\rm Sun}$. I find that the lower mass stars are significantly more inflated than the higher mass stars when compared to models. The lower mass stars are inflated by $13^{+4}_{-3}\%$ compared to the MIST models and $17.5^{+3.5}_{-3}\%$ compared to the Dartmouth models, and $15.5^{+4}_{-3}\%$ compared to the BHAC models. The higher mass stars are only inflated by $5.5^{+4.5}_{-3}\%$ compared to MIST models, $7^{+4.5}_{-3.5}\%$ compared to the Dartmouth models, and $7.5^{+5}_{-3}\%$ compared to the BHAC models. The empirical relations do not show the same trend that the lower mass stars are more inflated than the higher mass stars and for both empirical relations the points are within one standard deviation of each other.

The radius inflation I find for the higher mass bin is consistent with that found for in partially convective EBs, so I conclude that radius inflation is not a symptom of binarity (or the way in which parameters are extracted from EBs). I also find that there is no significant change in the amount of inflation compared to models across the fully convective boundary, and that the higher mass bin shows similar levels of inflation as to partially convective stars. However, for stars at the very end of

the main sequence, stellar evolutionary models severely underestimate stellar radii. While this could be an issue of age (i.e., the lowest mass stars may not have evolved onto the main sequence yet and are therefore still contracting), it is also possible that models of the lowest-mass stars are inaccurate. More work is needed to validate this result and determine why stellar evolutionary models underestimate the radii of the lowest mass stars by $15 - 20\%$.

Since partially convective and fully convective stars are inflated by similar amounts, this can be used to provide constraints on models. It is unclear whether strong magnetic fields can inhibit convection and inflate radii in fully convective stars to the $\sim$10% seen here and in EBs. For example, MacDonald & Mullan (2017) state that they can produce radius inflation at the $\sim 10\%$ level by modeling the stabilization of convection with magnetic fields on the order or 10 kG. Feiden & Chaboyer (2014) argue that if they use a similar method to **?**, they require unreasonably large magnetic fields to inflate the radii by even 5%. The data I present here are consistent with the results from MacDonald & Mullan (2017), but in the scenario put forth by Feiden & Chaboyer (2014), magnetic spots would be required to produce the observed inflation in fully convective stars. More exploration of spot modeling would increase our understanding of the problem and help distinguish between the two modeling frameworks.

Radii reported in Newton et al. (2016) and Dittmann et al. (2014), and radii calculated using the relations in Mann et al. (2015) under-predict the radii of the stars in my sample by $6-7\%$, but only with a moderate level of statistical significance ($2 - 3\sigma$). When I used the most recent empirical $M_{K_s}-$Mass relation (Benedict et al. 2016) and Mass$-$Radius relation (Boyajian et al. 2012), I found no statistically significant evidence that a model with inflation describes the data better than a model without inflation. The Mass$-$Radius relation I used to determine these radii

was calibrated using slowly rotating stars. Using this relationship on my rapidly rotating sample returns statistically consistent results, leading me to conclude that if rotation inflates the radii of fully convective rapidly rotating stars, it does so by less than $5^{+2.5}_{-2}$%.

Further evidence that rotation does not significantly affect the radii is given by the fact that slowly and rapidly rotating stars are inflated by similar amounts compared to models. I calculated updated mass estimates for Proxima Centauri and Barnard's Star using K_s-band magnitudes and distances reported in Boyajian et al. (2012), and applying the $M_{K_s}-$Mass relation from Benedict et al. (2016). I then used a relation from the Dartmouth code for solar metallicity and ages of 5 Gyrs and 10 Gyrs for Proxima Centauri and Barnard's Star, and found models underestimated the radii for both stars by 3-4% compared to the optical interferometry radius measurements from Boyajian et al. (2012). Further evidence of slowly rotating mid-to-late M dwarf stars with inflated radii was noted by Irwin et al. (2011), who measured the radii of a long period (41 day orbital period) EB, and found the component radii to be inflated by 4%. My bin of higher mass stars is inflated by an average of between 5 and 7%, depending on the model used, which is consistent with $3-5$% radius inflation of slowly rotating stars.

4.8 Summary

Magnetically active, rapidly rotating, fully convective M dwarf stars are on average $10-16$% larger than predictions from stellar evolutionary models. When the sample is broken up into two mass bins, however, the lowest mass M dwarfs are $15-17$% larger than models, while the larger mass bin is only $5-7$% larger than models. The $5-7$% radius inflation is consistent with previously published results from EBs and LBOI. I find that the larger radii of the lowest-mass is not completely due to

their young age because to mitigate any discrepancy with age effects the stars would have to be significantly younger than expected. Finally, by comparing to empirical relations I conclude that the Benedict et al. (2016) and Boyajian et al. (2012) relations are accurate (to an uncertainty of $\sim 5\%$) for rapidly rotating, magnetically active, fully-convective M dwarf stars. These relations had not been thoroughly tested at the very low-mass end of the main sequence until now. Boyajian et al. (2012) explicitly warned that their relations may not be accurate for spectral types later than M4. My work therefore provides evidence that the relations hold to within uncertainties of $\sim 5\%$, even at the end of the main sequence ($M \sim 0.08 M_{\rm Sun}$) for the most rapidly rotating and magnetically active stars.

Chapter 5

Can Starspots Explain Magnetic Stellar Inflation?

5.1 Introduction

Magnetic spots are cool regions of suppressed flux and enhanced magnetic fields on the surface of the Sun and other stars. Spots have been directly detected on the Sun for hundreds of years, and more recently they have been detected on the surfaces of other stars (e.g., Monnier et al. 2007). If the surface of a star is spotted, spots rotate in and out of view as the star rotates, and a periodic change in brightness will occur. Periodic rotational modulation has been measured in thousands of M dwarfs, demonstrating the spotted nature of these stars (McQuillan et al. 2013; Newton et al. 2016). The fact that M dwarf stars are spotted is unsurprising given the fact that they host strong magnetic fields (see Section 1.3.3), and starspots are a manifestation of concentrated magnetic energy.

Determining precise spot temperatures, spot covering fractions, and spot configurations on M dwarf surfaces is significantly more complicated than solely deducing their presence. Some insight into spot properties can be gained by analyzing the vast light curve data sets that show rotational modulation of M dwarf stars. Jackson & Jeffries (2013) analyzed Kepler light curves and predicted the sizes and distributions of spots on the surfaces of M dwarfs. Newton et al. (2017) found a relation between Hα equivalent width and the semi-amplitude of rotational modulation of mid-to-late

M dwarf stars. They found that as the Hα equivalent width became more negative (more emission and hence more magnetically active), the semi-amplitude of rotational modulation increases. That is, as the stars become more magnetically active, they have higher spot covering fractions and show more rotational modulation. Newton et al. (2017) found that this relation held true for all but the most active stars, where the relation reversed, and an increase in magnetic activity lead to smaller semi-amplitudes of rotational modulation. Newton et al. (2017) interpreted this as evidence that the most magnetically active stars have spot covering fractions $\geq 50\%$. Single light curves can also be analyzed in more depth by using computationally intensive programs to gain insight into spot parameters, instead of analyzing vast sets of light curves with simple diagnostic statistics (e.g., Davenport et al. 2015; Morris et al. 2018).

Vogt (1979, 1980) and Ramsey & Nations (1980) were the first to use spectral features to infer starspot properties on the surfaces of solar-type stars. Since the stars in the studies were solar-type stars, absorption from molecules should not have been present in the spectra due to the fact that molecules can only form in the atmospheres of stars with surface temperatures below $\sim$4000 K. Nevertheless, TiO was detected in absorption in the spectra of many Sun-like stars, which was attributed to the presence of a cooler spot spectrum.

This technique has been used more recently to estimate spot covering fractions for hundreds of G, K, and early-type M dwarfs in the Pleiades cluster (Fang et al. 2016). Fang et al. (2016) concluded that active M dwarf stars have spot covering fractions of $40 - 50\%$. Fang et al. (2016) also found evidence for spot temperatures that were about 500 K less than the quiescent photosphere temperatures on early-type M dwarf stars. Unfortunately, this technique becomes impossible for mid-to-late

M dwarf stars because TiO already dominates their spectra, making it difficult to constrain spot parameters by using its strength.

Gully-Santiago et al. (2017) used an approach similar to the TiO method to measure spectral signatures from a cool spot or cool spots on the surface of a T Tauri star. However, instead of simply using the TiO band, they used the entire H and K spectral bands and modeled the spectrum as a combination of a hot photosphere and a cool spot. Because this technique uses large regions of wavelength space, it has higher potential to be applicable to later-type M dwarf stars since it does not rely on a single molecular band such as TiO, which becomes saturated for cooler M dwarfs.

Finally, Barnes et al. (2015) used a new spectral analysis technique and published starspot properties for an M5 dwarf and an M9 dwarf. Using a spectral resolution of $\sim$90,000 Barnes et al. (2015) reconstructed Doppler imaging maps from small radial velocity jitters produced by starspots on the surfaces of these two fully convective M dwarf stars. Their study found that the best fit spot temperatures were of order 200 to 300 K less than the best fit photosphere temperatures.

In Chapter 4, I showed that rapidly rotating, magnetically active, fully convective M dwarf stars are on average $10 - 16\%$ larger than model determination. As discussed in Section 1.6.2, Chabrier et al. (2007) predicted that spots are the primary mechanism that can inflate the radii of fully convective stars, because decreasing the mixing length parameter has little to no effect on their radii. In this chapter I will show how I determined a spot temperature and spot covering fraction for a single rapidly rotating, magnetically active, fully convective M dwarf, using an approach similar to that of Gully-Santiago et al. (2017). I then compared the measured spot temperature and spot covering fraction to model predictions of the temperature to determine whether the radius discrepancy could be solely attributed

to spots or whether another mechanism of radius inflation was necessary to resolve the observed radius inflation.

5.2 Target Selection

I performed the starspot analysis on a single star, 2MASS J23270216+2710367. In the future I plan to extend this work to multiple stars, but that is not within the scope of this dissertation. The target was selected from my sample of fully convective rapidly rotating M dwarfs in Chapter 4. The data used in this Chapter are the same as the data used in Chapter 4; i.e., high resolution H- and K-band spectra taken with the IGRINS instrument on the Discovery Channel Telescope. For more information about the observation and data reduction technique, see Section 4.3.1.

Since this initial analysis was to be performed on only a single star, I chose a star that represented the best case scenario for spot detection: the highest spot covering fraction and the highest spot to photosphere temperature contrast. All of the stars in my sample had clearly detected rotation periods and, so, they are *all* spotted to some extent since a rotation period can only be detected as spots rotate into and out of view. However, to choose a star with a high spot covering fraction, I limited my selection to the most magnetically active stars, since Newton et al. (2017) demonstrated that magnetic activity and spot covering fractions were directly correlated. Newton et al. (2017) measured Hα equivalent widths for a large portion of the MEarth sample, so I selected only targets that had Hα equivalent width measurements less than -6 Å, which represented the most magnetically active $\sim$ 10% of all the stars from my sample. Fang et al. (2016) measured a trend in spot to photosphere temperature contrast, where the higher the photosphere temperature the larger the spot to photosphere temperature contrast. Although this relation was mostly for G- and K-type stars, as an initial guess I assumed this was the case for M dwarfs as well.

I therefore selected the star with the highest estimated mass (while still being below the fully convective limit of $\sim 0.35\ M_{\rm Sun}$) that satisfied the Hα equivalent width cut. The star meeting these criteria was 2MASS J23270216+2710367.

5.3 Properties of 2MASS J23270216+2710367

5.3.1 Empirically Derived Parameters

2MASS J23270216+2710367 was classified as an M5 dwarf with a metallicity of 0.11 ± 0.1 by Newton et al. (2014). Newton et al. (2016) measured a rotation period of 0.922 days, and Newton et al. (2017) measured an Hα equivalent width of -8.63 Å and a radial velocity of -4 ± 4 km/s. I measured a rotational broadening ($v \sin i$) of 13 $\pm$0.5 km/s for this object (Kesseli et al. 2018). Using the 2MASS K_s-band magnitude of 9.421 and the Gaia distance of 33.465 pc (Bailer-Jones et al. 2018), I calculated an absolute K_s-band magnitude of 6.798. I used the M_{K_s}–Radius relation I obtained in Chapter 3 (Equation 3.7) and the calculated metallicity to derive a radius of 0.334 $R_{\rm Sun}$. I used the M_{K_s}–Mass relation from Benedict et al. (2016) to calculate a mass of 0.34 $M_{\rm Sun}$. Finally, using Equation 4.1, I estimated the inclination to be 57° (where 0° is parallel to the rotation axis).

I was also able to obtain information on the $T_{\rm eff}$ of 2MASS J23270216+271036 from a previously published value in the literature and by using a new empirical color-to-effective temperature relation. Newton et al. (2015) used equivalent widths of temperature sensitive features in the H-band to estimate a temperature of 3251 ± 86 K for 2MASS J23270216+2710367. Mann et al. (2015) found that a $V - J$ color relation, which included a metallicity dependence, could predict the $T_{\rm eff}$ with an uncertainty of only 43 K. I used this relation to estimate a $T_{\rm eff}$ of 3216.4 ± 43 K for 2MASS J23270216+2710367. It is important to note that while previous studies have been able to derive an estimate of $T_{\rm eff}$, they could not distinguish between a spot

temperature and a photosphere temperature, reporting only a single temperature for the star. With only a single temperature reported for the star and no spot covering fraction, it is impossible to distinguish between global inhibition of convection and local inhibition of convection through spots.

5.3.2 Parameters Estimated from Stellar Evolution Models

I determined the $T_{\rm eff}$ values that different stellar evolution models predicted so that I would be able to compare the model $T_{\rm eff}$ values to the $T_{\rm eff}$ values that I measured. I first calculated the bolometric luminosity of 2MASS J23270216+2710367 and then used models to estimate the effective temperature for the given bolometric luminosity. It is vital to use the bolometric luminosity to calculate the model temperature because to solve for the radius inflation ($R_{\rm model}/R_{\rm true}$) using the temperature I will infer later in this chapter ($T_{\rm true}$), the bolometric luminosity input into the model ($L_{\rm model}$) and the observed bolometric luminosity ($L_{\rm true}$) need to be the same.

$$\frac{L_{\rm model}}{L_{\rm true}} = \frac{4\pi\ R_{\rm model}^2\ \sigma\ T_{\rm model}^4}{4\pi\ R_{\rm true}^2\ \sigma\ T_{\rm true}^4} = 1 \tag{5.1}$$

To calculate the bolometric luminosity I used the method I presented in Section 3.5. Table 5.1 lists all the photometry that I collected to generate an SED. I used the same quality cuts as in Section 3.5, which lead me to exclude all but the g-band of Pan-STARRS1 due to saturation and the WISE W4 band due to a low SNR. I then converted all the magnitudes to fluxes. I tested both integrating directly over the photometry points, as well as integrating over a BT-SETTL model spectrum that was anchored to the photometry points. I tested BT-SETTL models with a range of effective temperatures and metallicities, and I found that changing the model did not significantly change the calculated bolometric luminosity. Table 5.3 shows the

Table 5.1. Photometry of 2MASS J23270216+2710367

band	Central Wavelength (μm)	Magnitude	Uncertainty
SDSS u	0.35	18.134	0.016
SDSS g	0.48	15.657	0.004
Pan-STARRS1 g	0.481	15.4266	0.0047
Gaia B	0.5044	15.0443	0.0037
SDSS r	0.62	14.124	0.003
SDSS i	0.76	12.823	0.000
Gaia R	0.7692	12.0789	0.0019
SDSS z	0.91	11.747	0.004
2MASS J	1.235	10.274	0.021
2MASS H	1.662	9.705	0.022
2MASS K	2.159	9.421	0.018
WISE 1	3.35	9.262	0.022
WISE 2	4.60	9.066	0.019
WISE 3	11.56	8.873	0.027

different bolometric luminosities I calculated for 2MASS J23270216+2710367 using the slightly different methods.

Next, I used the different bolometric luminosities to estimate model effective temperatures. I generated isochrones from the Mesa Isochrones and Stellar Tracks (MIST v1.2; Choi et al. 2016) using the online web interpolator[1] and from the Dartmouth stellar evolution models using the online web tool[2] (Dotter et al. 2008). For both model grids I used a metallicity of 0.11 dex (Newton et al. 2014). Newton et al. (2016) determined constraints on MEarth star ages by analyzing the galactic velocity dispersion for different rotation period bins and found that stars with rotation periods less than a day had an average estimated age of $0.5^{+0.4}_{-0.2}$ Gyrs. However, this is solely an estimate for the population, and ages of individual low-mass stars are difficult to determine precisely. The MIST models allow for a wide range of age inputs, so I tested age values of 0.2, 0.5, 1, and 5 Gyrs. The Dartmouth models offer

[1] `http://waps.cfa.harvard.edu/MIST/interp_isos.html`
[2] `http://stellar.dartmouth.edu/models/isolf_new.html`

Table 5.2. Model Effective Temperatures

	$L_{\rm bol}$ ($\log L_{\rm Sun}$)	MIST $T_{\rm eff}$ (0.2 Gyr)	MIST $T_{\rm eff}$ (0.5 Gyr)	MIST $T_{\rm eff}$ (1.0 Gyr)	Dartmouth $T_{\rm eff}$ (1.0 Gyr)
$L_{\rm bol}$ simple	-1.8978	3383 K	3382 K	3378 K	3385 K
$L_{\rm bol}$ BT SETTL high temp.	-1.9697	3310 K	3327 K	3322 K	3362 K
$L_{\rm bol}$ BT SETTL low temp.	-1.9259	3354 K	3363 K	3360 K	3377 K

isochrones down to an age of 1 Gyr, so I only tested this single age isochrone for the Dartmouth models. Table 5.3 shows all the different derived effective temperatures from the models. All of the temperatures are within 65 K of each other and are consistent. For the rest of the analysis I used a model temperature of 3359 ± 25 K, which represents the mean of all the model temperatures with an uncertainty equal to the standard deviation between them.

5.4 Starspot Parameter Extraction

To derive starspot and photosphere temperatures, as well as spot filling fractions, I compared individual spectral orders of 2MASS J23270216+2710367 to a pre-computed grid of PHOENIX model atmospheres (Husser et al. 2013), which are available on the Göttingen Spectral Library Website[3]. The modeling process used the Starfish code presented in Czekala et al. (2015), which was modified to measure spot parameters by Gully-Santiago et al. (2017). In Section 5.4.1, I discuss the basics of the Starfish code, but for a more complete and in depth explanation the reader should refer to Czekala et al. (2015). In Section 5.4.2 I detail how this code has been modified by Gully-Santiago et al. (2017) to measure spot parameters. Finally, in Section 5.4.3 I explain my implementation of this code.

[3] `http://phoenix.astro.physik.uni-goettingen.de/?page_id=15`

5.4.1 Starfish

Starfish is a Bayesian modular framework that infers stellar properties from spectra. The stellar parameters are determined by forward modeling an observed spectrum using a pre-computed grid of synthetic model spectra. Since the grid is sparsely sampled in $T_{\rm eff}$, [Fe/H], and log g, but the observed spectrum can be any combination of these parameters, Czekala et al. (2015) developed a spectral "emulator" that smoothly interpolates over the model grid. A simple linear interpolation is insufficient, as Czekala et al. (2015) found that linear interpolation results in a posterior that is peaked at the model gridpoints, biasing the derived stellar properties. Instead, the emulator decomposes the model spectra into a set of eigenspectra using principal component analysis (PCA). Gaussian processes is then used to determine optimal weights associated with each eigenspectrum as a function of $T_{\rm eff}$, [Fe/H], and log g. A linear combination of the eigenspectra can then be used to reconstruct any arbitrary combination of the physical parameters necessary.

Along with the intrinsic physical parameters ($T_{\rm eff}$, [Fe/H], and log g), there are "extrinsic" parameters that also shape the spectrum, including the instrumental broadening profile, the rotational broadening of the star ($v \sin i$), the radial velocity of the star (v_r), the flux dilution (Ω), and any residual shape in the spectrum. The model is computed to return the flux at the stellar surface, but the observed star is some distance away and so the flux is diluted by $\Omega = (R/D)^2$, where R is the star's radius and D is the distance. To account for this effect, the model spectrum is simply multiplied by Ω. Before the new reconstructed model spectrum can be compared to the observed spectrum, the model is Doppler shifted to rest and convolved with the two broadening kernels: one for the instrumental broadening and one for the rotational broadening. Oftentimes there is a residual shape in the spectrum that is not physical and is left over from poor flat fielding, blaze correction or flux calibration.

This is taken into account by multiplying the model by a 3rd degree Chebyshev function. After this process, the model is sampled onto the same grid as the observed spectrum so the two can be compared directly.

The resulting model is compared pixel-by-pixel to the observed spectrum using a likelihood calculation, in which larger residuals are penalized, but covariances in the residual spectrum are allowed through an $N_{pix} \times N_{pix}$ covariance matrix. The covariance matrix characterizes measurement uncertainty and any correlated residuals using a global noise kernel. The residual structure can then be down-weighted in the likelihood calculation so as not to bias the final estimated parameter results. This process is repeated using a Markov Chain Monte Carlo (MCMC) simulation with a blocked Gibbs sampler, where $T_{\rm eff}$, log g, [Fe/H], $v \sin i$, v_r, and Ω are optimized, while the Chebyshev coefficients and noise parameterization coefficients are treated as nuisance parameters and marginalized over.

Since this is a Bayesian analysis, a prior can be specified for each parameter, and any known information about the star can be incorporated. I will discuss the priors I used to determine my best-fit parameters in Section 5.4.3.

5.4.2 Mix Model Implementation with Starfish

Gully-Santiago et al. (2017) altered Starfish to accommodate starspots by adding in a second model spectrum with a different $T_{\rm eff}$ and Ω, but identical values for all the other parameters (log g, [Fe/H], $v \sin i$, v_r, and Chebyshev coefficients). It is assumed that spots simply emit at some effective temperature ($T_{\rm spot}$) that is lower than the effective temperature of the photosphere ($T_{\rm phot}$). While a two component temperature model likely does not capture all of the complexities of a star's photosphere since faculae are not included, this simple model does capture the dominant behavior of flux suppression by starspots.

In the updated version of Starfish, the final composite model spectrum is a combination of the two model spectra, given by:

$$S_{\rm mix} = \Omega_{\rm spot} B(T_{\rm spot}) + \Omega_{\rm phot} B(T_{\rm phot}), \tag{5.2}$$

where $B(T)$ is the spectral radiance from the hot or cool model. $B(T)$ already accounts for the fact that a hotter model produces more flux than a cooler model. The spot covering fraction, β, can then be calculated using the flux dilution values, Ω:

$$\beta = \Omega_{\rm spot}/(\Omega_{\rm phot} + \Omega_{\rm spot}). \tag{5.3}$$

Gully-Santiago et al. (2017) also updated the MCMC process to include the two new free parameters and they switched the core sampling technique from a Gibbs sampler to an `emcee` ensemble sampler (Foreman-Mackey et al. 2013). The reason for the sampler switch was to account for the fact that the two new parameters made the MCMC sampling much more correlated than it had been previously, which necessitated that all the parameters be fit simultaneously.

Gully-Santiago et al. (2017) tested and validated this new framework on an early M-type T Tauri star, LkCa 4.

5.4.3 My Implementation and Parameter Extraction

I used the Gully-Santiago et al. (2017) updated Starfish code to estimate $T_{\rm spot}$, $T_{\rm phot}$, and β for 2MASS J23270216+2710367. As the first step in determining these parameters, I downloaded the grid of models for effective temperatures ranging from $2300-4000$ K, $\log g = 5.0$ and 5.5, and [Fe/H] $= -0.5$, 0.0, 0.5. The parameter range of the downloaded spectra greatly exceeded the actual range of expected values for

each parameter so the MCMC sampling could fully explore parameter space without hitting an edge of the grid.

I fitted each echelle order of the spectrum separately so that the process could be parallelized and computational the time reduced. I applied the Starfish spectral "emulator" to the grid of models in a wavelength range corresponding separately to each order. After this step, I was able to quickly create a reconstructed model spectrum of any IGRINS spectral order for any combination of log g, $T_{\rm eff}$, and [Fe/H].

Since 2MASS J23270216+2710367 has been thoroughly characterized already, and I was only interested in obtaining values for $T_{\rm spot}$, $T_{\rm phot}$, and β, I applied Gaussian priors or I fixed any parameters with values in the literature. I used the [Fe/H] value calculated by Newton et al. (2014) to fix the metallicity to 0.11 dex. Czekala et al. (2015) found that the residuals associated with small changes in log g were negligible compared to residuals introduced by model imperfections and recommended fixing log g for main sequence stars. Using the mass and radius of 2MASS J23270216+2710367, I estimated log g to be $\sim$5.0 dex, so I fixed it to that value. I added Gaussian priors for both $v \sin i$ and v_r from the values published in the literature (Kesseli et al. 2018; Newton et al. 2014). I used mean values of 13.0 and -4.0 and uncertainties of 0.5 and 4.0, for $v \sin i$ and v_r respectively. I did not fix these values because I found it useful to use $v \sin i$ and v_r as checks to ensure the code was working correctly.

I chose to apply few priors to the temperatures and flux scaling factors to avoid biasing the results in any way. However, I did specify that the spot temperature must be lower than the photosphere temperature.

To determine an initial starting point of the MCMC simulation for the temperatures, flux scaling factors (Ω), Chebyshev coefficients, and noise parameters, I compared data in a single order to reconstructed model spectra and hand-tuned these values to come up with an initial guess for each parameter. In a few orders I also

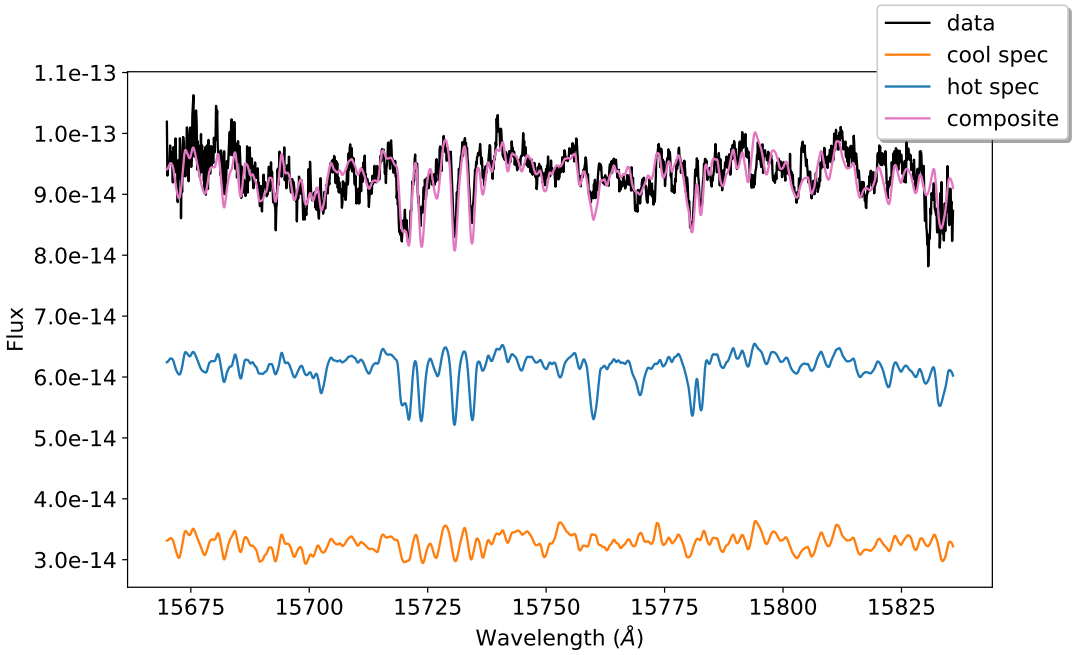

Fig. 5.1: The spectrum for a single IGRINS order (black) compared to the best-fit model spectrum (magenta). The best-fit spectrum is composed of a hot component (here about 3200 K; blue) and a cool component (here about 2600 K; orange). The component spectra have the same metallicity (fixed at 0.11 dex), log g (fixed at 5.0), radial velocity, and $v \sin i$. Many of the features seen in the hotter spectrum (blue) are clearly seen in the data, but these features are not as clearly defined as in the hot spectrum. By adding in the smaller and more continuous spectral features in the cooler spectrum (orange), the model fits the data much better.

checked that initializing the MCMC simulation to different starting values lead to a similar answer, and indeed found that initializing the parameters to different, yet still reasonable values, did not make a significant difference in the final parameter estimation.

5.5 Results

5.5.1 Starfish Output and Testing

The MCMC simulations were run separately in each order, allowing me to check orders individually and then to compare the orders to each other to ensure that

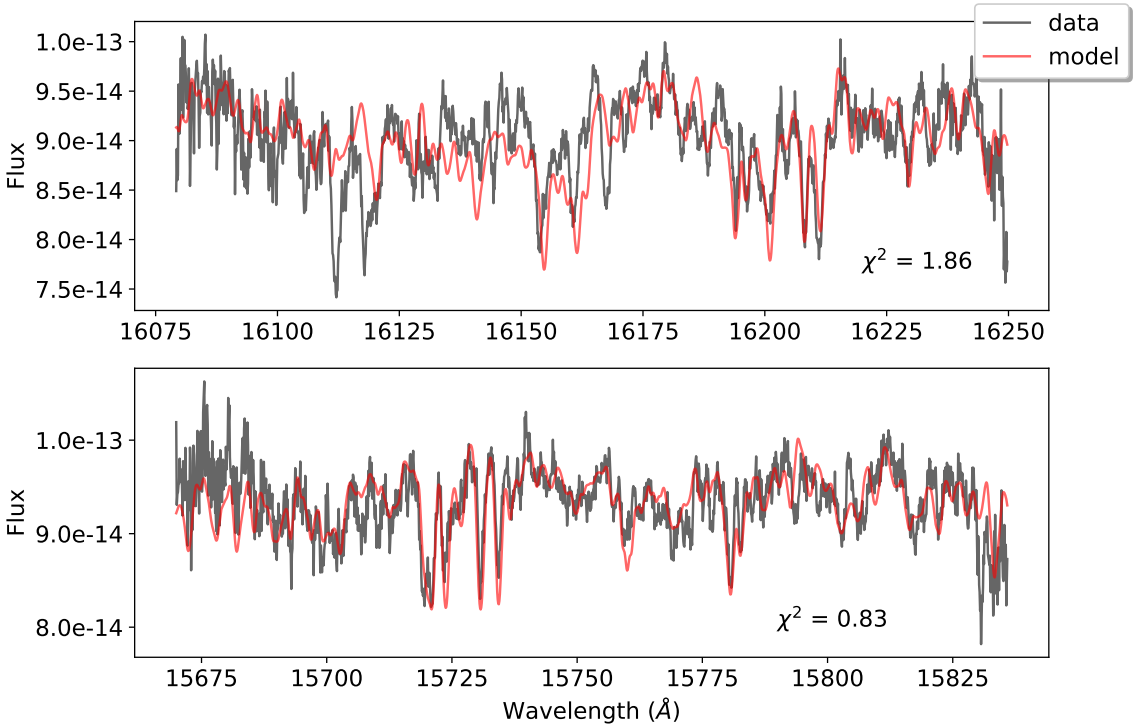

Fig. 5.2: On the bottom I show an example of an order with data (gray) that is well fit by the model (red), while on the top, the model cannot correctly reproduce the opacities and line strength present in this order. The poor performance of the model atmosphere at some wavelengths is a known problem, and while the models are state-of-the-art, they still have trouble correctly reproducing parts of the spectra of low-mass stars due to missing molecular opacities. The numbers listed are the reduced χ^2 values. I did not use orders with a reduced χ^2 value greater than 1.5.

different orders were producing consistent results. To check each order individually, I plotted the best-fit reconstructed spectra of the hot and cool components separately, along with the combined best-fit spectrum, and compared them to the data to be certain that the model and data were consistent (see Figure 5.3). This process was repeated and the best-fit reconstructed spectra were examined for each order. I found that in some orders there were many spectral features that the model could not reproduce, while in other orders the model successfully reproduced almost every

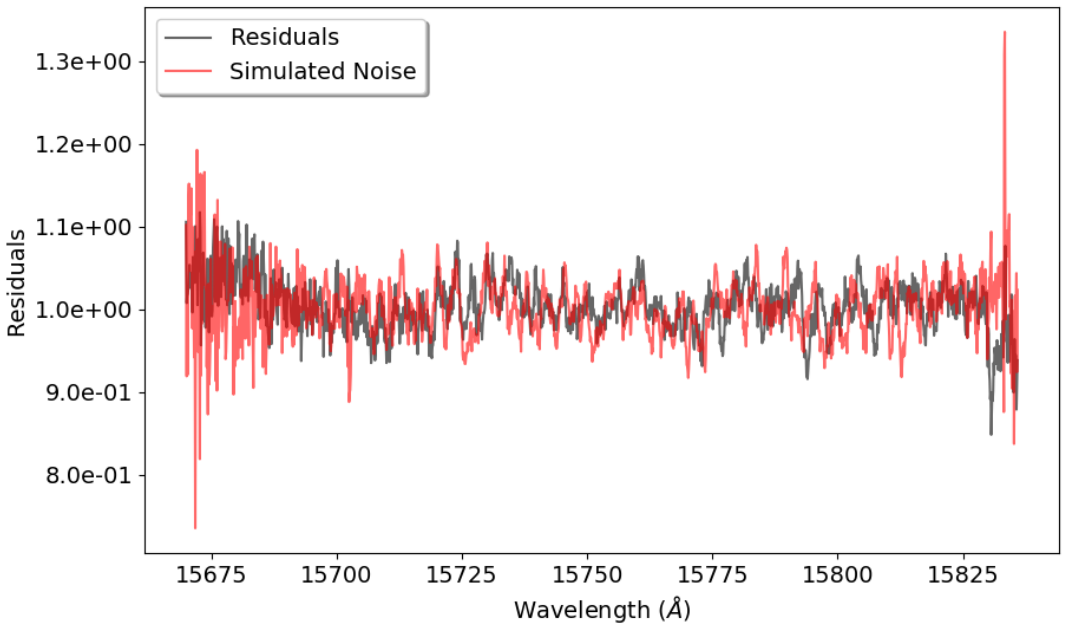

Fig. 5.3: Residual spectrum showing the data divided by the best fit model (gray) and the simulated noise set by the three noise parameters given in Starfish (red). The true residuals and the simulated residuals have a similar length scale for correlated residual noise, as well as a similar amplitude. Both also show larger amplitudes towards the edges of the order, as expected.

spectral feature. To remove orders with poor model agreement, I computed a reduced χ^2 statistic between the model and data to quantify the goodness of fit. Orders with a reduced χ^2 greater than 1.5 were not included in the rest of the spectral analysis, so that regions for which the model was inaccurate would not bias the results.

Along with checking the physical parameters, I also inspected the nuisance parameters. To ensure that the parameters used by Starfish to account for the noise and any correlated residuals in the spectrum were converging to reasonable values, I plotted a random draw of the reconstructed noise parameterization and the true residual (Figure 5.2). Figure 5.2 demonstrates that Starfish can accurately capture the noise and any correlated residuals that are present in the spectrum.

Table 5.3. Starfish Results by Echelle Order

Order Number	Central Wavelength (μm)	Reduced χ^2	$T_{\rm phot}$ (K)	$T_{\rm spot}$ (K)	β
9	1.688	1.03	3123^{+173}_{-152}	2715^{+127}_{-78}	49%
10	1.658	1.20	3737^{+185}_{-611}	2700^{+67}_{-80}	68%
11	1.643	1.50	3083^{+83}_{-98}	2736^{+106}_{-71}	39%
12	1.629	1.36	3135^{+66}_{-109}	2775^{+104}_{-70}	47%
13	1.614	1.86	2944^{+179}_{-69}	2813^{+73}_{-82}	47%
14	1.600	0.99	3140^{+108}_{-121}	2695^{+131}_{-58}	47%
15	1.587	1.95	3055^{+87}_{-61}	2762^{+157}_{-142}	22%
16	1.573	0.83	3259^{+147}_{-61}	2595^{+71}_{-108}	51%
17	1.560	0.64	3147^{+102}_{-94}	2866^{+237}_{-217}	37%
18	1.547	0.68	3086^{+152}_{-49}	2878^{+105}_{-206}	35%
19	1.534	0.88	3146^{+94}_{-62}	2890^{+114}_{-224}	41%
20	1.522	1.29	3227^{+305}_{-68}	2698^{+135}_{-77}	45%

I also constructed triangle plots for each order. The triangle plots show the results of the MCMC simulation for all of the physical free parameters, including both effective temperatures, both Ω values, the $v \sin i$ value, and the radial velocity. An example of a triangle plot for a single order is shown in Figure 5.4. The $v \sin i$ and v_r values were similar to what had previously been reported in all cases, lending confidence to my results. An interesting second peak in $T_{\rm phot}$, centered at $\sim$3750 K, can be clearly seen in Figure 5.4. This second temperature peak corresponds to a lower filling fraction, and a smaller second peak in $\log_{10}\Omega$ can also be easily distinguished. If this feature was only present in a single order, it would not be significant, but a similar second peak can be seen in five different orders (see Figure 5.5).

Figure 5.5 shows the results of all of the MCMC simulations for 12 different orders. Some of the orders show little overlap between the spot and the photosphere probability distributions (orders with the central wavelength of 1.688, 1.643, 1.6, 1.573, 1.522 μm), while others show varying degrees of overlapped distributions (orders with the central wavelengths of 1.534, 1.547, and 1.560). In orders that are

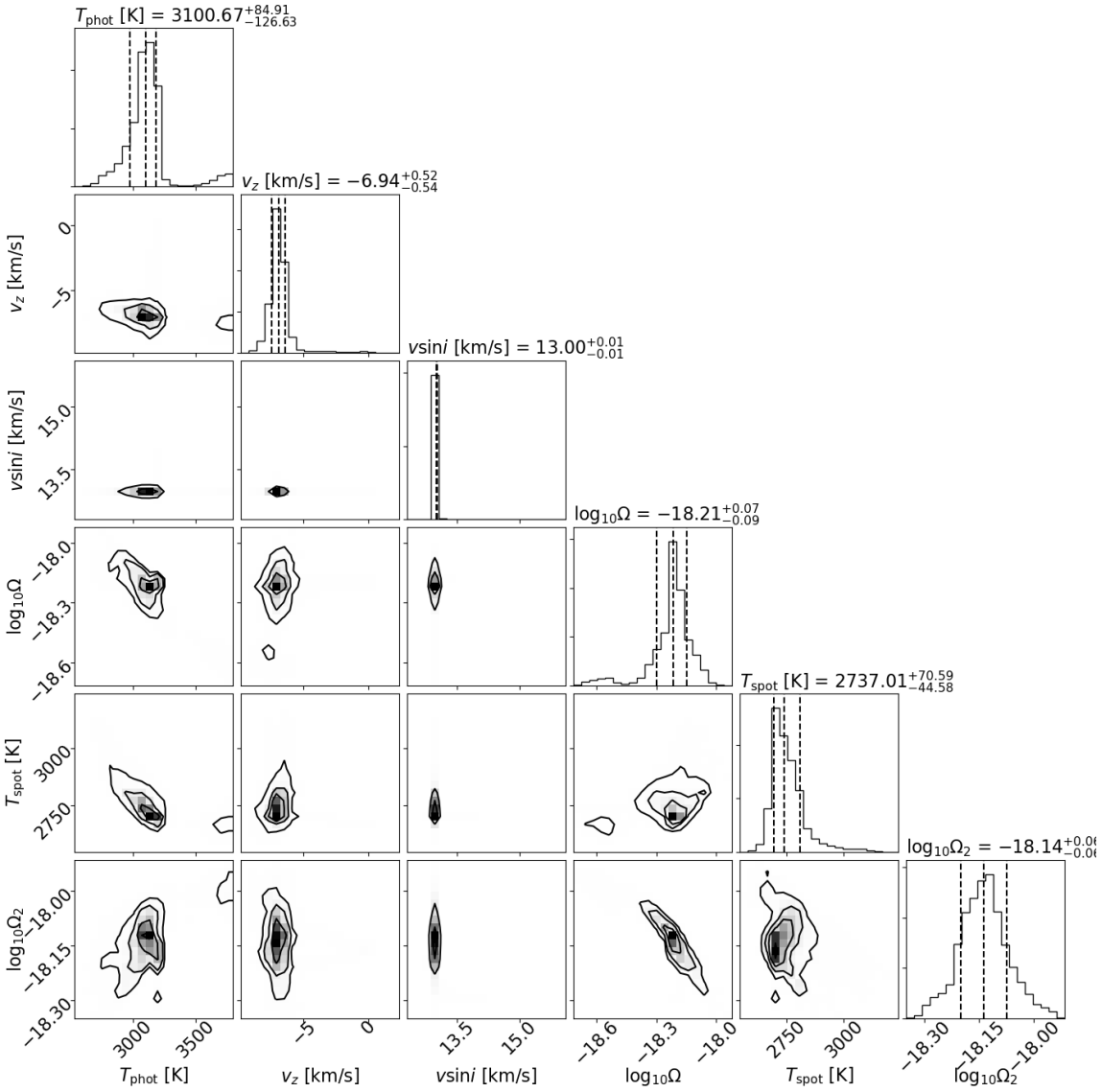

Fig. 5.4: Triangle plot showing the results of the MCMC simulation for a single IGRINS order. This order is the same order as shown in Figure 5.3 and has a central wavelength of 1.643 μm.

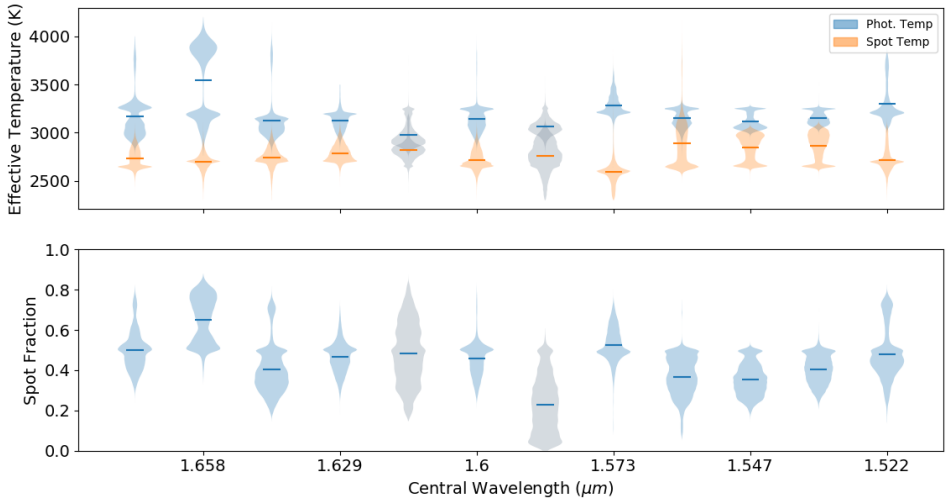

Fig. 5.5: **Top:** Probability distributions of the starspot temperature (orange) and photosphere temperature (blue) for 12 IGRINS orders, referred to by the central wavelength of the order. The distributions show the full MCMC simulation. Values that are more probable have wider distributions, and the mean value for each parameter is shown by a horizontal line. The gray boxes are the orders which had reduced χ^2 values larger than 1.5 and were not used in any of the analysis. The majority of the orders show consistent behavior, with a mean photosphere temperature of ∼3100 K and a mean spot temperature of ∼ 2650 K. **Bottom**: Probability distributions for the spot covering fraction calculated for each order using Equation 5.3.

dominated by a single large molecular feature such as FeH, the temperature difference between the photosphere and the spot manifests in the spectrum as all the molecular lines deepening or becoming more shallow together. A single temperature, or overlapping spot and photosphere temperature distributions, might then be measured instead of two separate temperature distributions. This is almost exactly what Figure 5.5 shows, with many of the overlapping orders showing both temperatures falling between 2600 K and 3300 K, with a best-fit spot and photosphere temperature around 2950 K. If this exercise is applied to more stars in the future, I can use only the orders that give good constraints on both the spot temperature and the

photosphere temperature, and exclude orders where there are not enough unique line strength changes, leading to overlapping temperature distributions.

In Figure 5.5, the majority of the orders exhibit a best-fit spot temperature of ∼2750 K and a best-fit photosphere temperature of ∼3200 K. However, the orders centered at 1.688, 1.658, 1.643, 1.6, 1.522 μm all show a second temperature peak in the photosphere temperature close to 3750 K. This peak always corresponds to a smaller Ω value and hence a smaller covering fraction. I interpret this second high temperature region of increased probability as a detection of faculae on the stellar surface. On the Sun, cool spots are always accompanied by faculae, or small bright regions with hotter temperatures. I did not initially include a third temperature in the MCMC simulation because observational evidence suggested that spots were the dominant feature in magnetically active stars (Lockwood et al. 2007). This does not mean faculae are not present; this means only that spots must have a significantly larger covering fraction, since Lockwood et al. (2007) found that on rapidly rotating active stars, the overall effective temperature decreased during times of increased activity indicators.

To further test the validity of this second temperature peak, I completely removed all of the temperature priors (the spot no longer had to be cooler than the photosphere), and I started the MCMC simulation of a single order at many random temperature initializations. In each case, three temperature regimes emerged. Figure 5.6 shows one of these cases, where the photosphere and the spot temperature each split into two or three different temperatures.

I combined all the probability distributions from the individual orders in Figures 5.7 and 5.8. Again, a second photosphere peak is clearly discernible. If this second peak is ignored, I derive a photosphere temperature of 3216 ± 228 K and a spot temperature of 2759 ± 154 K. These plots include all orders, even the ones with

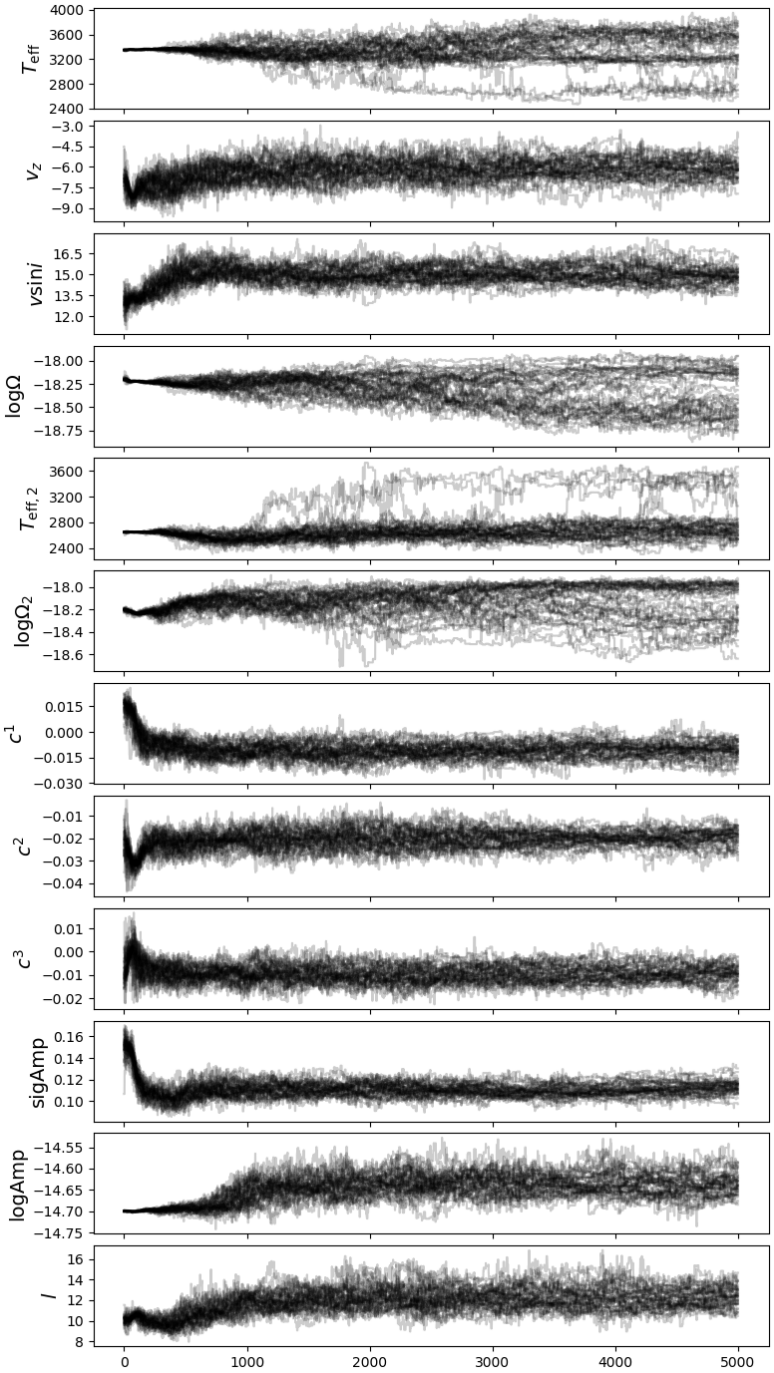

Fig. 5.6: MCMC walkers showing a simulation for 1 order. The walkers exploring $T_{\rm phot}$ ($T_{\rm eff}$) clearly find three regions of higher probability: one which corresponds to where the spot was previously detected, another which corresponds to where the photosphere was previously detected, and a third higher temperature region. The walkers exploring $T_{\rm spot}$ ($T_{\rm eff,2}$) also find the high temperature region. In this case I did not put any priors on the temperatures so there was nothing stopping the $T_{\rm eff}$ and $T_{\rm eff,2}$ walkers from overlapping.

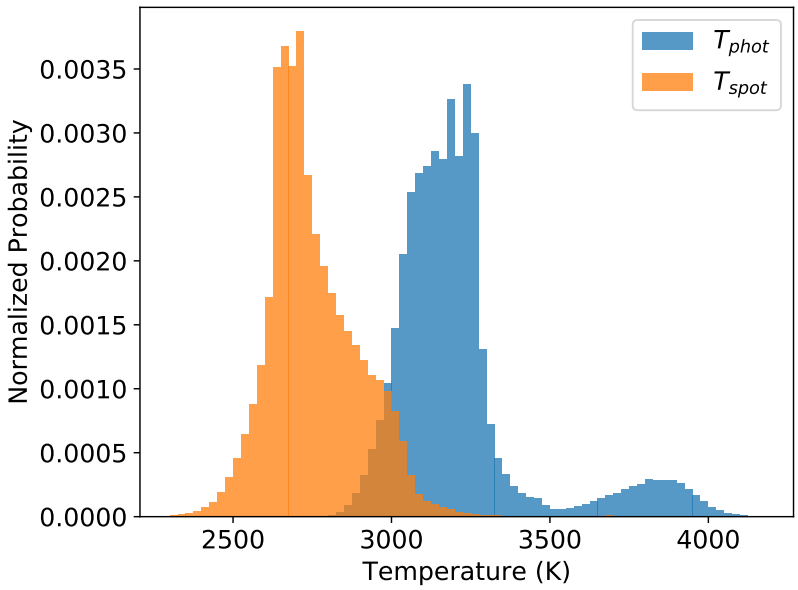

Fig. 5.7: Combined probability distributions of the spot temperature (orange) and photosphere temperature (blue) for all IGRINS orders that had a reduced χ^2 value less than 1.5. I found a mean photosphere temperature of 3216 ± 144 K and a spot temperature of 2769 ± 182 K, but a peak photosphere temperature around 3250 K and a peak spot temperature around 2700 K. The probability distribution for the spot temperature is slightly elongated due to the orders where the spectrum is fit best by a single temperature, as discussed above. The spot distribution then falls off sharply due to the prior specifying that the spot be cooler than the photosphere.

overlapping spot and photosphere temperatures. I find a spot covering fraction of $43 \pm 10\%$.

By tracing the individual walkers that separated into the three different temperature regimes, I was able to confirm that the higher temperature faculae region is associated with the elongated tail in Figure 5.8. The lowest point in the probability distribution in Figure 5.7 appears around 3500 K. I therefore called anything with a temperature less than 3500 K the photosphere and anything with a temperature greater than 3500 K faculae. This separation is shown in the top panel of Figure 5.9. Next, I determined which part of Figure 5.8 corresponded to the high temperature faculae (bottom panel of Figure 5.9). As expected, the lower covering fraction tail of

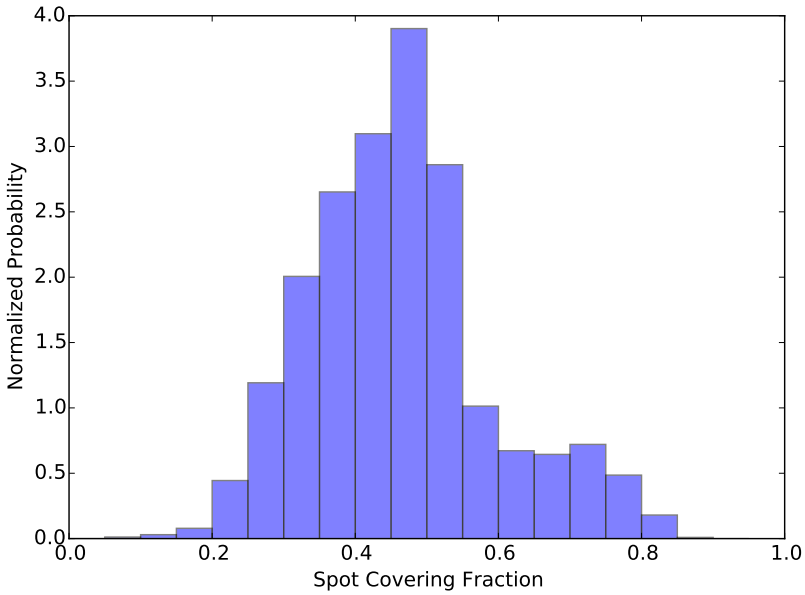

Fig. 5.8: Combined probability distribution of the spot covering fraction for all the IGRINS orders that had Reduced χ^2 values less than 1.5. I find a mean spot covering fraction of $43 \pm 10\%$. The tail at high spot covering fractions is due to the second photosphere temperature peak that has a small flux scaling factor.

the distribution was due to the high temperature distribution. Even though Figure 5.9 hints at a low covering fraction of faculae, it is not trivial to determine the exact value of Ω for all three temperature components since only two spectra of different temperatures are being fit simultaneously. Adding a third temperature spectrum greatly increases the computational time, and has even more of a tendency to overfit the data. In the future, this is something I can attempt, but it is not within the scope of this thesis, and for the remaining sections I will simply use the single spot temperature, photosphere temperature, and spot covering fraction.

The derived temperatures and filling fraction are consistent with previous indications that highly active M dwarfs can have spot covering fractions close to 50% (Newton et al. 2017) and spot temperatures that are between $200 - 500$ K less than photosphere temperatures (Barnes et al. 2015; Fang et al. 2016). Furthermore, I estimated the photosphere temperature to be 3216 ± 228 K, which is consistent with

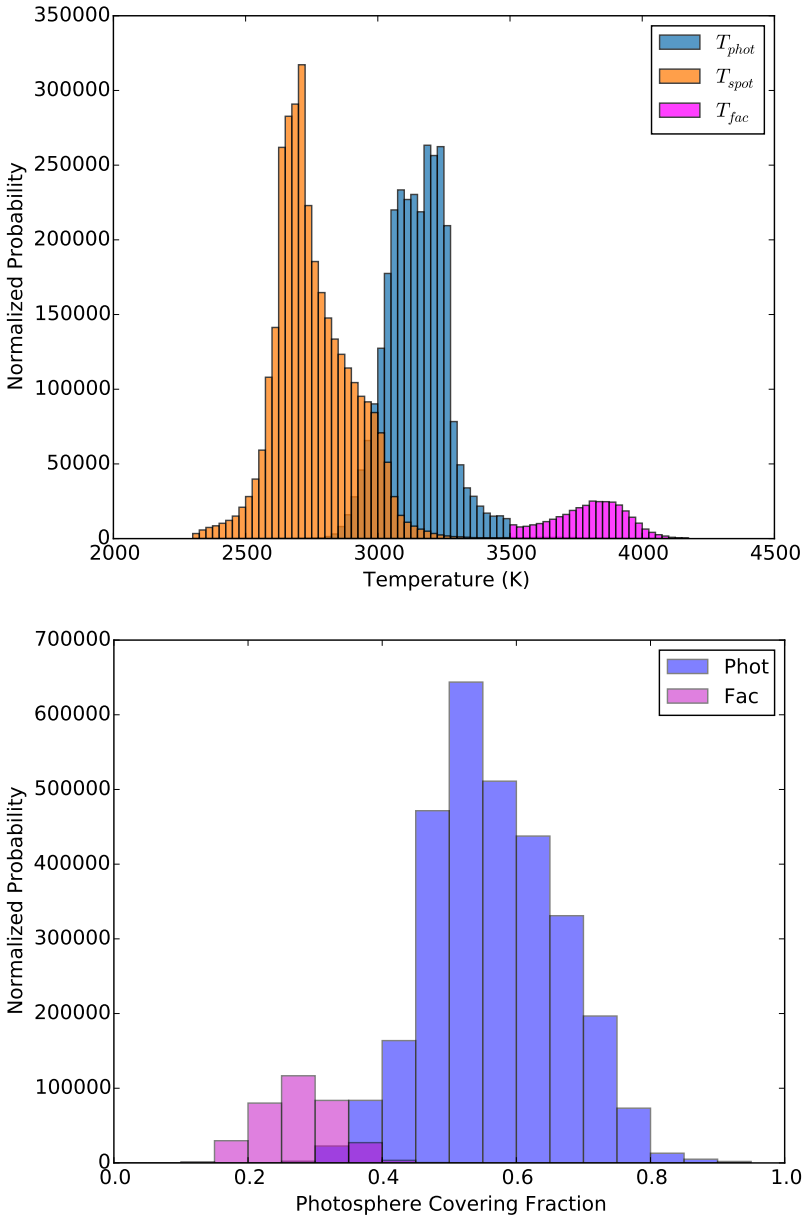

Fig. 5.9: **Top**: The same distribution as Figure 5.7, but with the photosphere distribution separated into two regimes. I used a cutoff temperature of 3500 K to distinguish the facula distribution from the photosphere distribution. **Bottom**: Distribution of the photosphere filling fraction from the parts of the MCMC simulation with Ω values corresponding to photosphere temperatures (blue), and for only the Ω values corresponding to the faculae temperatures (magenta). The faculae correspond to a lower filling fraction, as expected. The actual covering fraction of the faculae is not accurately represented in the plot since only two temperature components are assumed to derive these values, when in reality with the faculae included three temperature components and covering fractions would be present.

the literature temperature estimate of 3251 K from Newton et al. (2015) and the empirically derived temperature estimate of 3216 K derived using Mann et al. (2015).

5.6 Comparison With Models

By comparing the effective temperature estimated by the model to the photosphere temperature derived with Starfish, I determined whether spots alone are responsible for inflation or if global inhibition of convection is also present. If I detected low spot covering fractions and a photosphere temperature that was lower than the model predictions, then some form of global inhibition of convection would be primarily responsible for the observed inflation. Alternatively, a detection of a photosphere at a similar temperature to the model effective temperature, combined with a significant spot detection, would suggest that spots alone can inflate the radii of fully convective stars. Finally, a detection of spots and a photosphere temperature significantly lower than the model temperature would suggest a combination of global and local flux suppression. I detected a mean photosphere temperature of 3216 ± 228 K with a peak around 3250 K, while the models suggest a photosphere of 3359 ± 25 K. These two temperature are within 1-σ of each other and so a detection of any global inhibition of convection is not statistically significant, and contributes at most 5 and 8%.

With a more accurate spot temperature, photosphere temperature, and spot covering fraction, I was able to estimate how much larger 2MASS J23270216+2710367 would be than one would expect from the unspotted model. To do this, I used the following equation

$$(1/\eta)^2 = \frac{R^2_{\rm model}}{R^2_{\rm true}} = \frac{T^4_{\rm phot}\ \beta_{\rm phot} + T^4_{\rm spot}\ \beta_{\rm spot}}{T^4_{\rm model}}, \tag{5.4}$$

where η is the percentage radius inflation (see Chapter 4) and β is the covering fraction of the spot or photosphere. Using the best-fit parameters, I calculated an inflation percentage of 19%. An inflation percentage of 19% means that the spots are contributing 10 – 15% of the inflation and are the dominant mechanism of inflation for this star.

The estimated inflation percentage is larger than my results from Chapter 4, in which I showed that rapidly rotating fully convective M dwarf stars were on average 10–15% larger than models predicted, and shows a higher level of inflation than any of the stars from the most recent EB results (Parsons et al. 2018). A potential explanation for the larger-than-expected radius is that I omitted the temperature contribution from the faculae, which would raise the overall temperature of the star and mitigate some of the inflation.

My results are consistent with the modeling results from Chabrier et al. (2007). Due to the fact that this star is right on the edge of the fully-convective boundary, it is expected that some of the temperature discrepancy is due to global inhibition of convection, but that the majority is due to spots. This is the first observational evidence that confirms the Chabrier et al. (2007) modeling result, and future work to further confirm the theory could determine whether spots on partially convective M dwarf stars could explain discrepancies seen in EB observations or whether a global temperature change is required to match those observations. Furthermore, these results suggest that by adding spots to models, models would be able to predict M dwarf radii more accurately. However, before changes to models can be implemented it is imperative to determine how the spot temperatures and spot covering fractions change with parameters such as mass and magnetic activity.

5.7 Summary

I deduced that one of the most magnetically active M dwarf stars has spots covering ∼45% of its surface. The spots are ∼400 K cooler than the quiescent stellar surface. I found evidence that faculae may be present on the surface of this star, but to confirm their existence and to determine exact covering fractions, more testing is required. Using my derived spot properties, I calculated that 2MASS J23270216+2710367 is ∼19% larger than an unspotted model predicts. This value is larger than the 10–15% radius inflation that I measured in Chapter 4 when I compared the radii of rapidly rotating fully convective M dwarfs to model estimates, but it is not significantly larger. By adding effects of faculae, the discrepancy may be mitigated. In 2MASS J23270216+2710367 spots seem to be primarily responsible for the inflation. This suggests that models would be able to predict the radii of M dwarfs more accurately if spots were included. However, to correctly incorporate spots into the models, more information on the ways in which spot properties change with mass and magnetism is necessary.

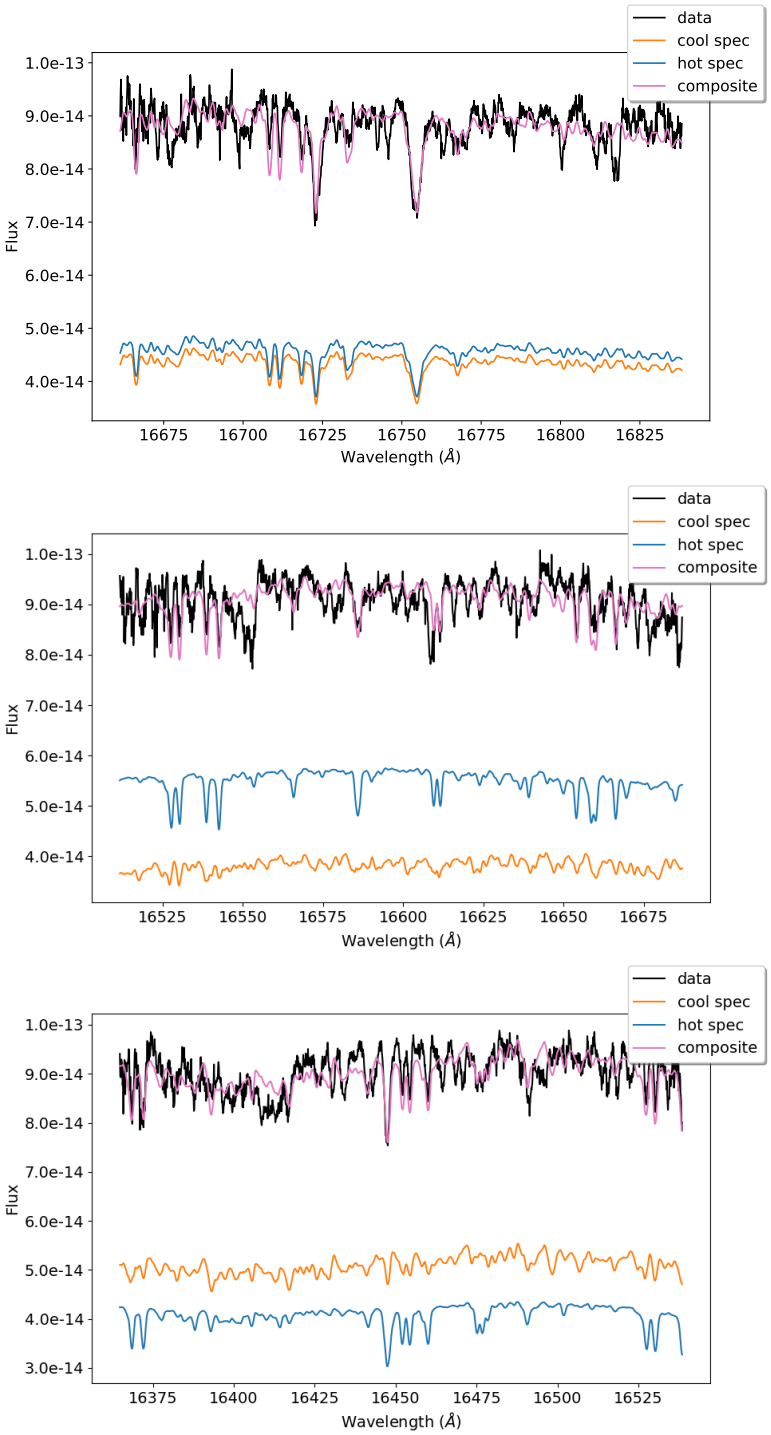

Fig. 5.10: Similar to Figure 5.3, I am showing the spectra for a the first three IGRINS orders (black) compared to the best-fit model spectrum (magenta). The best-fit spectrum is composed of a hot component (blue) and a cool component (orange).

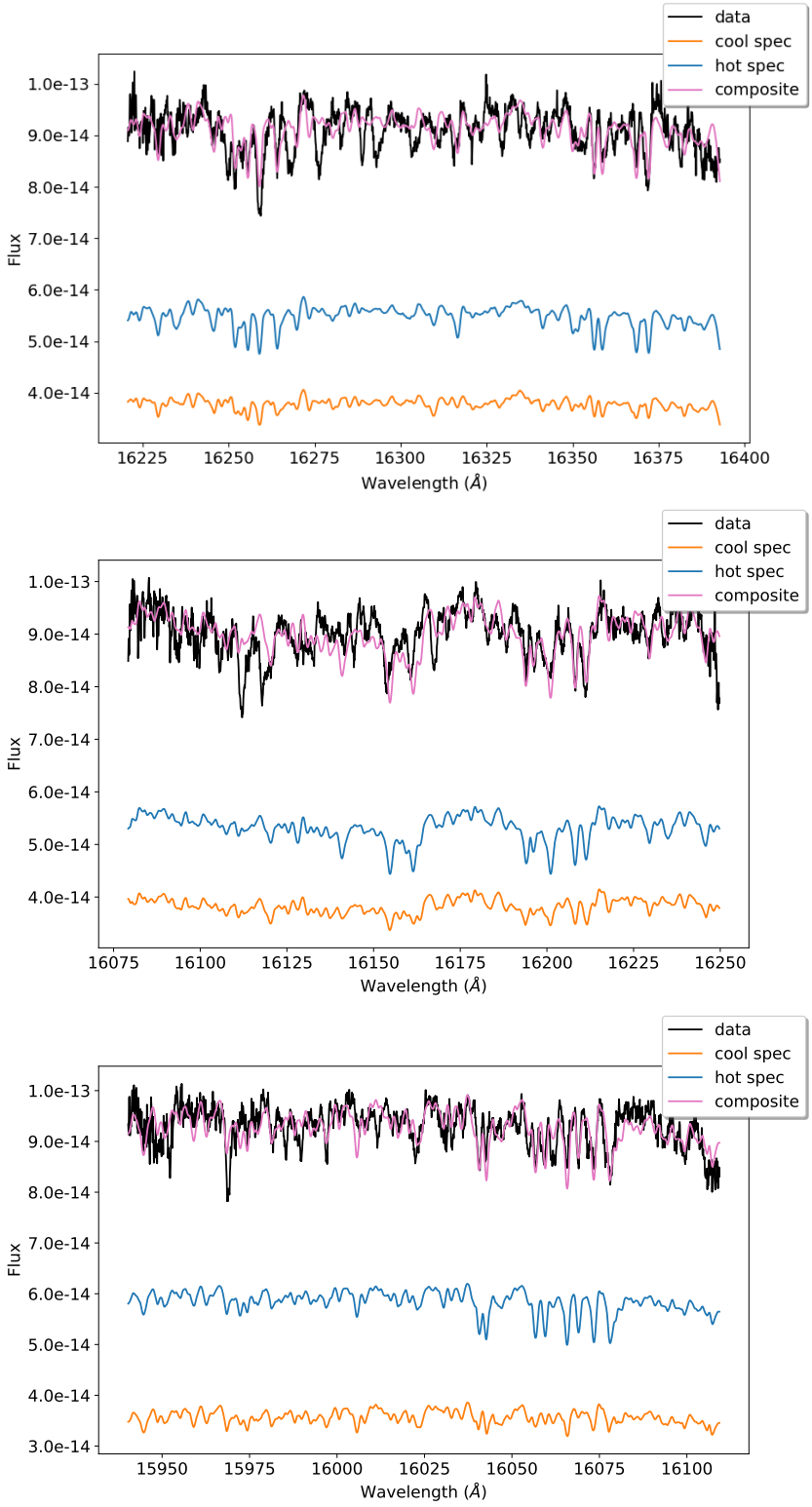

Fig. 5.11: Same as Figure 5.10

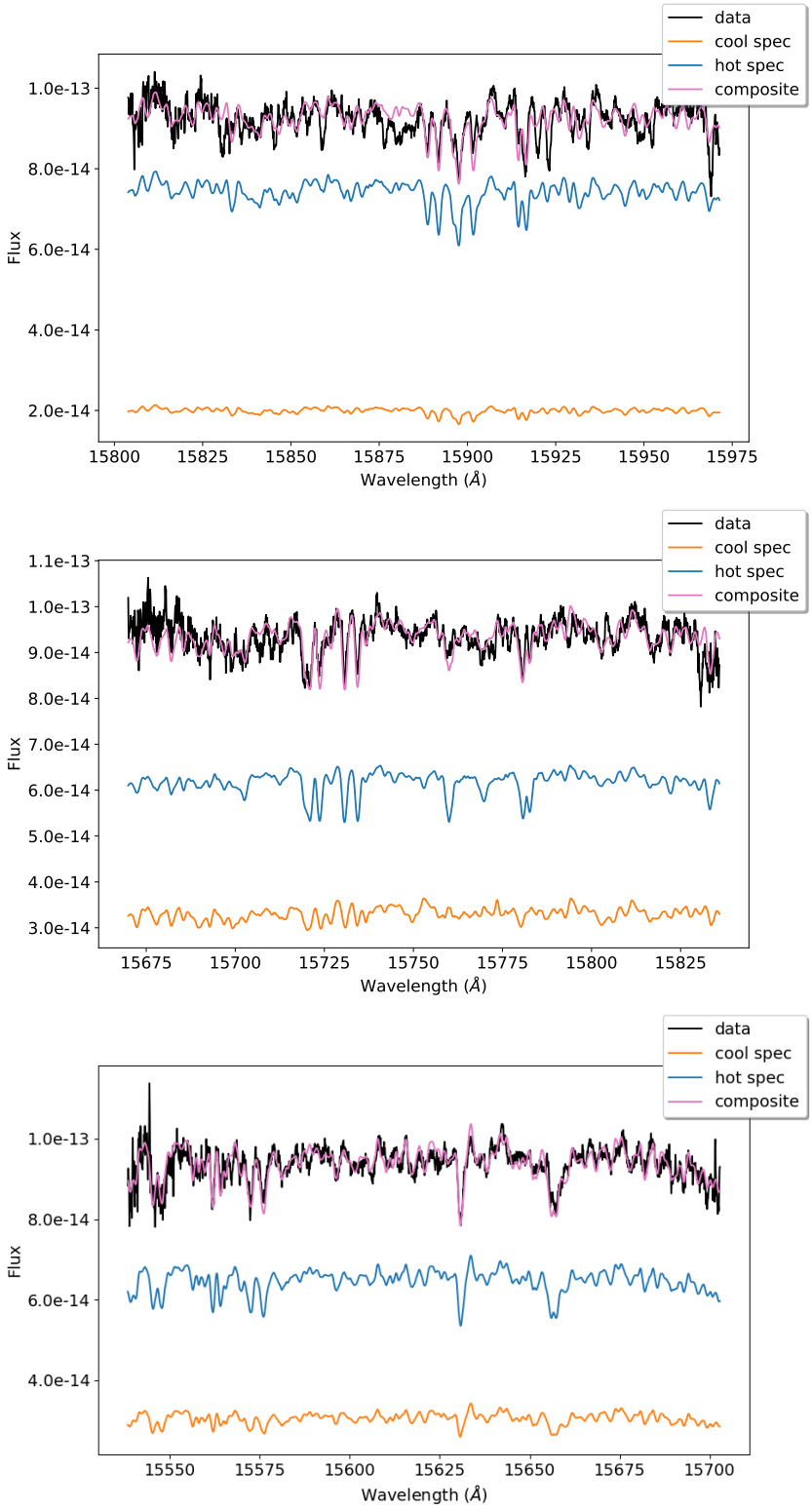

Fig. 5.12: Same as Figure 5.10

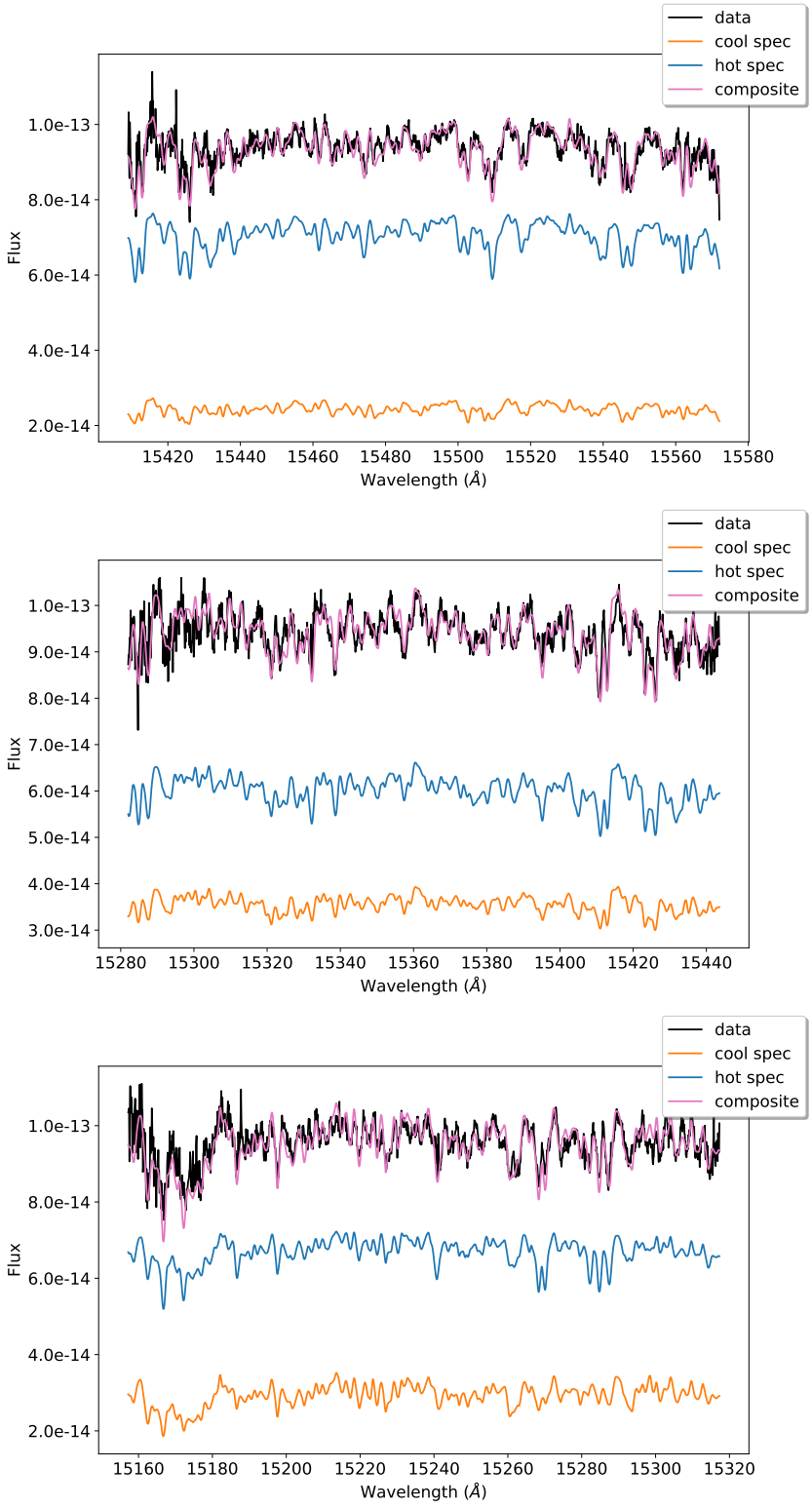

Fig. 5.13: Same as Figure 5.10

Chapter 6

Conclusions

The goal of my dissertation was to determine the cause of the discrepancy between models and observations of M dwarf radii. Observations of M dwarf stars from LBOI, EBs, and those derived using the Stefan Boltzmann method all show evidence that models are under predicting the stellar radii by an average of 5-10% for a given mass (Torres & Ribas 2002; Morales et al. 2008; Boyajian et al. 2012). The two main hypotheses evoked to explain this discrepancy involve the effects of (1) metallicity, and (2) magnetism.

Metallicity controls the opacity of the atmosphere; in metal poor stars, hydrostatic equilibrium is achieved at a smaller radius. Theory predicts that for a given temperature, luminosity, or mass, low metallicity stars will be smaller than high metallicity stars. Mann et al. (2015) confirmed that the radii of M dwarfs were metallicity dependent when temperature was held constant, but observations had yet to determine whether M dwarf radii were metallicity dependent when luminosity or mass was held constant.

Strong magnetic fields are thought to inhibit convection and lead to cooler surface temperatures, and thus larger radii. M dwarf stars are known to host strong surface magnetic fields that have been measured to be over a thousand times stronger than the Sun's surface magnetic field (e.g., Donati et al. 2006). The inhibition of convective flux can either be localized, occurring around magnetic cool spots on the star's surface, or it can occur throughout the convective envelope, lowering the

temperature of the entire stellar surface (which can be modeled by decreasing the mixing length parameter, α). However, decreasing the mixing length parameter has a significant effect only on higher mass M dwarfs. This is because lower mass M dwarfs (M $\lesssim 0.35\ M_{\rm Sun}$) are so dense that convection is still efficient, despite a decrease in α. Therefore, it is predicted that spots on the surfaces of low-mass M dwarfs are the dominant cause of radius inflation via magnetic fields.

To test both of these radius-altering mechanisms, I measured radii of two different statistical samples of M dwarf stars – one selected to test metallicity effects, and the other to test magnetic effects. Both surveys contained observations of more than 85 stars, resulting in large statistical samples with which the parameters of interest could be investigated.

To determine the effect of metallicity on the radii of M dwarfs, I measured the radii of 88 stars using the Stefan Boltzmann method. The stars were specifically selected to include many targets with metallicities less than -1.0 dex and spectral types that spanned K7 though M7. It was important that many of the stars that were selected had extremely low metallicities. This is because previous studies had only tested near-solar metallicity stars, and this led to conflicting results regarding the effect of metallicity on M dwarf radii. I found that for a given temperature, a star with a metallicity of -2.0 dex can be smaller than a solar metallicity star by up to a factor of five. This large metallicity effect was predicted by the Baraffe et al. (1997) stellar evolution models, but had not been confirmed observationally. Since the models are in agreement with my data, these results provide the first validation of the models for the lowest stellar temperatures and metallicities. While this was not the first time that M dwarf radii were shown to be metallicity dependent for a given temperature, the extent to which metallicity alters the radii had not been observed previously.

I also tested the degree to which the radii dependent on metallicity when other parameters were held constant. I found that, similar to temperature, radii for a given color were highly metallicity dependent. Previous studies demonstrated that absolute K_s band to radius relations seemed to be insensitive to metallicity and showed the least scatter, leading to the most accurate radius estimates (Boyajian et al. 2012; Mann et al. 2015). In agreement with these previous studies, I found that an absolute K_s band to radius relation returned the least scatter and the most accurate radii. Unlike previous studies, however, I found a slight metallicity dependence. The lowest metallicity stars in the sample were at most 10-15% smaller than the highest metallicity stars in the sample. Therefore, while a K_s-to-radius relation is metallicity dependent, in order to see any change in the radius, an extremely large change in metallicity is required ($>$ 2.0 dex). To aid in future determinations of low-metallicity M dwarf radii, I presented relations that can be used to convert these direct observables (color and M_{K_s}) to radii. I updated an existing absolute K_s-band magnitude-to-radius relation such that the relation is valid for spectral types between K7 and M7, and metallicities down to -2.0 dex, with an uncertainty of only 6%.

Absolute K_s-band magnitude and mass are tightly correlated (Benedict et al. 2016) and metallicity dependency in recent M_{K_s} $-$ $-$Mass relations is negligible (Mann et al. 2019). Therefore, one would expect that there would be little metallicity-dependent scatter in a Mass–Radius plot since there is not much metallicity-dependent scatter in the M_{K_s}–Radius relation. To test this hypothesis I calculated mass estimates for all of the stars in my sample using a relation from (Benedict et al. 2016). As expected, to obtain an offset of 10-15%, a change in metallicity of more than 2.0 dex is required. Since evidence for radius inflation is primarily found for nearby solar-metallicity stars, I conclude that metallicity is unlikely to be the main cause of the radius discrepancies in Mass–Radius diagrams.

Next, to determine the role of magnetism on the radii of M dwarf stars, I tested the degree to which magnetically active, rapidly rotating, fully convective M dwarf stars were inflated compared to stellar evolution models and empirically determined relations. To do this, I developed a technique to measure the statistical distribution of a large number of M dwarf radii modulated by the rotational inclination ($R_\star \sin i$) of single, rapidly rotating M dwarf stars. To calculate $R_\star \sin i$ for each target star, I combined photometric rotation periods ($P_{\rm rot}$) from the literature with rotational broadening measurements ($v \sin i$) that I obtained. By assuming the inclinations were randomly oriented on the sky, I was able to extract information about the stellar radii using a Bayesian modeling approach.

I found that the magnetically active, rapidly rotating, fully convective M dwarf stars were on average $10 - 16\%$ larger than predictions from stellar evolutionary models. The most recent results of all compiled EBs in the literature show an average inflation of 6%, with a peak inflation of 12% (Parsons et al. 2018). Radii measured through LBOI also show an average inflation of 5% (Boyajian et al. 2012). The results from EBs, LBOI, and those presented here have a large range of rotation periods, and presumably magnetic field strengths, due to the fact that most of the LBOI stars are slowly rotating and the EBs have a range of rotation periods. Therefore, I conclude that *all* M dwarfs with near-solar metallicity are on average larger than model predictions.

When I split the sample into two mass bins, I found the larger mass stars ($M > 0.18\ M_{\rm Sun}$) to be only $5 - 7\%$ larger than the model predictions, while the lowest mass stars were $13 - 17\%$ larger than the model predictions. I argued that the larger radii of the lowest-mass stars are not completely due to their young age, but some of the $13 - 17\%$ inflation could be due to these very low-mass stars having not settled onto the main sequence.

I also compared my rapidly rotating, magnetically active stars to empirical relations and found that the most recent relations from Benedict et al. (2016) and Boyajian et al. (2012) are consistent to within $\sim 5\%$. The Bayesian analysis showed a peak inflation compared to the empirical relations of 5%, meaning that the stars in my sample could be 5% larger than the stars used by Boyajian et al. (2012). This result was, however, not statistically significant. The stars used to determine the empirical relations had much slower rotation periods than the stars in my sample, so if the 5% discrepancy between my stars and the stars used in Boyajian et al. (2012) is real, it could be due to rotation and magnetic field strength. However, any potential change due to rotation can only inflate the radii by $\sim 5\%$.

Finally, to determine whether the radius inflation I measured was due to localized starspots or a decrease in the mixing length, I determined spot properties on one of the rapidly rotating magnetically active stars in my sample. To do this, I looked for spectral signatures of two different photospheric temperatures in a high resolution infrared spectrum using a spectral analysis tool, known as Starfish. To obtain constraint on the role of spots on radius inflation, I then compared the temperatures derived from the observations to temperature predictions from models.

I found evidence that one of the most magnetically active M dwarf stars in my sample had spots covering almost 50% of its surface. The spots are $\sim$400K cooler than the quiescent stellar surface. When photosphere temperature priors were relaxed, I also found evidence of faculae on the surface of this star; however, more testing is required to confirm this result.

When I compared these temperatures to those given by models, I found that the photosphere temperature is consistent to within $\sim$1-σ, leading me to conclude that spots are the dominant source of radius inflation in this star. If global inhibition of convection exists at all, it contributes at most 5-8%. For stars of even lower mass

than I studied, this percentage should to decrease. Therefore, my work shows that models should include effects of spots to predict stellar parameters more accurately in the future.

I used my derived spot parameters to calculate how much larger this star would be than predicted by models. The result was that this star would be inflated by 19% compared to an unspotted model. 19% is potentially overestimated due to the effects of faculae not being included. I previously predicted that even slowly rotating M dwarfs are inflated by 3–5%. Assuming this to be true, I can calculate their spot covering fraction using my measured spot and photosphere temperatures. I find that between 13 and 20% of the surface of a star needs to be covered in spots to inflate the star by 3-5%. I propose that all M dwarfs are spotted to some degree, which is confirmed by rotational modulation detected in the light curves of even the slowest rotators with periods of 100 days (Newton et al. 2017). I expect slow rotators to be ∼3-5% larger than model predictions and have spot covering fractions of about 10-20%, while rapid rotators are 15-20% larger than model predictions and have spot covering fractions of ∼50%. This result can explain all of the scatter seen in the most recent Mass–Radius diagram (e.g., Parsons et al. 2018).

In summary, I demonstrated that metallicity can significantly effect the radii of M dwarf stars if parameters such as effective temperature or color are used to determine the radii. Parameters such as M_{K_s} and mass are, however, only slightly metallicity dependent. Therefore, any scatter in the Mass–Radius diagram is likely not attributed to metallicity effects. I also found that magnetically active, rapidly rotating, fully convective stars were on average $10 - 16\%$ larger than model predictions. I argue that any effect of rotation on the radii of M dwarfs can at most inflate the radii by $5 - 10\%$, and that all radii (even those of slow rotators) are inflated by $3 - 5\%$ on average. Next, I measured a starspot temperature that was ∼400 K

less than the photosphere and a spot covering fraction close to 50% on a single M dwarf. This lead to the conclusion that the star's radius is $\sim 19\%$ larger than model predictions. I determined that spots were the primary cause of radius inflation, but that global inhibition of convection could account for up to 5–8% of the inflation. In even lower-mass stars I expect that spots alone are the cause of any radius inflation. Finally, I provided evidence that an M_{K_s}–Radius relation is the most accurate way to determine radii of stars empirically. It is valid to within $5 - 10\%$ for both a large range of metallicities and a large range of rotation periods, even at the lowest-mass end of the main sequence.

List of Journal Abbreviations

A&A	Astronomy and Astrophysics
AJ	Astronomical Journal
ApJ	Astrophysical Journal
ApJS	Astrophysical Journal Supplements
Am. Stat	The American Statistician
Am. Stat. Assoc.	American Statistical Association
ARA&A	Annual Review of Astronomy and Astrophysics
MNRAS	Monthly Notices of the Astronomical Royal
PASP	Publications of the Astronomical Society of the Pacific
Proc. SPIE	Society of Photo-Optical Instrumentation Engineers Conference Proceedings
Sol. Phys.	Solar Physics

References

Alam, S., Albareti, F. D., Allende Prieto, C., Anders, F., Anderson, S. F., Anderton, T., Andrews, B. H., Armengaud, E., Aubourg, É., Bailey, S., & et al. 2015, ApJS, 219, 12

Allard, F. & Hauschildt, P. H. 1995, ApJ, 445, 433

Allard, F., Homeier, D., & Freytag, B. 2012, Royal Society of London Philosophical Transactions Series A, 370, 2765

Alonso-Floriano, F. J., Morales, J. C., Caballero, J. A., Montes, D., Klutsch, A., Mundt, R., Cortés-Contreras, M., Ribas, I., Reiners, A., Amado, P. J., Quirrenbach, A., & Jeffers, S. V. 2015, A&A, 577, A128

Andrae, R., Fouesneau, M., Creevey, O., Ordenovic, C., Mary, N., Burlacu, A., Chaoul, L., Jean-Antoine-Piccolo, A., Kordopatis, G., Korn, A., Lebreton, Y., Panem, C., Pichon, B., Thévenin, F., Walmsley, G., & Bailer-Jones, C. A. L. 2018, A&A, 616, A8

Bailer-Jones, C. A. L., Rybizki, J., Fouesneau, M., Mantelet, G., & Andrae, R. 2018, AJ, 156, 58

Baraffe, I. & Chabrier, G. 2018, A&A, 619, A177

Baraffe, I., Chabrier, G., Allard, F., & Hauschildt, P. H. 1997, A&A, 327, 1054

Baraffe, I., Homeier, D., Allard, F., & Chabrier, G. 2015, A&A, 577, A42

Barnes, J. R., Collier Cameron, A., Donati, J.-F., James, D. J., Marsden, S. C., & Petit, P. 2005, MNRAS, 357, L1

Barnes, J. R., Jeffers, S. V., Jones, H. R. A., Pavlenko, Y. V., Jenkins, J. S., Haswell, C. A., & Lohr, M. E. 2015, ApJ, 812, 42

Barnes, S. A. 2003, ApJ, 586, 464

Bayless, A. J. & Orosz, J. A. 2006, ApJ, 651, 1155

Beers, T. C. & Christlieb, N. 2005, ARA&A, 43, 531

Benedict, G. F., Henry, T. J., Franz, O. G., McArthur, B. E., Wasserman, L. H., Jao, W.-C., Cargile, P. A., Dieterich, S. B., Bradley, A. J., Nelan, E. P., & Whipple, A. L. 2016, AJ, 152, 141

Benedict, G. F., McArthur, B., Nelan, E., Story, D., Whipple, A. L., Shelus, P. J., Jefferys, W. H., Hemenway, P. D., Franz, O. G., Wasserman, L. H., Duncombe, R. L., van Altena, W., & Fredrick, L. W. 1998, AJ, 116, 429

Berger, D. H., Gies, D. R., McAlister, H. A., ten Brummelaar, T. A., Henry, T. J., Sturmann, J., Sturmann, L., Turner, N. H., Ridgway, S. T., Aufdenberg, J. P., & Mérand, A. 2006, ApJ, 644, 475

Berta, Z. K., Irwin, J., Charbonneau, D., Burke, C. J., & Falco, E. E. 2012, AJ, 144, 145

Bessell, M. S. & Brett, J. M. 1988, PASP, 100, 1134

Bochanski, J. J., Hawley, S. L., Covey, K. R., West, A. A., Reid, I. N., Golimowski, D. A., & Ivezić, Ž. 2010, AJ, 139, 2679

Bochanski, J. J., West, A. A., Hawley, S. L., & Covey, K. R. 2007, AJ, 133, 531

Bochanski, J. J., Willman, B., West, A. A., Strader, J., & Chomiuk, L. 2014, AJ, 147, 76

Boyajian, T. S., von Braun, K., van Belle, G., McAlister, H. A., ten Brummelaar, T. A., Kane, S. R., Muirhead, P. S., Jones, J., White, R., Schaefer, G., Ciardi, D., Henry, T., López-Morales, M., Ridgway, S., Gies, D., Jao, W.-C., Rojas-Ayala, B., Parks, J. R., Sturmann, L., Sturmann, J., Turner, N. H., Farrington, C., Goldfinger, P. J., & Berger, D. H. 2012, ApJ, 757, 112

Bressan, A., Marigo, P., Girardi, L., Salasnich, B., Dal Cero, C., Rubele, S., & Nanni, A. 2012, MNRAS, 427, 127

Browning, M. K. 2008, ApJ, 676, 1262

Browning, M. K., Weber, M. A., Chabrier, G., & Massey, A. P. 2016, ApJ, 818, 189

Burgasser, A. J. 2014, in Astronomical Society of India Conference Series, Vol. 11, Astronomical Society of India Conference Series

Burgasser, A. J., Kirkpatrick, J. D., Burrows, A., Liebert, J., Reid, I. N., Gizis, J. E., McGovern, M. R., Prato, L., & McLean, I. S. 2003, ApJ, 592, 1186

Burrows, A., Hubbard, W. B., Saumon, D., & Lunine, J. I. 1993, ApJ, 406, 158

Çakırlı, Ö., İbanoğlu, C., & Sipahi, E. 2013, MNRAS, 429, 85

Caffau, E., Ludwig, H.-G., Steffen, M., Freytag, B., & Bonifacio, P. 2011, Sol. Phys., 268, 255

Cannon, A. J. & Pickering, E. C. 1901, Annals of Harvard College Observatory, 28, 129

Cassisi, S. & Salaris, M. 2019, A&A, 626, A32

Chabrier, G. & Baraffe, I. 1997, A&A, 327, 1039

—. 2000, ARA&A, 38, 337

Chabrier, G., Gallardo, J., & Baraffe, I. 2007, A&A, 472, L17

Chambers, K. C., Magnier, E. A., Metcalfe, N., Flewelling, H. A., Huber, M. E., Waters, C. Z., Denneau, L., Draper, P. W., Farrow, D., Finkbeiner, D. P., Holmberg, C., Koppenhoefer, J., Price, P. A., Rest, A., Saglia, R. P., Schlafly, E. F., Smartt, S. J., Sweeney, W., Wainscoat, R. J., Burgett, W. S., Chastel, S., Grav, T., Heasley, J. N., Hodapp, K. W., Jedicke, R., Kaiser, N., Kudritzki, R.-P., Luppino, G. A., Lupton, R. H., Monet, D. G., Morgan, J. S., Onaka, P. M., Shiao, B., Stubbs, C. W., Tonry, J. L., White, R., Bañados, E., Bell, E. F., Bender, R., Bernard, E. J., Boegner, M., Boffi, F., Botticella, M. T., Calamida, A., Casertano, S., Chen, W.-P., Chen, X., Cole, S., Deacon, N., Frenk, C., Fitzsimmons, A., Gezari, S., Gibbs, V., Goessl, C., Goggia, T., Gourgue, R., Goldman, B., Grant, P., Grebel, E. K., Hambly, N. C., Hasinger, G., Heavens, A. F., Heckman, T. M., Henderson, R., Henning, T., Holman, M., Hopp, U., Ip, W.-H., Isani, S., Jackson, M., Keyes, C. D., Koekemoer, A. M., Kotak, R., Le, D., Liska, D., Long, K. S., Lucey, J. R., Liu, M., Martin, N. F., Masci, G., McLean, B., Mindel, E., Misra, P., Morganson, E., Murphy, D. N. A., Obaika, A., Narayan, G., Nieto-Santisteban, M. A., Norberg, P., Peacock, J. A., Pier, E. A., Postman, M., Primak, N., Rae, C., Rai, A., Riess, A., Riffeser, A., Rix, H. W., Röser, S., Russel, R., Rutz, L., Schilbach, E., Schultz, A. S. B., Scolnic, D., Strolger, L., Szalay, A., Seitz, S., Small, E., Smith, K. W., Soderblom, D. R., Taylor, P., Thomson, R., Taylor, A. N., Thakar, A. R., Thiel, J., Thilker, D., Unger, D., Urata, Y., Valenti, J., Wagner, J., Walder, T., Walter, F., Watters, S. P., Werner, S., Wood-Vasey, W. M., & Wyse, R. 2016, arXiv e-prints

Charbonneau, D., Berta, Z. K., Irwin, J., Burke, C. J., Nutzman, P., Buchhave, L. A., Lovis, C., Bonfils, X., Latham, D. W., Udry, S., Murray-Clay, R. A., Holman, M. J., Falco, E. E., Winn, J. N., Queloz, D., Pepe, F., Mayor, M., Delfosse, X., & Forveille, T. 2009, Nature, 462, 891

Chen, Y., Girardi, L., Bressan, A., Marigo, P., Barbieri, M., & Kong, X. 2014, MNRAS, 444, 2525

Choi, J., Dotter, A., Conroy, C., Cantiello, M., Paxton, B., & Johnson, B. D. 2016, ApJ, 823, 102

Claret, A., Hauschildt, P. H., & Witte, S. 2012, A&A, 546, A14

Conroy, C. & van Dokkum, P. G. 2012, ApJ, 760, 71

Covey, K. R., Hawley, S. L., Bochanski, J. J., West, A. A., Reid, I. N., Golimowski, D. A., Davenport, J. R. A., Henry, T., Uomoto, A., & Holtzman, J. A. 2008, AJ, 136, 1778

Covey, K. R., Ivezić, Ž., Schlegel, D., Finkbeiner, D., Padmanabhan, N., Lupton, R. H., Agüeros, M. A., Bochanski, J. J., Hawley, S. L., West, A. A., Seth, A., Kimball, A., Gogarten, S. M., Claire, M., Haggard, D., Kaib, N., Schneider, D. P., & Sesar, B. 2007a, AJ, 134, 2398

—. 2007b, AJ, 134, 2398

Cox, A. N. 2000, Allen's astrophysical quantities

Cushing, M. C., Marley, M. S., Saumon, D., Kelly, B. C., Vacca, W. D., Rayner, J. T., Freedman, R. S., Lodders, K., & Roellig, T. L. 2008, ApJ, 678, 1372

Cushing, M. C., Vacca, W. D., & Rayner, J. T. 2004, PASP, 116, 362

Czekala, I., Andrews, S. M., Mandel, K. S., Hogg, D. W., & Green, G. M. 2015, ApJ, 812, 128

Davenport, J. R. A., Covey, K. R., Clarke, R. W., Boeck, A. C., Cornet, J., & Hawley, S. L. 2019, ApJ, 871, 241

Davenport, J. R. A., Hebb, L., & Hawley, S. L. 2015, ApJ, 806, 212

Davison, C. L., White, R. J., Henry, T. J., Riedel, A. R., Jao, W.-C., Bailey, III, J. I., Quinn, S. N., Cantrell, J. R., Subasavage, J. P., & Winters, J. G. 2015, AJ, 149, 106

Delfosse, X., Forveille, T., Perrier, C., & Mayor, M. 1998, A&A, 331, 581

Delfosse, X., Forveille, T., Ségransan, D., Beuzit, J.-L., Udry, S., Perrier, C., & Mayor, M. 2000, A&A, 364, 217

Demarque, P., Woo, J.-H., Kim, Y.-C., & Yi, S. K. 2004, ApJS, 155, 667

Demory, B.-O., Ségransan, D., Forveille, T., Queloz, D., Beuzit, J.-L., Delfosse, X., di Folco, E., Kervella, P., Le Bouquin, J.-B., Perrier, C., Benisty, M., Duvert, G., Hofmann, K.-H., Lopez, B., & Petrov, R. 2009, A&A, 505, 205

Deshpande, R., Blake, C. H., Bender, C. F., Mahadevan, S., Terrien, R. C., Carlberg, J. K., Zasowski, G., Crepp, J., Rajpurohit, A. S., Reylé, C., Nidever, D. L., Schneider, D. P., Allende Prieto, C., Bizyaev, D., Ebelke, G., Fleming, S. W., Frinchaboy, P. M., Ge, J., Hearty, F., Hernández, J., Malanushenko, E., Malanushenko, V., Majewski, S. R., Marchwinski, R., Muna, D., Oravetz, D., Pan, K., Schiavon, R. P., Shetrone, M., Simmons, A., Stassun, K. G., Wilson, J. C., & Wisniewski, J. P. 2013, AJ, 146, 156

Dhital, S., West, A. A., Stassun, K. G., Bochanski, J. J., Massey, A. P., & Bastien, F. A. 2012, AJ, 143, 67

Dittmann, J. A., Irwin, J. M., Charbonneau, D., & Berta-Thompson, Z. K. 2014, ApJ, 784, 156

Donahue, R. A., Saar, S. H., & Baliunas, S. L. 1996, ApJ, 466, 384

Donati, J.-F., Forveille, T., Collier Cameron, A., Barnes, J. R., Delfosse, X., Jardine, M. M., & Valenti, J. A. 2006, Science, 311, 633

Dotter, A., Chaboyer, B., Ferguson, J. W., Lee, H.-c., Worthey, G., Jevremović, D., & Baron, E. 2007, ApJ, 666, 403

Dotter, A., Chaboyer, B., Jevremović, D., Kostov, V., Baron, E., & Ferguson, J. W. 2008, ApJS, 178, 89

Dressing, C. D. & Charbonneau, D. 2015, ApJ, 807, 45

Duchêne, G. & Kraus, A. 2013, ARA&A, 51, 269

Evans, D. W., Riello, M., De Angeli, F., Carrasco, J. M., Montegriffo, P., Fabricius, C., Jordi, C., Palaversa, L., Diener, C., Busso, G., Cacciari, C., van Leeuwen, F., Burgess, P. W., Davidson, M., Harrison, D. L., Hodgkin, S. T., Pancino, E., Richards, P. J., Altavilla, G., Balaguer-Núñez, L., Barstow, M. A., Bellazzini, M., Brown, A. G. A., Castellani, M., Cocozza, G., De Luise, F., Delgado, A., Ducourant, C., Galleti, S., Gilmore, G., Giuffrida, G., Holl, B., Kewley, A., Koposov, S. E., Marinoni, S., Marrese,

P. M., Osborne, P. J., Piersimoni, A., Portell, J., Pulone, L., Ragaini, S., Sanna, N., Terrett, D., Walton, N. A., Wevers, T., & Wyrzykowski, Ł. 2018, A&A, 616, A4

Fang, X.-S., Zhao, G., Zhao, J.-K., Chen, Y.-Q., & Bharat Kumar, Y. 2016, MNRAS, 463, 2494

Feiden, G. A. & Chaboyer, B. 2012, ArXiv e-prints

—. 2014, ApJ, 789, 53

Filippazzo, J. C., Rice, E. L., Faherty, J., Cruz, K. L., Van Gordon, M. M., & Looper, D. L. 2015, ApJ, 810, 158

Foreman-Mackey, D., Hogg, D. W., Lang, D., & Goodman, J. 2013, PASP, 125, 306

Fouqué, P., Moutou, C., Malo, L., Martioli, E., Lim, O., Rajpurohit, A., Artigau, E., Delfosse, X., Donati, J.-F., Forveille, T., Morin, J., Allard, F., Delage, R., Doyon, R., Hébrard, E., & Neves, V. 2018, MNRAS, 475, 1960

Fukugita, M., Ichikawa, T., Gunn, J. E., Doi, M., Shimasaku, K., & Schneider, D. P. 1996, AJ, 111, 1748

Gaia Collaboration, Brown, A. G. A., Vallenari, A., Prusti, T., de Bruijne, J. H. J., Babusiaux, C., Bailer-Jones, C. A. L., Biermann, M., Evans, D. W., Eyer, L., & et al. 2018, A&A, 616, A1

Gaia Collaboration, Prusti, T., de Bruijne, J. H. J., Brown, A. G. A., Vallenari, A., Babusiaux, C., Bailer-Jones, C. A. L., Bastian, U., Biermann, M., Evans, D. W., & et al. 2016, A&A, 595, A1

Gaidos, E., Mann, A. W., Lépine, S., Buccino, A., James, D., Ansdell, M., Petrucci, R., Mauas, P., & Hilton, E. J. 2014, MNRAS, 443, 2561

Gaudi, B. S. 2012, ARA&A, 50, 411

Girardi, L., Grebel, E. K., Odenkirchen, M., & Chiosi, C. 2004, A&A, 422, 205

Gizis, J. E. 1997, AJ, 113, 806

Gould, A. 1994, ApJ, 421, L71

Granzer, T., Schüssler, M., Caligari, P., & Strassmeier, K. G. 2000, A&A, 355, 1087

Gregory, P. C. 2005, Bayesian Logical Data Analysis for the Physical Sciences: A Comparative Approach with 'Mathematica' Support (Cambridge University Press)

Gully-Santiago, M. A., Herczeg, G. J., Czekala, I., Somers, G., Grankin, K., Covey, K. R., Donati, J. F., Alencar, S. H. P., Hussain, G. A. J., Shappee, B. J., Mace, G. N., Lee, J.-J., Holoien, T. W.-S., Jose, J., & Liu, C.-F. 2017, ApJ, 836, 200

Hall, D. S. 1991, in Lecture Notes in Physics, Berlin Springer Verlag, Vol. 380, IAU Colloq. 130: The Sun and Cool Stars. Activity, Magnetism, Dynamos, ed. I. Tuominen, D. Moss, & G. Rüdiger, 353

Han, E., Muirhead, P. S., Swift, J. J., Baranec, C., Law, N. M., Riddle, R., Atkinson, D., Mace, G. N., & DeFelippis, D. 2017, AJ, 154, 100

Hawley, S. L., Covey, K. R., Knapp, G. R., Golimowski, D. A., Fan, X., Anderson, S. F., Gunn, J. E., Harris, H. C., Ivezić, Ž., Long, G. M., Lupton, R. H., McGehee, P. M., Narayanan, V., Peng, E., Schlegel, D., Schneider, D. P., Spahn, E. Y., Strauss, M. A., Szkody, P., Tsvetanov, Z., Walkowicz, L. M., Brinkmann, J., Harvanek, M., Hennessy, G. S., Kleinman, S. J., Krzesinski, J., Long, D., Neilsen, E. H., Newman, P. R., Nitta, A., Snedden, S. A., & York, D. G. 2002, AJ, 123, 3409

Hayes, C. R., Majewski, S. R., Shetrone, M., Fernández-Alvar, E., Allende Prieto, C., Schuster, W. J., Carigi, L., Cunha, K., Smith, V. V., Sobeck, J., Almeida, A., Beers, T. C., Carrera, R., Fernández-Trincado, J. G., García-Hernández, D. A., Geisler, D., Lane, R. R., Lucatello, S., Matthews, A. M., Minniti, D., Nitschelm, C., Tang, B., Tissera, P. B., & Zamora, O. 2018, ApJ, 852, 49

Helmi, A., Ivezić, Ž., Prada, F., Pentericci, L., Rockosi, C. M., Schneider, D. P., Grebel, E. K., Harbeck, D., Lupton, R. H., Gunn, J. E., Knapp, G. R., Strauss, M. A., & Brinkmann, J. 2003, ApJ, 586, 195

Hilton, E. J., West, A. A., Hawley, S. L., & Kowalski, A. F. 2010, AJ, 140, 1402

Holberg, J. B. & Bergeron, P. 2006, AJ, 132, 1221

Husser, T.-O., Wende-von Berg, S., Dreizler, S., Homeier, D., Reiners, A., Barman, T., & Hauschildt, P. H. 2013, A&A, 553, A6

Iglesias, C. A. & Rogers, F. J. 1996, ApJ, 464, 943

Irwin, J., Berta, Z. K., Burke, C. J., Charbonneau, D., Nutzman, P., West, A. A., & Falco, E. E. 2011, ApJ, 727, 56

Ivezić, Ž., Sesar, B., Jurić, M., Bond, N., Dalcanton, J., Rockosi, C. M., Yanny, B., Newberg, H. J., Beers, T. C., Allende Prieto, C., Wilhelm, R., Lee, Y. S., Sivarani, T., Norris, J. E., Bailer-Jones, C. A. L., Re Fiorentin, P., Schlegel, D., Uomoto, A., Lupton, R. H., Knapp, G. R., Gunn, J. E., Covey, K. R., Allyn Smith, J., Miknaitis, G., Doi, M., Tanaka, M., Fukugita, M., Kent, S., Finkbeiner, D., Munn, J. A., Pier, J. R., Quinn, T., Hawley, S., Anderson, S., Kiuchi, F., Chen, A., Bushong, J., Sohi, H., Haggard, D., Kimball, A., Barentine, J., Brewington, H., Harvanek, M., Kleinman, S., Krzesinski, J., Long, D., Nitta, A., Snedden, S., Lee, B., Harris, H., Brinkmann, J., Schneider, D. P., & York, D. G. 2008, ApJ, 684, 287

Jackson, R. J., Deliyannis, C. P., & Jeffries, R. D. 2018, MNRAS, 476, 3245

Jackson, R. J. & Jeffries, R. D. 2013, MNRAS, 431, 1883

Jackson, R. J., Jeffries, R. D., & Maxted, P. F. L. 2009, MNRAS, 399, L89

Jackson, R. J., Jeffries, R. D., Randich, S., Bragaglia, A., Carraro, G., Costado, M. T., Flaccomio, E., Lanzafame, A. C., Lardo, C., Monaco, L., Morbidelli, L., Smiljanic, R., & Zaggia, S. 2016, A&A, 586, A52

Jao, W.-C., Henry, T. J., Beaulieu, T. D., & Subasavage, J. P. 2008, AJ, 136, 840

Jeffers, S. V., Donati, J.-F., & Collier Cameron, A. 2007, MNRAS, 375, 567

Jenkins, J. S., Ramsey, L. W., Jones, H. R. A., Pavlenko, Y., Gallardo, J., Barnes, J. R., & Pinfield, D. J. 2009, ApJ, 704, 975

Johnson, J. A. 2019, Science, 363, 474

Jones, J. E., Alloin, D. M., & Jones, B. J. T. 1984, ApJ, 283, 457

Kass, R. E. & Raftery, A. E. 1995, J. Am. Stat. Assoc., 90, 773

Kervella, P. & Fouqué, P. 2008, A&A, 491, 855

Kesseli, A. Y., Kirkpatrick, J. D., Fajardo-Acosta, S. B., Penny, M. T., Gaudi, B. S., Veyette, M., Boeshaar, P. C., Henderson, C. B., Cushing, M. C., Calchi-Novati, S., Shvartzvald, Y., & Muirhead, P. S. 2019, AJ, 157, 63

Kesseli, A. Y., Muirhead, P. S., Mann, A. W., & Mace, G. 2018, AJ, 155, 225

Kesseli, A. Y., West, A. A., Veyette, M., Harrison, B., Feldman, D., & Bochanski, J. J. 2017, ApJS, 230, 16

Kirkpatrick, J. D., Henry, T. J., & McCarthy, Jr., D. W. 1991, ApJS, 77, 417

Kirkpatrick, J. D., Kellogg, K., Schneider, A. C., Fajardo-Acosta, S., Cushing, M. C., Greco, J., Mace, G. N., Gelino, C. R., Wright, E. L., Eisenhardt, P. R. M., Stern, D., Faherty, J. K., Sheppard, S. S., Lansbury, G. B., Logsdon, S. E., Martin, E. C., McLean, I. S., Schurr, S. D., Cutri, R. M., & Conrow, T. 2016, ApJS, 224, 36

Kleinman, S. J., Kepler, S. O., Koester, D., Pelisoli, I., Peçanha, V., Nitta, A., Costa, J. E. S., Krzesinski, J., Dufour, P., Lachapelle, F.-R., Bergeron, P., Yip, C.-W., Harris, H. C., Eisenstein, D. J., Althaus, L., & Córsico, A. 2013, ApJS, 204, 5

Kraus, A. L., Tucker, R. A., Thompson, M. I., Craine, E. R., & Hillenbrand, L. A. 2011, ApJ, 728, 48

Küker, M. & Rüdiger, G. 2011, Astronomische Nachrichten, 332, 933

Kurucz, R. L. 1979, ApJS, 40, 1

Lee, J.-J., Gullikson, K., & Kaplan, K. 2017, igrins/plp 2.2.0

Lee, Y. S., Beers, T. C., Sivarani, T., Allende Prieto, C., Koesterke, L., Wilhelm, R., Re Fiorentin, P., Bailer-Jones, C. A. L., Norris, J. E., Rockosi, C. M., Yanny, B., Newberg, H. J., Covey, K. R., Zhang, H.-T., & Luo, A.-L. 2008, AJ, 136, 2022

Leighton, R. B. 1959, ApJ, 130, 366

Lépine, S., Rich, R. M., & Shara, M. M. 2003, AJ, 125, 1598

—. 2007, ApJ, 669, 1235

Lépine, S., Shara, M. M., & Rich, R. M. 2004, ApJ, 602, L125

Lockwood, G. W., Skiff, B. A., Henry, G. W., Henry, S., Radick, R. R., Baliunas, S. L., Donahue, R. A., & Soon, W. 2007, ApJS, 171, 260

López-Morales, M. 2007, ApJ, 660, 732

MacDonald, J. & Gizis, J. 2018, MNRAS, 480, 1711

MacDonald, J. & Mullan, D. J. 2017, ApJ, 850, 58

Mace, G., Kim, H., Jaffe, D. T., Park, C., Lee, J.-J., Kaplan, K., Yu, Y. S., Yuk, I.-S., Chun, M.-Y., Pak, S., Kim, K.-M., Lee, J.-E., Sneden, C. A., Afsar, M., Pavel, M. D., Lee, H., Oh, H., Jeong, U., Park, S., Kidder, B., Lee, H.-I., Nguyen Le, H. A., McLane, J., Gully-Santiago, M., Oh, J. S., Lee, S., Hwang, N., & Park, B.-G. 2016, in Proc. SPIE, Vol. 9908, Ground-based and Airborne Instrumentation for Astronomy VI, 99080C

Mann, A. W., Brewer, J. M., Gaidos, E., Lépine, S., & Hilton, E. J. 2013a, AJ, 145, 52

Mann, A. W., Deacon, N. R., Gaidos, E., Ansdell, M., Brewer, J. M., Liu, M. C., Magnier, E. A., & Aller, K. M. 2014, AJ, 147, 160

Mann, A. W., Dupuy, T., Kraus, A. L., Gaidos, E., Ansdell, M., Ireland, M., Rizzuto, A. C., Hung, C.-L., Dittmann, J., Factor, S., Feiden, G., Martinez, R. A., Ruíz-Rodríguez, D., & Thao, P. C. 2019, ApJ, 871, 63

Mann, A. W., Feiden, G. A., Gaidos, E., & Boyajian, T. 2015, ArXiv e-prints

Mann, A. W., Gaidos, E., & Ansdell, M. 2013b, ApJ, 779, 188

Mann, A. W., Gaidos, E., Kraus, A., & Hilton, E. J. 2013c, ApJ, 770, 43

McQuillan, A., Aigrain, S., & Mazeh, T. 2013, MNRAS, 432, 1203

Meibom, S., Mathieu, R. D., & Stassun, K. G. 2006, ApJ, 653, 621

Miller, A. A. 2015, ApJ, 811, 30

Mohanty, S. & Basri, G. 2003, ApJ, 583, 451

Monnier, J. D. 2003, Reports on Progress in Physics, 66, 789

Monnier, J. D., Zhao, M., Pedretti, E., Thureau, N., Ireland, M., Muirhead, P., Berger, J. P., Millan-Gabet, R., Van Belle, G., & ten Brummelaar, T. 2007, Science, 317, 342

Morales, J. C., Gallardo, J., Ribas, I., Jordi, C., Baraffe, I., & Chabrier, G. 2010, ApJ, 718, 502

Morales, J. C., Ribas, I., & Jordi, C. 2008, A&A, 478, 507

Morgan, D. P., West, A. A., Garcés, A., Catalán, S., Dhital, S., Fuchs, M., & Silvestri, N. M. 2012, AJ, 144, 93

Morin, J., Donati, J.-F., Petit, P., Delfosse, X., Forveille, T., & Jardine, M. M. 2010, MNRAS, 407, 2269

Morris, B. M., Agol, E., Davenport, J. R. A., & Hawley, S. L. 2018, ApJ, 857, 39

Muirhead, P. S., Dressing, C. D., Mann, A. W., Rojas-Ayala, B., Lépine, S., Paegert, M., De Lee, N., & Oelkers, R. 2018, AJ, 155, 180

Muirhead, P. S., Vanderburg, A., Shporer, A., Becker, J., Swift, J. J., Lloyd, J. P., Fuller, J., Zhao, M., Hinkley, S., Pineda, J. S., Bottom, M., Howard, A. W., von Braun, K., Boyajian, T. S., Law, N., Baranec, C., Riddle, R., Ramaprakash, A. N., Tendulkar, S. P., Bui, K., Burse, M., Chordia, P., Das, H., Dekany, R., Punnadi, S., & Johnson, J. A. 2013, ApJ, 767, 111

Nemiroff, R. J. & Wickramasinghe, W. A. D. T. 1994, ApJ, 424, L21

Newton, E. R., Charbonneau, D., Irwin, J., Berta-Thompson, Z. K., Rojas-Ayala, B., Covey, K., & Lloyd, J. P. 2014, AJ, 147, 20

Newton, E. R., Charbonneau, D., Irwin, J., & Mann, A. W. 2015, ApJ, 800, 85

Newton, E. R., Irwin, J., Charbonneau, D., Berlind, P., Calkins, M. L., & Mink, J. 2017, ApJ, 834, 85

Newton, E. R., Irwin, J., Charbonneau, D., Berta-Thompson, Z. K., Dittmann, J. A., & West, A. A. 2016, ApJ, 821, 93

Oke, J. B. & Gunn, J. E. 1982, PASP, 94, 586

—. 1983, ApJ, 266, 713

Ossendrijver, M. 2003, A&A Rev., 11, 287

Park, C., Jaffe, D. T., Yuk, I.-S., Chun, M.-Y., Pak, S., Kim, K.-M., Pavel, M., Lee, H., Oh, H., Jeong, U., Sim, C. K., Lee, H.-I., Nguyen Le, H. A., Strubhar, J., Gully-Santiago, M., Oh, J. S., Cha, S.-M., Moon, B., Park, K., Brooks, C., Ko, K., Han, J.-Y., Nah, J., Hill, P. C., Lee, S., Barnes, S., Yu, Y. S., Kaplan, K., Mace, G., Kim, H., Lee, J.-J., Hwang, N., & Park, B.-G. 2014, in Proc. SPIE, Vol. 9147, Ground-based and Airborne Instrumentation for Astronomy V, 91471D

Parker, E. N. 1955, ApJ, 122, 293

—. 1975, ApJ, 198, 205

Parsons, S. G., Gänsicke, B. T., Marsh, T. R., Ashley, R. P., Breedt, E., Burleigh, M. R., Copperwheat, C. M., Dhillon, V. S., Green, M. J., Hermes, J. J., Irawati, P., Kerry, P., Littlefair, S. P., Rebassa-Mansergas, A., Sahman, D. I., Schreiber, M. R., & Zorotovic, M. 2018, MNRAS, 481, 1083

Peth, M. A., Ross, N. P., & Schneider, D. P. 2011, AJ, 141, 105

Pickles, A. J. 1998, PASP, 110, 863

Prugniel, P. & Soubiran, C. 2001, A&A, 369, 1048

Rabus, M., Lachaume, R., Jordán, A., Brahm, R., Boyajian, T., von Braun, K., Espinoza, N., Berger, J.-P., Le Bouquin, J.-B., & Absil, O. 2019, MNRAS, 484, 2674

Rajpurohit, A. S., Reylé, C., Allard, F., Homeier, D., Bayo, A., Mousis, O., Rajpurohit, S., & Fernández-Trincado, J. G. 2016, A&A, 596, A33

Rajpurohit, A. S., Reylé, C., Allard, F., Scholz, R.-D., Homeier, D., Schultheis, M., & Bayo, A. 2014, A&A, 564, A90

Ramsey, L. W. & Nations, H. L. 1980, ApJ, 239, L121

Rayner, J., Bond, T., Bonnet, M., Jaffe, D., Muller, G., & Tokunaga, A. 2012, in SPIE Proc, Vol. 8446

Rayner, J., Tokunaga, A., Jaffe, D., Bonnet, M., Ching, G., Connelley, M., Kokubun, D., Lockhart, C., & Warmbier, E. 2016, in Proc. SPIE, Vol. 9908, Ground-based and Airborne Instrumentation for Astronomy VI, 990884

Rebull, L. M., Stauffer, J. R., Bouvier, J., Cody, A. M., Hillenbrand, L. A., Soderblom, D. R., Valenti, J., Barrado, D., Bouy, H., Ciardi, D., Pinsonneault, M., Stassun, K., Micela, G., Aigrain, S., Vrba, F., Somers, G., Christiansen, J., Gillen, E., & Collier Cameron, A. 2016a, AJ, 152, 113

Rebull, L. M., Stauffer, J. R., Bouvier, J., Cody, A. M., Hillenbrand, L. A., Soderblom, D. R., Valenti, J., Barrado, D., Bouy, H., Ciardi, D., Pinsonneault, M., Stassun, K., Micela, G., Aigrain, S., Vrba, F., Somers, G., Gillen, E., & Collier Cameron, A. 2016b, AJ, 152, 114

Reid, I. N. & Hawley, S. L. 2005, New light on dark stars : red dwarfs, low-mass stars, brown dwarfs, ed. Reid, I. N. & Hawley, S. L.

Reid, I. N., Hawley, S. L., & Gizis, J. E. 1995, AJ, 110, 1838

Reid, I. N., Kirkpatrick, J. D., Liebert, J., Gizis, J. E., Dahn, C. C., & Monet, D. G. 2002, AJ, 124, 519

Reiners, A., Zechmeister, M., Caballero, J. A., Ribas, I., Morales, J. C., Jeffers, S. V., Schöfer, P., Tal-Or, L., Quirrenbach, A., Amado, P. J., Kaminski, A., Seifert, W., Abril, M., Aceituno, J., Alonso-Floriano, F. J., Ammler-von Eiff, M., Antona, R., Anglada-Escudé, G., Anwand-Heerwart, H., Arroyo-Torres, B., Azzaro, M., Baroch, D., Barrado, D., Bauer, F. F., Becerril, S., Béjar, V. J. S., Benítez, D., Berdiñas, Z. M., Bergond, G., Blümcke, M., Brinkmöller, M., del Burgo, C., Cano, J., Cárdenas Vázquez, M. C., Casal, E., Cifuentes, C., Claret, A., Colomé, J., Cortés-Contreras, M., Czesla, S., Díez-Alonso, E., Dreizler, S., Feiz, C., Fernández, M., Ferro, I. M., Fuhrmeister, B., Galadí-Enríquez, D., Garcia-Piquer, A., García Vargas, M. L., Gesa, L., Gómez, V., Galera, González Hernández, J. I., González-Peinado, R., Grözinger, U., Grohnert, S., Guàrdia, J., Guenther, E. W., Guijarro, A., de Guindos, E., Gutiérrez-Soto, J., Hagen, H.-J., Hatzes, A. P., Hauschildt, P. H., Hedrosa, R. P., Helmling, J., Henning, T., Hermelo, I., Hernández Arabí, R., Hernández Castaño, L., Hernández Hernando, F., Herrero, E., Huber, A., Huke, P., Johnson, E., de Juan, E., Kim, M., Klein, R., Klüter, J., Klutsch, A., Kürster, M., Lafarga, M., Lamert, A., Lampón, M., Lara, L. M., Laun, W., Lemke, U., Lenzen, R., Launhardt, R., López del Fresno, M., López-González, J., López-Puertas, M., López Salas, J. F., López-Santiago, J., Luque, R., Magán Madinabeitia, H., Mall, U., Mancini, L., Mandel, H., Marfil, E., Marín Molina, J. A., Maroto, D., Fernández, Martín, E. L., Martín-Ruiz, S., Marvin, C. J., Mathar, R. J., Mirabet, E., Montes, D., Moreno-Raya, M. E., Moya, A., Mundt, R., Nagel, E., Naranjo, V., Nortmann, L., Nowak, G., Ofir, A., Oreiro, R., Pallé, E., Panduro, J., Pascual, J., Passegger, V. M., Pavlov, A., Pedraz, S., Pérez-Calpena, A., Pérez Medialdea, D., Perger, M., Perryman, M. A. C., Pluto, M., Rabaza, O., Ramón, A., Rebolo, R., Redondo, P., Reffert, S., Reinhart, S., Rhode, P., Rix, H.-W., Rodler, F., Rodríguez, E., Rodríguez-López, C., Rodríguez Trinidad, A., Rohloff, R.-R., Rosich, A., Sadegi, S., Sánchez-Blanco, E., Sánchez Carrasco, M. A., Sánchez-López, A., Sanz-Forcada, J., Sarkis, P., Sarmiento, L. F., Schäfer, S., Schmitt, J. H. M. M., Schiller, J., Schweitzer, A., Solano, E., Stahl, O., Strachan, J. B. P., Stürmer, J., Suárez, J. C., Tabernero, H. M., Tala, M., Trifonov, T., Tulloch, S. M., Ulbrich, R. G., Veredas, G., Vico Linares, J. I., Vilardell, F., Wagner, K., Winkler, J., Wolthoff, V., Xu, W., Yan, F., & Zapatero Osorio, M. R. 2017, ArXiv e-prints

Reinhold, T. & Gizon, L. 2015, A&A, 583, A65

Reylé, C., Rajpurohit, A. S., Schultheis, M., & Allard, F. 2011, in Astronomical Society of the Pacific Conference Series, Vol. 448, 16th Cambridge Workshop on Cool Stars, Stellar Systems, and the Sun, ed. C. Johns-Krull, M. K. Browning, & A. A. West, 929

Rojas-Ayala, B., Covey, K. R., Muirhead, P. S., & Lloyd, J. P. 2010, ApJ, 720, L113

—. 2012, ApJ, 748, 93

Saar, S. H. & Linsky, J. L. 1985, ApJ, 299, L47

Sandage, A. R. & Eggen, O. J. 1959, MNRAS, 119, 278

Savcheva, A. S., West, A. A., & Bochanski, J. J. 2014, ApJ, 794, 145

Schlieder, J. E., Lépine, S., Rice, E., Simon, M., Fielding, D., & Tomasino, R. 2012, AJ, 143, 114

Schmidt, S. J., Wagoner, E. L., Johnson, J. A., Davenport, J. R. A., Stassun, K. G., Souto, D., & Ge, J. 2016, MNRAS, 460, 2611

Schmidt, S. J., West, A. A., Bochanski, J. J., Hawley, S. L., & Kielty, C. 2014, PASP, 126, 642

Scholz, A., Irwin, J., Bouvier, J., Sipőcz, B. M., Hodgkin, S., & Eislöffel, J. 2011, MNRAS, 413, 2595

Ségransan, D., Kervella, P., Forveille, T., & Queloz, D. 2003, A&A, 397, L5

Sellke, T., Bayarri, M. J., & J., B. 2001, Am. Stat., 55, 62

Shkolnik, E., Liu, M. C., & Reid, I. N. 2009, ApJ, 699, 649

Skrutskie, M. F., Cutri, R. M., Stiening, R., Weinberg, M. D., Schneider, S., Carpenter, J. M., Beichman, C., Capps, R., Chester, T., Elias, J., Huchra, J., Liebert, J., Lonsdale, C., Monet, D. G., Price, S., Seitzer, P., Jarrett, T., Kirkpatrick, J. D., Gizis, J. E., Howard, E., Evans, T., Fowler, J., Fullmer, L., Hurt, R., Light, R., Kopan, E. L., Marsh, K. A., McCallon, H. L., Tam, R., Van Dyk, S., & Wheelock, S. 2006, AJ, 131, 1163

Skumanich, A. 1972, ApJ, 171, 565

Skumanich, A., Smythe, C., & Frazier, E. N. 1975, ApJ, 200, 747

Spite, M., Cayrel, R., Plez, B., Hill, V., Spite, F., Depagne, E., François, P., Bonifacio, P., Barbuy, B., Beers, T., Andersen, J., Molaro, P., Nordström, B., & Primas, F. 2005, A&A, 430, 655

Strassmeier, K. G. 2009, A&A Rev., 17, 251

ten Brummelaar, T. A., McAlister, H. A., Ridgway, S. T., W. G. Bagnuolo, J., Turner, N. H., Sturmann, L., Sturmann, J., Berger, D. H., Ogden, C. E., Cadman, R., Hartkopf, W. I., Hopper, C. H., & Shure, M. A. 2005, The Astrophysical Journal, 628, 453

Terrien, R. C., Mahadevan, S., Bender, C. F., Deshpande, R., Ramsey, L. W., & Bochanski, J. J. 2012, ApJ, 747, L38

Theissen, C. A. & West, A. A. 2014, ApJ, 794, 146

Torres, G., Andersen, J., & Giménez, A. 2010, A&A Rev., 18, 67

Torres, G. & Ribas, I. 2002, ApJ, 567, 1140

Turnshek, D. E., Turnshek, D. A., & Craine, E. R. 1985, An atlas of digital spectra of cool stars

Vacca, W. D., Cushing, M. C., & Rayner, J. T. 2003, PASP, 115, 389

VandenBerg, D. A., Bergbusch, P. A., & Dowler, P. D. 2006, ApJS, 162, 375

Veyette, M. J. & Muirhead, P. S. 2018, ApJ, 863, 166

Veyette, M. J., Muirhead, P. S., Mann, A. W., Brewer, J. M., Allard, F., & Homeier, D. 2017, ApJ, 851, 26

Vogt, S. S. 1979, PASP, 91, 616

—. 1980, ApJ, 240, 567

von Braun, K., Boyajian, T. S., van Belle, G. T., Kane, S. R., Jones, J., Farrington, C., Schaefer, G., Vargas, N., Scott, N., ten Brummelaar, T. A., Kephart, M., Gies, D. R., Ciardi, D. R., López-Morales, M., Mazingue, C., McAlister, H. A., Ridgway, S., Goldfinger, P. J., Turner, N. H., & Sturmann, L. 2014, MNRAS, 438, 2413

West, A. A. & Basri, G. 2009, ApJ, 693, 1283

West, A. A., Hawley, S. L., Bochanski, J. J., Covey, K. R., Reid, I. N., Dhital, S., Hilton, E. J., & Masuda, M. 2008, AJ, 135, 785

West, A. A., Morgan, D. P., Bochanski, J. J., Andersen, J. M., Bell, K. J., Kowalski, A. F., Davenport, J. R. A., Hawley, S. L., Schmidt, S. J., Bernat, D., Hilton, E. J., Muirhead, P., Covey, K. R., Rojas-Ayala, B., Schlawin, E., Gooding, M., Schluns, K., Dhital, S., Pineda, J. S., & Jones, D. O. 2011, AJ, 141, 97

West, A. A., Weisenburger, K. L., Irwin, J., Berta-Thompson, Z. K., Charbonneau, D., Dittmann, J., & Pineda, J. S. 2015, ApJ, 812, 3

Wilson, O. C. 1968, ApJ, 153, 221

Witt, H. J. & Mao, S. 1994, ApJ, 430, 505

Woolf, V. M., Lépine, S., & Wallerstein, G. 2009, PASP, 121, 117

Woosley, S. E. & Weaver, T. A. 1995, ApJS, 101, 181

Wright, E. L., Eisenhardt, P. R. M., Mainzer, A. K., Ressler, M. E., Cutri, R. M., Jarrett, T., Kirkpatrick, J. D., Padgett, D., McMillan, R. S., Skrutskie, M., Stanford, S. A., Cohen, M., Walker, R. G., Mather, J. C., Leisawitz, D., Gautier, III, T. N., McLean, I., Benford, D., Lonsdale, C. J., Blain, A., Mendez, B., Irace, W. R., Duval, V., Liu, F., Royer, D., Heinrichsen, I., Howard, J., Shannon, M., Kendall, M., Walsh, A. L., Larsen, M., Cardon, J. G., Schick, S., Schwalm, M., Abid, M., Fabinsky, B., Naes, L., & Tsai, C.-W. 2010, AJ, 140, 1868

Yoo, J., DePoy, D. L., Gal-Yam, A., Gaudi, B. S., Gould, A., Han, C., Lipkin, Y., Maoz, D., Ofek, E. O., Park, B.-G., Pogge, R. W., Mu-Fun Collaboration, Udalski, A., Soszyński, I., Wyrzykowski, Ł., Kubiak, M., Szymański, M., Pietrzyński, G., Szewczyk, O., Żebruń, K., & OGLE Collaboration. 2004, ApJ, 603, 139

Youngblood, A., France, K., Loyd, R. O. P., Brown, A., Mason, J. P., Schneider, P. C., Tilley, M. A., Berta-Thompson, Z. K., Buccino, A., Froning, C. S., Hawley, S. L., Linsky, J., Mauas, P. J. D., Redfield, S., Kowalski, A., Miguel, Y., Newton, E. R., Rugheimer, S., Segura, A., Roberge, A., & Vieytes, M. 2017, ApJ, 843, 31

Zhang, Z. H., Pinfield, D. J., Gálvez-Ortiz, M. C., Burningham, B., Lodieu, N., Marocco, F., Burgasser, A. J., Day-Jones, A. C., Allard, F., Jones, H. R. A., Homeier, D., Gomes, J., & Smart, R. L. 2017, MNRAS, 464, 3040

Zhu, W., Penny, M., Mao, S., Gould, A., & Gendron, R. 2014, ApJ, 788, 73

Curriculum Vitae